ABSTRACT

EXPERIMENTAL STUDIES AND MODELING OF MECHANICAL PROPERTIES AND MORPHOLOGIES OF *IN SITU* POLYMER COMPOSITES

by

Zhigang Li

In this study, a series of experiments was set up in order to analyze the morphology development and mechanical properties of poly(ethylene terephthalate) (PET)/ liquid crystalline polymer (LCP) blends. Simulations of the injection molded blends at various process conditions were performed using CMOLD. In order to determine the effect of the processing parameters on the deformation of the LCP domains during the injection molding, a new analytical method to analyze the melt flow in the advancing melt front (AMF) region was developed. By combining the simulations of the injection molding and analysis of the melt flow in the AMF region, velocity and deformation in the AMF region at various injection molding conditions were determined. A relationship between the aspect ratio of the LCP fibers and elongational strain was developed by assuming an affine deformation of the LCP domains. A new method was also developed to predict the tensile modulus of the injection molded blends by introducing the effects of injection molding parameters, based on the Halpin-Tsai composite model. The relationships between the structure and mechanical properties of the blends, between processing parameters, the properties and the structure, have been investigated.

Our studies show that injection speed and mold temperature have significant effects on the morphological development and mechanical properties of the PET/LCP

blends. A 10 % increase in the tensile modulus could be obtained when the two parameters are changed at the same time. It was also found that melt temperature has a distinct effect on the strength of the blends. An effective way to enhance the modulus and strength of the blends is to increase LCP content but high LCP content results in an increase in the cost of the materials and a decrease in the elongation of LCP blends.

The efficacy of the new method to calculate the tensile modulus of the injection molded PET/LCP blends is demonstrated by comparing the theoretical predictions and experimental results. An agreement between the predictions and experimental data was obtained.

EXPERIMENTAL STUDIES AND MODELING OF MECHANICAL PROPERTIES AND MORPHOLOGIES OF *IN SITU* POLYMER COMPOSITES

by
Zhigang Li

A Dissertation
Submitted to the Faculty of
New Jersey Institute of Technology
in Partial Fulfillment of the Requirement for the Degree of
Doctor of Philosophy

Department of Mechanical Engineering

January 2000

APPROVAL PAGE

EXPERIMENTAL STUDIES AND MODELING OF MECHANICAL PROPERTIES AND MORPHOLOGIES OF *IN SITU* POLYMER COMPOSITES

Zhigang Li

Dr. Kwabena A. Narh, Dissertation Advisor — Date
Assistant Professor of Mechanical Engineering, NJIT

Dr. Rong Y. Chen, Committee Member — Date
Professor and Graduate Advisor of Mechanical Engineering, NJIT

Dr. Marino Xanthos, Committee Member — Date
Professor of Chem. Engineering, Chemistry, and Environmental Sci., NJIT and
Director of Research, Polymer Processing Institute, at NJIT

Dr. Zhiming Ji, Committee Member — Date
Associate Professor of Mechanical Engineering, NJIT

Dr. Ernest S. Geskin, Committee Member — Date
Professor of Mechanical Engineering, NJIT

BIOGRAPHICAL SKETCH

Author: Zhigang Li

Degree: Doctor of Philosophy

Date: January 2000

Undergraduate and Graduate Education:

- Doctor of Philosophy in Mechanical Engineering,
  New Jersey Institute of Technology, Newark, NJ, 2000

- Master of Science in Mechanical Engineering,
  Beijing University of Chemical Technology, Beijing, P. R. China, 1986

- Bachelor of Science in Mechanical Engineering,
  Beijing University of Chemical Technology, Beijing, P. R. China, 1982

Major: Mechanical Engineering

Presentations and Publications:

Li, Z. and K. A. Narh. 1999. "Morphological Development during Injection Molding of Self-Reinforcing Composites: II. Numerical Simulations and Analytical Predictions." *Polymer Composites,* Submitted.

Narh, K. A. and Z. Li. 1999. "Morphological Development during Injection Molding of Self-Reinforcing Composites: I. Experimental Results." *Polymer Composites,* Submitted.

Narh, K. A., Q. Zhang, and Z. Li. 1999. "The Effect of Mixing Shear Rate on the Properties of Liquid Crystalline Polymer/Polyethylene (terephthalate) Blends." *J. of Appl. Polym. Sci.*, Accepted.

Li, Z. and K. A. Narh. 1999. "Effect of Processing Conditions on the Morphological Development of Injection Molded In-Situ Polymer Composites." Sixth Annual International Conference on Composite Engineering, June, Orlando, Florida, p.613.

Li, Z. and K. A. Narh. 1999. "Effect of Processing Parameters on the Modulus and Structure of PET/LCP Blends." 1999 Proceedings of the SPE ANTEC Conference, May, New York, p.2835 - 2839.

Narh, K. A., J. Guo, and Z. Li. 1998. "Measurement and Molding of Flow and Mechanical Properties of ASR-Filled Polymer Composites." *Polymer Composites* 19 (6):787 -792.

Narh, K. A., M. Xanthos, Z. Li, S. K. Dey, U. Yilmazer and Y. Li, 1998. "Simulation of the Intrusion Process for Thick-walled thermoplastics Product and Process Characteristics." 1998 Proceedings of the SPE ANTEC Conference, April, Atlanta, Georgia, p.1767 - 1771.

Narh, K. A., Z. Li , and M. Xanthos. 1997. "Prototype Design and Moldability Analysis with Glass-fiber Reinforced Polymer Blends." 1997 Proceedings of SPE ANTEC Conference, April, Toronto, Canada, p.678 - 681.

Narh, K. A., M. Xanthos, Z. Li, and D. H. Sebastian, 1996. "Composites From Commingled Waste Plastics: Prototype Design and Moldability Analysis." 1996 Proceedings of AICHE Annual Conference, November, Chicago, ILL.

Li, Z. and K. A. Narh, 1996. "Design and Moldability Analysis of an Adjustable Automobile Armrest." 1996 Sixth Annual Mini-tech Conference, April, Hoboken, New Jersey.

This thesis is dedicated to my family,
for all their love and support

ACKNOWLEDGMENT

The author wishes to express his sincere gratitude to his advisor, Dr. K. A. Narh, for his remarkable guidance, constant supervision, and friendship throughout this research. A special appreciation is extended to Dr. M. Xanthos for his remarkable help and advice and for serving on the dissertation committee .

Special thanks to Dr. Z. Ji, Dr. R. Y. Chen, and Dr. E. S. Geskin for serving as members of the committee, having kindly read through the original manuscript, and providing many valuable suggestions. Additionally, sincere thanks to Dr. Dey (PPI), Mr. Y. Li, Mr. Zhang, Mr. Guo, and Dr. Sridhar for their timely help and suggestions in this study.

The author wishes to thank the Department of Mechanical Engineering, NJIT for funding assistantship from Jan., 1995 to July, 1999 during the Ph. D. program.

And finally, grateful thanks to the author's parents, brother, sister, especially, his wife and son, for the firm support and encouragement.

TABLE OF CONTENTS

TABLE OF CONTENTS
(Continued)

Chapter **Page**

TABLE OF CONTENTS
(Continued)

Chapter **Page**

TABLE OF CONTENTS
(Continued)

LIST OF TABLES

LIST OF FIGURES

LIST OF FIGURES
(Continued)

Figure **Page**

LIST OF FIGURES
(Continued)

Figure **Page**

LIST OF FIGURES
(Continued)

Figure **Page**

LIST OF FIGURES
(Continued)

Figure **Page**

LIST OF FIGURES
(Continued)

Figure **Page**

LIST OF FIGURES
(Continued)

Figure **Page**

LIST OF FIGURES
(Continued)

Figure **Page**

LIST OF SYMBOLS

C_p	Specific heat (J/Kg-K)
E	Modulus (Pa)
E_f	Filler modulus (Pa)
E_m	Matrix modulus (Pa)
H	Thickness of mold cavity (m)
K	Thermal conductivity (W/m-K)
M	Magnification ratio
V	Velocity (m/s)
V_f	Filler volume fraction
VI	Velocity at the entrance of the advancing melt front (m/s)
VO	Velocity on the free surface (m/s)
L/D	Aspect ratio: length to diameter of a fiber
ε	Elongational strain
ρ	Density (Kg/m^3)
y, z	Denote the two directions

Subscript

f	Filler
m	Matrix
p	Pressure
w	Weight

LIST OF ABBREVIATIONS

AMF	Advancing melt front
AN	Amorphous nylon
DR	Draw ratio
EPDM	Ethylene-propylene-diene terpolymer
HBA	Hydroxybenzoic acid
HNA	Hydroxy naphthoic acid
HQ	Hydroquinone
LCP	Liquid crystalline polymer
MVE	Matrix Videometrix Econoscope
OM	Optical microscopy
PA	Polyamide
PBT	Poly (butylene terephthalate)
PC	Polycarbonate
PET	Poly (ethylene terephthalate)
PHB	Poly-hydroxybenzoate
PP	Polypropylene
PPE	Polyphenylene ether
PS	Polystyrene
SEM	Scanning electron microscopy
TA	Terephthalic acid
TP	Thermoplastic

CHAPTER 1

INTRODUCTION

Polymers are relatively cheap, large volume structural materials comparable in importance to metals. Their widespread use and rapid growth result largely from their versatile mechanical and physical properties in flexibility, strength-to-weight ratio, abrasion resistance, energy absorption of foams, thermal and electrical insulation, variety in color and clarity, and resistance to inorganic and/or organic chemicals. Even though there is a broad spectrum of properties offered by the variety of polymers, their grades are still not sufficient to meet the demands of engineering and structural applications. For example, the mechanical properties, such as stiffness and strength, of non-reinforced polymers are very poor. When compared to those of metals, the moduli of these materials are ~100 times lower and strengths ~5 times lower (McCrum et al. 1992). Therefore, one wishes to develop materials with the combinations of the properties of polymers and to set up much wider applications in engineering or other fields for them. Polymer blends and composites have provided researchers and engineers effective approaches to tailor-make the materials for improving their mechanical properties, and for achieving the specific combinations of the physical properties, processing characteristics, and cost. Currently, more and more polymers are used in the form of blends and composites, and the use of unmodified neat resins has shrunk rapidly (Utracki 1990).

A polymer blend is a mixture of at least two polymers or copolymers. Use of polymer blends is for developing materials with a full set of desired properties at a low cost. The disadvantages of one polymer are often compensated by the advantages of other polymers. For example, the weaknesses of polyphenylene ether (PPE) are its poor processability and low impact strength; polyamide (PA) with good processability and

high impact strength can be used to blend with PPE to compensate for the disadvantages of PPE.

Most polymer materials are used because they have desirable mechanical properties at an economical cost. For this reason, the mechanical properties should be considered the most important of all the physical and chemical properties of polymers in applications of polymers. The usual and better method of improving the mechanical properties of polymers is to fill polymers with reinforcing materials, or to develop polymer composites.

A polymer composite is a mixture of at least one polymer and fillers (the aspect ratio of fillers is close to one), or is a material in which at least one polymer matrix is combined with reinforcing fibers, which are stronger and stiffer than the polymer matrix. Fillers are used to decrease the cost of materials; reinforcements are used to improve the mechanical properties of polymers. The fiber-reinforced polymer can be classified as long fiber-reinforced polymers and short fiber-reinforced polymers. Recent years have seen rapid growth in the use of short fiber-reinforced polymers. This is because rapid, economical process technology is probably the single most important factor in the growth of the composites, and a major advantage of short fiber-reinforced polymers is that forming of the polymers is possible by normal injection molding or extrusion techniques. These techniques are the most economical processes when cheap and precise manufacture of very large quantities of components is required. In our life, we can find many products, which are manufactured with these materials such as tennis racquet frames, storage tanks, pipes, seating for public places, plastic window frame, and components of boats and planes. But the presence of rigid fillers or reinforcing materials in a polymeric matrix entails many problems such as high processing temperature which can easily result in potential degradation of the polymer matrix, high energy required for processing, and the abrasion of processing equipment. From environmental considerations, it is not easy to re-engineer the reinforced materials, thereby possibly discarding them after using, and

resulting in environmental problems. The difficulty in re-engineering the materials originates from the significant decrease of mechanical properties after repeated recycling due to the reduction of aspect ratio of reinforcing fibers during reprocessing.

Is it possible to find a material that can be used to reinforce polymers as traditional fibers did and, at the same time, does not entail the problems, which occur at the processing of fiber-reinforced polymers? Liquid crystalline polymers (LCPs) provide a solution to the challenge. An important characteristic of many LCPs is that they have no pronounced structural periodicity along the backbone and, therefore, they give rise more easily to nematic structures, rather than to smectic ones. In recent years, LCPs have entered the polymer market (Naitive 1985, Wood 1985). Froix (1980) and Cogswell et al. (1983) used LCPs as processing aids and reinforcing agents. Cogswell et al. reported that the viscosity of thermoplastic (TP)/liquid crystalline polymer (LCP) blends was much lower than that of the thermoplastic polymers alone and the processing temperatures could be reduced. The mechanical properties of TP/LCP blends have also been reported (Siegmann et al. 1985; Chung 1987). It was found that higher mechanical properties from TP/LCP blends have been achieved. Although the mixtures of thermoplastics and liquid crystalline polymers are polymer blends, we can also call them composites. This is because suitable processing histories can yield a reinforcing, microfibrillar morphology of the dispersed LCP-phase. The final structures of TP/LCP blends assemble composites: they consist of a matrix (thermoplastic) and reinforcing fibers (LCP) which are stronger and stiffer than the thermoplastic matrix.

Studies have shown that blending flexible thermoplastic polymers with LCPs can give rise to two important results:

- Processability is improved as a result of the viscosity decrease. The decrease of viscosity can make processable blend matrices, which otherwise cannot be melt processed.

- A composite-like morphology is developed which can determine remarkable mechanical properties.

LCP composites have many advantages over conventional short fiber reinforced composites. The two most distinct advantages are: (1) The reinforcing fibrillar morphology is formed *in-situ*, i.e., the formation of the reinforcing phase and the composite itself are completed in a single step. A separate process to produce the reinforcing fibers, as in traditional short fiber reinforced composites, is unnecessary. Hence it is a potentially economical process to generate high performance materials; (2) LCP functions as a processing aid because of its extremely low melt viscosity, thereby making the use of higher viscosity thermoplastics possible.

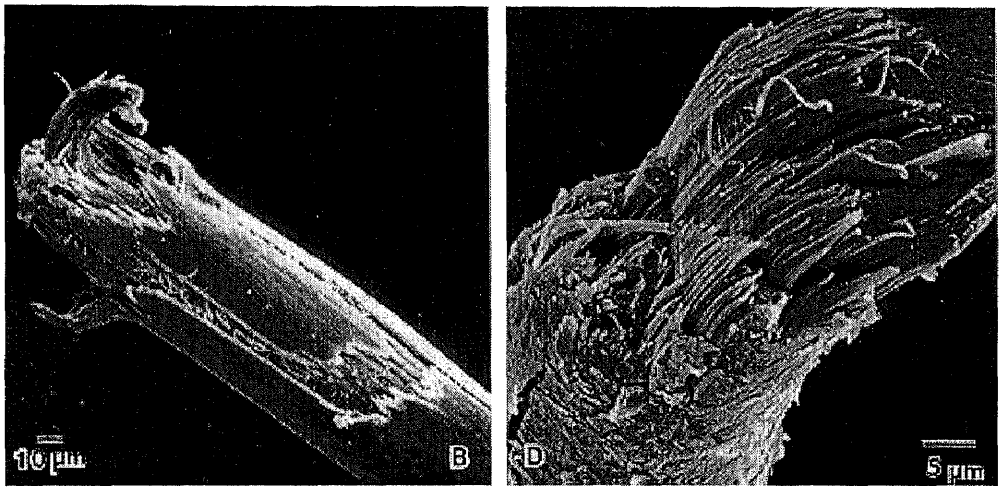

Figure 1.1 SEM fracture micrographs show the fibrillar and wood-like morphology in Vectra extrudates (Sawyer and Jaffe 1991).

The abilities of liquid crystalline polymers as processing aids and reinforcing agents originate from their propensity for forming highly oriented crystalline polymer chains when subjected to shear and elongational flows in melt phase, their long rod-like molecular conformation, and the strength and stiffness of their backbone chains. During processing, LCPs easily form fibrous morphology in oriented regions in the melt. The

fibrous nature of LCPs is readily seen at fracture surface being similar to wood (Figure 1.1). The morphology of LCPs gives the non-reinforced LCPs a self-reinforced capability, which is comparable to or sometimes surpasses that of glass fibers. The modulus of glass fibers is usually 86 GPa (McCrum et al. 1992) and the modulus of drawn LCPs is up to 105 GPa (Acierno et al. 1993) which depends on processing histories of LCPs. Therefore, it is possible to use LCP as reinforcements instead of glass fibers. Because of these characteristics of LCP, polymer blends containing LCPs have received considerable interest. These blends have been considered in many areas including electronic, automotive, commercial aircraft, medical, packaging.

The formation of fibrous morphology and achievement of higher mechanical properties from TP/LCP blends are obtained during processing. The present understanding about the effect of processing on the morphology development and mechanical properties of TP/LCP blends is not sufficient. This doctoral study is aimed at determining the morphology development and mechanical properties of TP/LCP during processing. Chapter 2 reviews the related studies and presents some comments on the studies. The motivations and objectives of this study are discussed in Chapter 3. Chapter 4 describes the experimental procedures including rheological measurements, injection molding, morphology observation, and measurement of mechanical properties. A numerical modeling and analysis using finite element method are presented in Chapter 5. A new method to calculate the flow in advancing melt front region is introduced. The morphology developments with processing parameters are discussed in Chapter 6. It provides the evidence of formation of LCP fiber during processing and the relationships between the distribution of LCP fiber and processing variables. The variations of mechanical properties of TP/LCP blends with processing parameters are presented in Chapter 7. The moduli of TP/LCP blends are measured to validate the predictions. Finally, conclusions and recommended studies are given in Chapter 8.

CHAPTER 2

LITERATURE SURVEY

2.1 Morphology of LCP Blends

In the morphological studies of LCP blends, important parameters are the formation, orientation, and aspect ratio of LCP fibers. Droplets, ribbons, and fibrils are the typical morphological units found in the blends, which may change from one type to another depending on the blend composition, rheological properties of each component of the blends, and flow conditions. Taylor (1934) was the first to analyze the elongation of a suspended immiscible droplet in a Newtonian fluid. According to Taylor's theory, the elongation of a Newtonian-fluid droplet depends on the ratio of the viscous to the surface tension force acting at the interface of the two phases. The former force is determined by the product of deformation rate (shear or elongation) and viscosity. The interfacial force is given by the ratio of interfacial tension to initial droplet diameter. Thus, for a given LCP blend, it could be assumed that the interfacial force is constant and that the only parameter that could be changed is the deformation rate in addition to the polymer viscosity. Obviously, the LCP blend system could be analyzed from the hydrodynamics point of view, similar to the case of rigid particles suspended in a fluid with the approximation of neglecting the viscoelastic effects.

2.1.1 Shear Flow Induced Morphology

Blizard and Baird (1987) studied the morphological development in shear flow of a blend of 60% hydroxybenzoic acid (HBA)/poly (ethylene terephthalate) (PET) (as a LCP) and polycarbonate (PC) (as a matrix). The experimental results of samples subjected to shear flow in cone and plate rheometer show that the LCP particles are in spherical form regardless of the shear rate. The diameter of the LCP particles becomes constant and

uniform by increasing the shear rate, and no fibrous structure was found. The reason that no fibrous structure was observed may be attributed to low shear rate (10 s^{-1}) in cone and plate rheometer. SEM micrographs of samples extruded through capillaries reveal fibrils of the LCP phase near skin region for shear rate from 45.7 to 457 s^{-1}. The authors did not give the size range of LCP fibrils. Blizard and Baird (1987), and La Mantia et al. (1990) demonstrated that the fibrils were formed and retained only in short capillaries. By increasing the length of the capillary, no fibrous structure was observed. Blizard and Baird (1987) explained this behavior by considering that the fibrils formed at the entrance of the capillary can be lost because of the relaxation of these structures in the shear flow field of the capillary. Obviously, the shear flow is not a key factor for the formation of LCP fibers according to the authors' explanation. An interesting phenomenon was found in the study of Blizard and Baird (1987), i.e. that the fibers tend to be of smaller diameter with increasing shear rate and the presence of phase inversion can be detected at high shear rate. The higher concentration of the LCP near the edge of the samples appears as a matrix from which near-spherical droplets of PC have been extracted. But the results mean that shear flow can really deform the LCP particles only at very high shear rate or at skin region. La Mantia et al (1990) pointed out also that the elongated particles could deform and break in shear flow into small particles if the viscosity of the matrix is much larger than that of the dispersed phase.

Beery et al. (1991a) also studied the shear flow of PC/LCP and polybutyleneterephthalate (PBT)/LCP blends in capillaries. They found in the PC/LCP blends that the LCP structure on the surface of the extruded strand changes with shear rates. At low shear rates up to 54 s^{-1}, the LCP appears as spherical particles that change to highly oriented fibrillar structure as the shear rate increases above 270 s^{-1}. The relative amount of fibrillar structure as well as the length of the fibrils gradually increases with increasing shear rate. The resulting diameter of fibrils is rather inhomogeneous. The LCP structure development with shear rates in PBT/LCP blends is different. In the case of

PBT/LCP blend, even at high shear rates above 2700 s^{-1}, the skin of the strand includes spherical particles of the LCP dispersed phase with occasional elongated particles, which is considerably different from the fibrillar appearance of the preceding PC/LCP blends. The authors explained these results on the basis of rheological analysis that the PBT viscosities lie below the LCP ones in the whole shear rates studied. Beery et al. (1991) observed the LCP morphological development at the center region of extruded strands in the PBT/LCP and Nylon6/LCP blends. No fibrous structures were found in center region of the strands both at low shear rates down to 27 s^{-1} and high shear rates up to 5400 s^{-1}. Actually, the shear rates in the center region are very low and the viscosities of matrix polymer are larger than those of the LCP in that region. It is worth noting that only if the viscosities of the two phases are similar or if the viscosity of the matrix polymer is moderately higher than that of the LCP, can fibrous structure develop (Beery et al. 1991a).

The skin-core morphology in the extrudates from capillary or extruder die mostly supports the effect of shear flow on the LCP fibrillar formation.

Seo et al. (1995) investigated the structure development of ethylene-propylene-diene terpolymer (EPDM) (as a matrix)/Vectra B950 (as a LCP) blends in a straight die with no converging section, and in converging dies with different converging angles: 7.5°, 10°, 30°, and 45°. SEM photographs reveal that the strand from the straight die has relatively large particles in the core region that seem to be deformed very little; more oriented materials exists at the outer region, which has undergone mostly shear flow. In the strands from converging dies, SEM photographs did not show any evidence of particle deformation in the core region even though extensional flow exists in this region. It seems that the extensional flow is not large enough to deform LCP particles, but the orientation of deformed particles near the outer region in converging dies with large converging angle is higher than that with small converging angle. Seo et al. (1995) also tested the effect of screw speeds on particle deformation in the die. As expected, more

macrofibrils and fibers appear in the outer region, because of more severe shearing action, and overall particle size is reduced. The conclusion drawn from these results is that shear flow can deform dispersed LCP particle only at the outer region.

Other typical studies related to the shear flow induced morphology of LCP blends include Isayev and Modic (1987), Weiss et al. (1987), and James et al. (1987). All of them reported on fibrous structure formations at high shear rate.

From all the above reported results, we found that fibrous structures of TP/LCP blends subjected to shear flow could be formed only at very high shear rates and mostly near the skin region. It could be concluded that shear flow is not a key factor in the formation of fibrous morphology of TP/LCP blends.

2.1.2 Elongational Flow Induced Morphology

In general, in elongational flow, droplets of the dispersed phase are deformed into fibrils. Evidence of this statement has been found for blends containing LCPs both in convergent flow at the entrance of the capillary (Kolhi et al. 1989, Blizard et al. 1987, Weiss et al. 1987) and in non-isothermal elongational flow (spinning processes) (La Mantia et al. 1990, Qin et al. 1993, Mehta and Deopura 1993, Lin et al. 1993, Carfagna et al. 1991). In this latter case, La Mantia et al. (1990) observed that relatively high draw ratios are needed in order to produce fibrils of the liquid crystal phase. Indeed, nylon/Vectra B950 blends show fibrils only for draw ratios larger than 50, but the author did not explain the reasons of this behavior. Lin et al. (1993) reported that the sample of PC/LCP blends with draw ratio of 25 shows uniform and well-defined LCP microfibrils. The diameter of the microfibrils is in the range of 0.05 to 0.3 μm. The experimental results of La Mantia et al. and Lin et al. show that the components of the TP/LCP blends are crucial to the generation of an LCP fibrillar structure. Lin et al. explained the morphology of PC/LCP *in-situ* composites using Taylor's theory on the deformation of Newtonian droplets suspended in another Newtonian fluid. They concluded that drawing increases the

deforming force, thus leading to a higher aspect ratio. Their experimental results also show that for given sufficiently large LCP droplets, the LCP phase can be readily stretched into the fibrillar form by drawing.

The viscosity ratio is also very important in the spinning process for the formation of LCP fibers as discussed in shear flow. Baird and Ramanathan (1990) showed that the LCP phase of the two blends, with the same matrix and different LCP samples having similar viscosity, has different size (droplets or fibrils) depending on the temperature dependence of the viscosity of the two components. Fibrils are formed and retained when the solidification behavior of the LCP component is similar to that of the thermoplastic matrix. Carfagna et al. (1991) studied the spinning process of the blends of polyetherimide Ultem 1000 as a matrix and the fully aromatic polyester K161 as a LCP, which have different glass transition temperatures T_g. Since the K161 has a T_g at 280 °C, over 70 °C higher than that of Ultem 1000, during spinning of the extrudate at room temperature, K161 quickly cools to a temperature close to its T_g, freezing any motion of the rods and not allowing further macromolecular orientation, by spinning. Therefore, the authors pointed out that the maximum level of orientation and deformation for LCP fibers in the blend is reached only inside the capillary. During fiber spinning, Ultem 1000 is drawn after the die exit, but the LCP fibers quickly stiffen due to the cooling. Thus, the LCP is almost unaffected by the fiber spinning, retaining the degree of molecular orientation reached inside the capillary. They also stressed the importance of shear viscosity ratio. To obtain a liquid crystalline phase, in the form of fibers with a high aspect ratio, LCP viscosity should be lower than that of matrix.

Heino and Seppala (1992) studied the effects of LCP content and different types of matrices on morphology developed during spinning process. At low LCP contents, the LCP phases can form only a few small fibers and no significant reinforcement is achieved, while at larger LCP contents there are enough oriented LCP fibers in the matrix (see Figure 2.1) to carry a significant amount of the load and reinforce the matrix. A clear

difference in morphology of PET/LCP blends can be seen in Figure 2.1. The left and right in Figure 2.1 are the morphologies of the core and skin regions, respectively. The thickness of the skin layer was generally about 100 -200 μm. Although the length of the LCP fibrils could not be measured accurately at the transversally fractured surface, they ranged from about 5 - 10 μm at lower LCP contents (5 and 10 wt%) to at least tens of μms at higher LCP contents. The diameter of the LCP fibers and spheres was mostly 1 -3 μm in the PET/LCP blends. The amount of fibrillar LCP domains increased with increasing LCP contents and increasing draw ratio. The effect of draw ratio could be seen

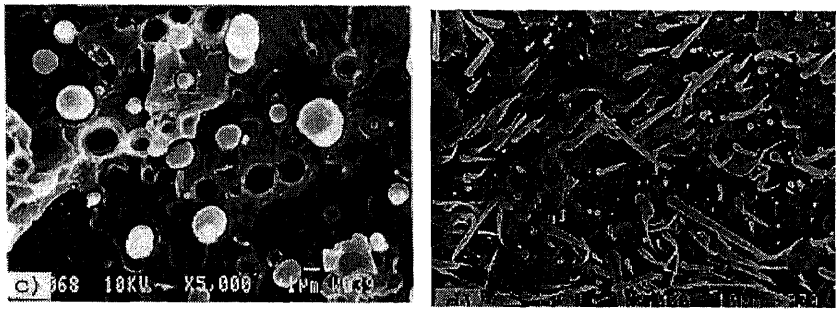

Figure 2.1 SEM studies of PET/ 10 wt% LCP blend (Heino and Seppala 1992).

from Figure 2.1, where the spherical particles in the core region at lower LCP contents are seen to be slightly deformed at even higher draw ratio. At 20 wt% LCP, fibers also existed in the core region, and at 30 wt% there were abundant fibers throughout the strand (see Figure 2.2); most of them continued to be well oriented in the skin region. At the highest LCP content, the skin layer was thicker (about 400 μm) than in other blend compositions. The polypropylene (PP)/LCP blends exhibited generally similar structure as the PET/LCP blends, but there was considerable difference in the size of the fibers. LCP formed longer fibrils in PP than in PET, ranging from tens of μms at the lowest LCP contents to hundreds of μms at the highest. In blends containing 20 and 30 wt% LCP, also larger diameter or thicker (up to 10 -20 μm) and flat LCP domains existed. The

formation of large LCP domains in PP is at least partly explained by shear viscosity ratio of LCP to PP.

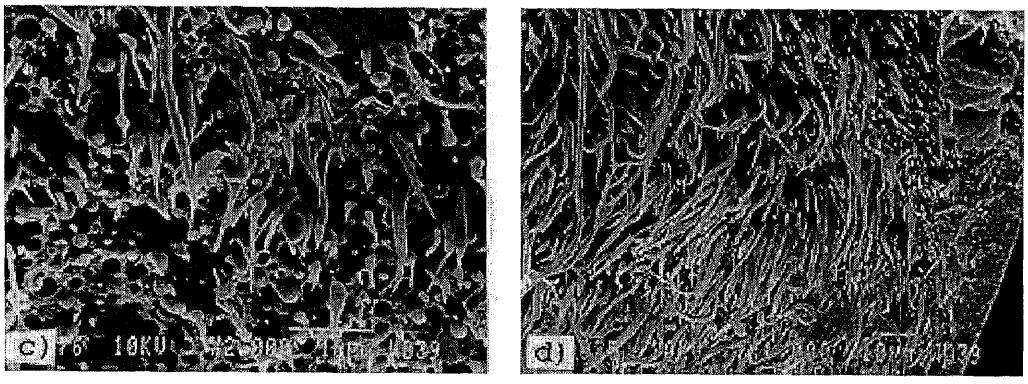

Figure 2.2 SEM studies of the core (left) and skin regions (right) of PET/30 wt % LCP blend (Heino and Seppala 1992).

Blizard et al. (1990) proposed a model to predict the morphology of extruded strands considering not only the rheological properties of the two components, but also the cooling conditions at the exit of the die. Their model is able to predict fibril formation and the morphology of the extruded strands and describes well their experimental results. Actually, this model only qualitatively predicts the trend of fibrillar formation and of morphological variation.

From all the above studies, it is shown that elongation flow is very critical in deforming LCP domains.

2.1.3 Morphology of Injection Molded Blends Containing LCPs

The injection-molding process is a highly complex process since the polymer melt is subjected to both shear and elongational flows during the filling stage. Many studies that consider the injection molding of the blends containing LCPs analyze the morphology of

the molded object. Significant differences between the skin layer and the core region are usually reported. These differences obviously relate to differences of flow and temperature history experienced by the material in the two regions. As mentioned in the previous section, elongational flow is much more effective than shear flow in inducing orientation in the fluid particles and, thus, in producing fibers from the LCP phase. In the injection molding process the polymer melt is layered on the skin after experiencing fountain flow at the melt front, which is an elongational flow aligning the material on the skin along the flow direction. Also the polymer melt in the core region may experience elongational flow if the cross section normal to the flow direction changes significantly along the path. This happens, for instance, downstream from the gate where a radial flow develops until the flow front reaches the cavity width. But in most cases, the effect of shear flow is superposed on the elongational one in the core region: shear gradient is a maximum at the solid-melt interface, and decreases to zero at the center. Larger gradients are required to elongate the LCP phase. Most of the observations reported in the literature may be explained within the above framework.

The effect of LCP percentage on the morphology of the injection molded specimens is shown by Siegmann et al. (1985). Polyblends with larger LCP content are found to produce fibrils more easily; this is probably related to larger particle dimensions in the initial polyblend morphology.

An interesting study was reported by Beery et al. (1991b). According to these authors, the structure of injection molded polyblends, containing Vectra A as a LCP and either PC, PBT or Nylon 6 as the matrix, was analyzed in relation to viscosity ratio and the interfacial force between the two phases. The thermoplastic matrices mentioned above

follow an inverse order with respect to high gradient viscosity values, and this order corresponds to a decreasing scale for the orientation of the LCP particles observed in the injection molded specimens. In particular, with PC (high viscosity) full alignment of LCP in the skin area and spheres or ellipsoids in the core were observed; the orientation in the core has to be related to converging flow towards the narrow section of tensile specimens or shear flow behind the melt front. High orientation of LCP, but with particles having larger diameter, was observed with PBT (second in viscosity). Some elongated particles were observed in the sample skin with the Nylon 6 matrix, while the sample core contains mainly spherical LCP domains with some fibrils especially at high levels of LCP. With the Nylon 6 matrix, which has the lowest viscosity and high interfacial forces, the skin appears to contain only a few elongated particles. The differences of the matrix effectiveness in inducing elongation in the LCP particles can be judged from Figure 2.3, where morphology of the LCP phase is shown, after complete extraction of the matrix polymer, at the skin of samples obtained with blends with 10% LCP content and either PC or Nylon 6.

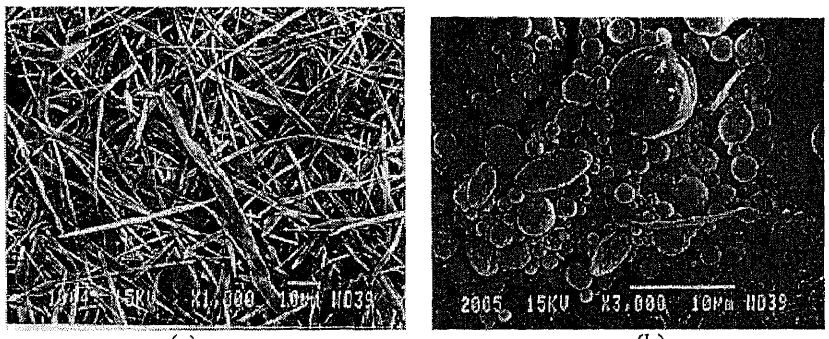

(a) (b)

Figure 2.3 Effect of matrix on the morphology of LCP blends taken from skin region: (a) LCP particles after extraction of PC from PC/10 % LCP blends, (b) LCP particles after extraction of Nylon 6 from Nylon 6/10 % LCP blends (Beery et al. 1991b).

Based on optical microscopy and scanning electron microscopy observations on Vectra A900/PET, a hierarchical system of layers and sublayers with different sizes and shapes of the fibrils was proposed by Silverstein et al. (1991). The model proposed included a macroscopic as well as a microscopic level. Starting from the macroscopic level, three macrolayers were detected. They are composed of a highly oriented skin, a less oriented central area, and disoriented core. The first two macrolayers were further divided into microlayers. The first sublayer or top sublayer, approximately 20 μm thick at the mold surface, consists of elongated fibrillar LCP domains 1-2 μm in diameter. These LCP fibrils are highly oriented in the flow direction. The sublayer next to top layer is approximately 120 μm thick. This second sublayer consists of cylindrical LCP domains 2 –5 μm in diameter oriented in the flow direction. These LCP domains are shorter, thicker, and less oriented than those in the top layer. The third sublayer is also approximately 180 μm wide and has still shorter, thicker, and less oriented LCP domains. The LCP domains in the fourth sublayer, approximately 100 μm wide, are similar to those in the third sublayer but are somewhat more oriented in the flow direction. The fifth or central sublayer, approximately 60 μm wide, has shorter, thick LCP domains that seem to be oriented in a direction normal to that of the flow direction. The authors pointed out that the oriented LCP structures in the first two sublayers result from the elongational flow in the injection direction along the cold mold surface. A 3-dimensional picture (see Figure 2.4) of the injection molded blends was constructed by the authors from the optical and electron micrographs which have revealed various parts of the structural hierarchy.

The above studies show that the morphology of blends is mainly dependent on viscosity ratio and the flow in the mold cavity, which is closely related to geometry and many processing parameters such as injection pressure, filling time or injection speed, mold temperature, and melt temperature. O'Donnell and Baird (1996) studied the effect of filling time and geometry of mold cavity on the morphology of Vectra A950/PC blends. In contrast, SEM photomicrographs show many long ribbons of LCP in the

samples with the same thickness molded in 0.8 second. In the 1.0 mm thick plaque, a more diverse LCP structure was observed with a wavy LCP morphology near core. The morphology of the 2.3 mm thick plaque shows a more uniform structure with a smooth morphological change from fibrils or ribbons near the skin to larger less deformed LCP structures near the core. The differences in morphology may be related to the differences in the flow and heat transfer that existed during filling in these two molds.

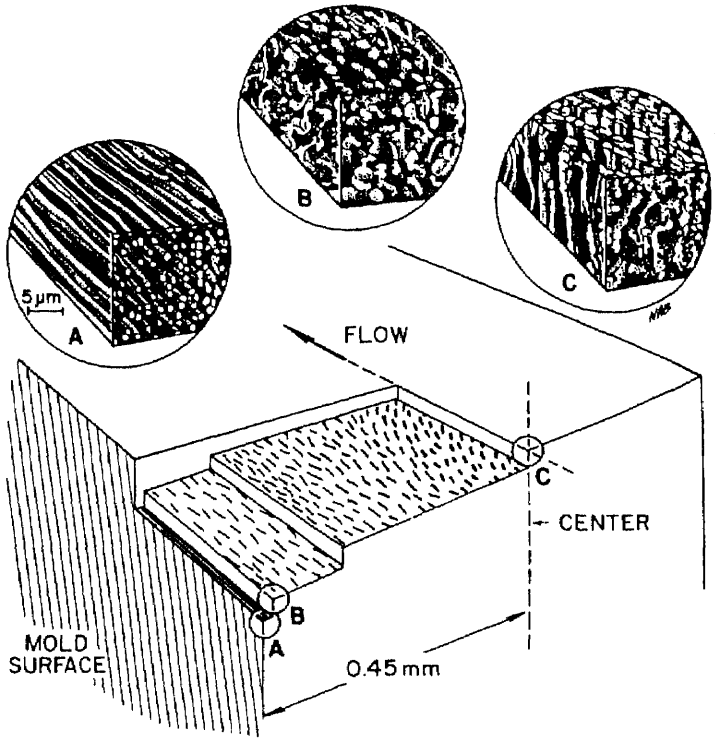

Figure 2.4 Schematic illustration of the hierarchical structure in LCP blends. LCP domains arranged in three sublayers (Silverstein et al. 1991).

2.2 Mechanical Properties of LCP Blends

One of the primary objectives of blending LCPs with thermoplastic polymers has been to use the LCP as reinforcement for flexible thermoplastic polymers. Mechanical properties of blends have been reported in a number of studies. Most of the researchers have

attempted to explain the changes in mechanical properties in term of the morphology of the LCP domains in the blends.

In nearly all the studies of LCP/polymer blends, the two components of the blends were immiscible. The size, shape, and distribution of the LCP phase depended on many factors such as composition, processing conditions, viscosity ratio of the component polymers, and the rheological characteristics of the matrix polymer. The first results of mechanical properties of extruded LCP blends were reported by Kiss (1987) on blends of polyether sulfone with different thermotropic LCPs including two HBA/hydroxy-2-naphthoic acid (HNA) copolyesters, A and B, and one copolyesteramide. All the blends show a remarkable increase of both tensile strength and tensile modulus; the elongation at break is, on the contrary, drastically reduced. Whereas the pure polymers, matrix and LCP, are almost unaffected by shear rate, the blends show a significant dependence on shear rate. Increasing the shear rate, both tensile strength and tensile modulus of the blend with copolyester A show a significant increase; as for the blend with the copolyester B the dependence on shear rate is reversed. Finally, the blend with the LCP copolyesteramide shows the same increase on the tensile strength observed for the blend with the two LCP copolyesters, however the tensile modulus is far higher.

Increased orientation of the dispersed LCP microfibrils formed by drawing can result in greatly improved mechanical properties of the blend. Dutta et al. (1990) observed an order of magnitude increase in modulus as the draw ratio was increased from 1 to 1000 for fibers extruded from blends of an HNA/poly-hydroxybenzoate (PHB)/hydroquinone (HQ)/terephthalic acid (TA) LCP with PC (see Figure 2.5). Jung and Kim (1988) studied mechanical properties and morphology of fibers of blends of polycarbonate and PET/60PHB considering, in particular, the influence of the draw ratio. The tensile modulus and the ultimate tensile strength of the fibers increased both with the LCP content and with the draw ratio. The elongation at break decreased sharply. The improvement of modulus and strength increased more than linearly with draw ratio.

According to the authors, at the highest draw ratio, the LCP droplets were transformed to continuous fibers because of the elongational flow experienced during drawing. Lin et al. (1993) also studied the variations of elastic modulus and tensile strength with draw ratio for PC/Vectra B950 (70/30, wt%). The elastic modulus of the strand with a draw ratio of 35 is more than three times that of undrawn one. The highest value of elastic modulus is 19 GPa for composite strands. The tensile strength of the strands with 30 wt% LCP rises sharply with increasing draw ratio up to ~15. The highest value of tensile strength is 146 MPa. Again these increments are attributed to microfibril formation of the LCP phase, and more importantly to the LCP molecular orientation. The authors also pointed out that all samples broke in a brittle mode despite the high ductility of the PC matrix. No necking was detected, and the elongation to break was less than 2%.

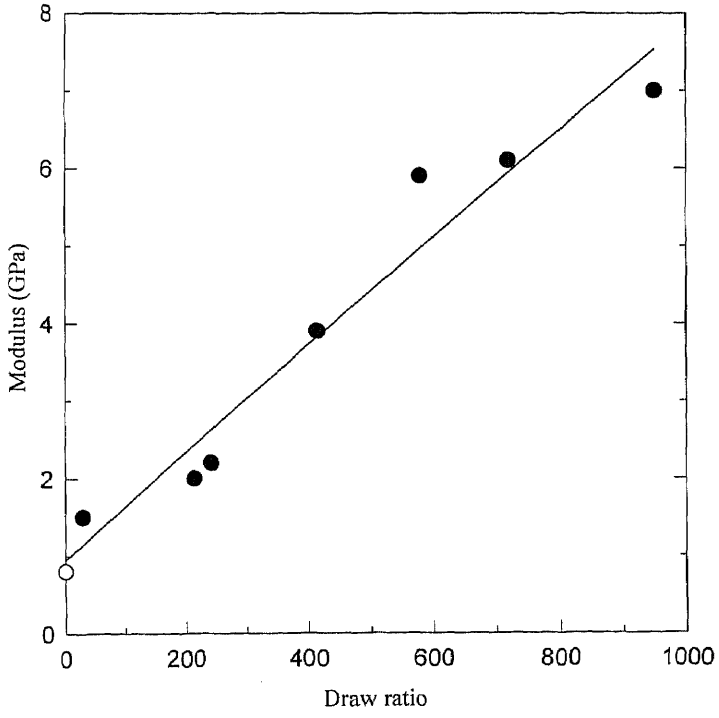

Figure 2.5 Effect of draw ratio (DR) on the tensile modulus of 20% LCP/80% PC blend (Dutta et al. 1991).

Obviously, the improvement of tensile strength and tensile modulus due to the shear rate or melt drawing was a result of improved orientation and fibrillation of the dispersed LCP domains. These results demonstrate that the modulus and strength can be markedly improved by varying elongational rate and shear rate.

A number of studies have considered the effect of LCP concentration on the mechanical properties. Zhuang, et al. (1988) found that adding small amount of 40PET/60PHB to PET, PC, polystyrene (PS) increased the modulus and tensile strength of compression molded films, extrudates, and melt spun filaments; the elongation at break was, on the contrary, drastically reduced in all cases. The modulus was also found to increase with LCP percentage studied by Crevecoeur and Groeninckx (1990).

Mechanical properties of injection molded blends of thermoplastic polymers and thermotropic LCP materials were first reported by Siegmann et al. (1985) with reference to a blend of an amorphous polyamide and Vectra A. In particular, the modulus was found to undergo a 1.5-fold increase by addition of 25% of LCP and elongation at break underwent a dramatic decrease with only 5% LCP. These two features are quite general with blends with thermotropic LCPs and are related to the morphology that builds up during the processing. In injection molded objects, the change of mechanical properties is mainly related to the structure at the sample skin. Indeed, the same authors found that the core had a lower modulus and a higher elongation. With this system, ultimate strength was found to undergo a 1.3-fold increase by addition of 25% LCP, however the ultimate strength is very sensitive to adhesion between components and thus its behavior may change with the system considered. Kiss (1987) reported data with reference to many systems having 30% LCP. He also found that elongation at break had much lower values

than the matrix, the modulus increased at least as expected on the basis of the mixture rule and the strength often increased, but in some cases decreased by the addition of LCP. Surprisingly, his data showed values of flexural moduli not larger than the tensile ones.

Isayev and Modic (1987) reported mechanical properties both in the flow and in the transverse direction. Along the flow direction the results are in line with those previously considered and with the morphology of the system, in particular, the modulus increases and impact strength decreases much faster with LCP content. Along the transverse (tangential) direction the elongation at break decreases even more quickly than along the flow direction; conversely the modulus is higher than in both pure components. In the same paper, the authors reported that a decrease of flow rate reduces the increase of both modulus and strength in the flow direction; an opposite effect of flow rate on the mechanical properties was reported by Brinkmann et al. (1991). The effect of matrix is shown in the work by Siegmann et al. (1985) also with reference to mechanical properties. The results are in line with their morphological observations mentioned previously. In particular, modulus increases with amorphous nylon (AN), PC and slightly with PBT, tensile strength increases with AN, PC and remains essentially unchanged with PBT matrix; both modulus and strength decrease as LCP content increase in a Nylon 6 matrix.

O`Donnell and Baird (1996) studied the effect of injection molding conditions on the mechanical properties of an *in situ* composite. The variables of filling time, mold temperature, and the thickness of mold cavity were analyzed. The flexural moduli increase from 3.9 to 5.2 GPa, and tensile moduli increase from ~2.9 to 4.7 GPa with filling time from 0.8 to 5 s for both 1.5 mm molds. This same property / processing trend

occurs for 2.3 mm mold: the flexural moduli increased from 2.62 to 4.08 GPa and the tensile moduli increased from 2.12 to 3.08 GPa while the filling time is increased from 1.3 to 7.8 s. The authors also found that the transverse flexural properties were unaffected by changing filling time. The average transverse modulus for the 1.0 mm thick plaques was approximately 1.5 GPa, and for the 1.5 and 2.3 mm thick plaques was 1.4 GPa. Flexural modulus for the thin molds were larger than that for the thick molds. The authors did not obtain a simple relationship between mold temperature and mechanical properties for the PP/LCP blend, even for pure LCP; these results are different from the results reported by Suokas (1989) with reference to a pure thermotropic LCP. Suokas found that the tensile modulus of pure LCP decreases with increasing mold temperature. Yi et al. (1996) analyzed the tensile modulus and strength of PC/LCP blends at the melt temperatures of 280 and 320 ^{o}C and at the volume flow rates of 8 and 80 cm^3/s, and found that there are larger tensile modulus and strength at lower melt temperature, and lower volume flow rate. At the injection conditions of lower melt temperature and lower volume flow rate, larger average aspect ratio of LCP fibers was observed.

2.3 Prediction of Modulus of LCP *In-Situ* Composites

It is important to predict the morphology and mechanical properties of LCP based blends. Such a modeling effort will help determine the structure-property relations and structure/property-processing relations, and also determine the optimal processing conditions for this new class of materials. Most of the recent studies were experimentally concerned with the relationships between the mechanical properties and morphologies of LCP based blends. Few researchers conducted studies on developing a model

incorporating processing variables, to predict the mechanical properties and morphology of the blends. Some investigators modeled the mechanical properties of the blends based on the traditional composite theories (Isayev and Modic 1987, Kolhi et al. 1989, Shin et al. 1992, Kyolani et al. 1992). Isayev and Modic (1987) based their calculations on the assumption that the blends of PHB/HNA and PC could be treated as unidirectional fiber-reinforced composites. Their experimental data deviated from the calculation. Kohli et al. (1989) in their studies on the blends of LCP (PHB/HNA/HQ/TA) and PC reported that the moduli of highly drawn melts could be modeled by the simple rule of mixtures:

$$E = E_f V_f + E_m (1 - V_f) \tag{2.1}$$

where E, E_f, and E_m are the moduli of composite, reinforcing LCP, and PC, respectively; V_f is the LCP volume fraction. Kohli et al. obtained a good agreement between the experimental results and the predictions of the model. An explanation for the good agreements was the high alignment of the LCP fibers in the draw direction and the formation of almost continuous fibers. But most processing methods cannot give such a perfect structure. Thus, theoretically, the traditional composite theory can not describe the mechanical properties of TP/LCP blends for the following reasons:

- LCP droplets are not totally fibrillated, particularly at low shear and elongation rates. The aspect ratio of LCP fibers in final composite-like structure of TP/LCP blends is distributed over a wide range.
- The fibers are not perfectly aligned in the longitudinal direction, especially when subjected to shear flow.
- The modulus of LCP fibers varies with the aspect ratio of LCP.

Real morphologies, orientation, and aspect ratio of LCP in a matrix vary with the concentration of LCP, viscosity ratio of LCP to matrix, processing variables. The model to predict the mechanical properties of TP/LCP blends must involve these factors. Therefore, traditional composite models cannot be used for TP/LCP blends.

Lin and Yee (1994) developed a model that was based on the traditional composite theory and only considered the pure elongational affine deformation of TP/LCP blends in a spinning process. The LCP phase itself was envisaged as a composite of a perfectly oriented chain aggregate and a randomly oriented chain aggregate. The fraction of the perfectly oriented chains, f, is given by the order parameter of the LCP chains assuming affine deformation as follows:

$$f = \frac{2\lambda^3 + 1}{2(\lambda^3 - 1)} - \frac{3}{2}\frac{\lambda^3}{(\lambda^3 - 1)^{1.5}}\sin^{-1}\left(\frac{\lambda^3 - 1}{\lambda^3}\right)^{0.5} \tag{2.2}$$

where λ is the draw ratio. The elastic modulus of the LCP phase can be expressed by the following formula based on the composite model:

$$\frac{1}{E_f} = \frac{f}{E_c} + \frac{1-f}{E_r} \tag{2.3}$$

where E_f is the longitudinal elastic modulus of the reinforcing LCP fibers; E_r is the elastic modulus of the randomly oriented chain aggregate; E_c is the elastic modulus of the perfectly oriented chain aggregate along the chain direction; f is calculated using Eq. 2.2. The elastic modulus of TP/LCP blends can be modeled by the Halpin-Tsai composite model with E_f as the modulus of dispersed phase and $2\lambda^{1.5}$ as the aspect ratio of the LCP fibers. A good agreement was obtained between the experimental results and the predictions except at higher draw ratios. The predictions were larger than experimental

data at higher draw ratios. The authors did not explain the reason for this deviation at higher draw ratios. Due to the complex flow in polymer processing, Lin's and Yee's model cannot be extended to other processing techniques except spinning because it is based solely on the pure and uniform elongation flow.

Based on the layered structure of injection molded TP/LCP blends, Yi et al. (1996) predicted the modulus of each layer using the Cox-Darlington model as follows:

$$E_i = E_f * V_{fi} * n_l + E_m * (1 - V_{fi}) \qquad i=1, 2, 3 \qquad (2.4a)$$

with

$$n_l = \sum_j^M h_j (1 - \frac{\tanh x}{x}) \qquad (2.4b)$$

and

$$x = \sqrt{\frac{2}{\ln(2/V_{fi} * \pi/\sqrt{3})} * \frac{E_m/E_f}{1+V_m}} * (\frac{L}{D}) \qquad (2.4c)$$

where E_f and E_m are the elastic moduli of fiber and matrix, respectively; V_{fi} represents the fiber volume fraction in each layer; n_l is the modifying factor, which depends on the fiber aspect ratio (L/D) and volume fraction; V_m is the Poisson's ratio. This model does not involve the effects of processing parameters. The authors derived an approximate linear function between the elastic modulus of LCP fiber and aspect ratio of fiber based on the experimental data. This approach allows the modulus of the blends to be correlated with the size of dispersed phase. The data (see Table 2.1) used to derive the approximate linear function by the authors will be applied to calculate the modulus of LCP in this dissertation study using a different approach.

Table 2.1 Aspect ratio and modulus of Vectra A950 (Yi et al. 1996)

Aspect Ratio	10	11	15	21
Modulus (GPa)	20	22	22.3	25

2.4 Comments on Previous Studies

From the above reviews, some comments can be addressed as follows:

1. According to the Taylor theorem, it is possible to analyze the deformation of LCP particles from a hydrodynamics point.
2. Shear flow could result in the deformation of LCP particles. But the deformation is very limited. Distinct deformation could be observed only at very high shear rates.
3. Elongational flow is very effective for deforming the LCP particles. Compared with the elongational deformation, shear deformation may be neglected.
4. There have been many studies on the influences of simple flows, such as pure elongational flow and shear flow, on the formation of LCP morphology. But it is necessary to investigate the formation of LCP morphology under complex flows in the injection molding.
5. Several studies have reported on the variation of the mechanical properties of LCP blends with both the LCP concentration and the draw ratios of LCP fibers. However, it is essential to understand the effect of processing parameters on the properties, particularly variables in injection molding, by far the most important and popular process in the plastics industry.
6. It is essential for engineers to calculate the mechanical properties of materials as applicable to product designs. Only a few studies have been concerned in the prediction of the mechanical properties of TP/LCP blends. It is obviously necessary to develop a model to predict the properties of injection molded TP/LCP blends.

CHAPTER 3

MOTIVATION AND OBJECTIVES

The formation of fibrous morphology and achievement of higher mechanical properties from TP/LCP blends do not result from the simple mixing of these polymers but from processing of the blends in a manner that forms a reinforcing fiber-like LCP structure within the blends. As discussed in Chapter 2, many researchers have studied the fiber formation and development of the LCP blends in simple manufacturing processes, such as capillary extrusion and spinning, and the effect of these manufacturing processes on the mechanical properties of LCP blends. They found that the morphologies and mechanical properties of the blends are controlled by the melt flow and by the rheological properties of the two components of TP/LCP blends and, qualitatively, analyzed the rheology-morphology and flow-morphology relationships. But the most popular manufacturing processes in polymer industry are injection molding and screw extrusion. In these manufacturing processes, melt flow is more complex; the role of process parameters is the most important in the control of the final properties of polymer products. Obviously, the studies of morphology formation and development in the simple manufacturing processes and qualitative analysis for these relationships are not sufficient for the application of the new materials. It is very important to enhance the basic knowledge on the morphology development and mechanical properties of LCP blends in one of the most popular processes, such as injection molding. Actually, there is little work done on the effect of process parameters on morphology development and mechanical properties of injection molded TP/LCP blends as discussed under literature review.

The primary objective of this work is the determination of the morphology development and the variation of mechanical properties of TP/LCP blends with process

parameters. Due to the complex relationship between morphology development and flow, a numerical approach was developed to simulate the formation of LCP fibers. A new method incorporating process parameters was developed to calculate the mechanical properties of the *in situ* composites. Using flow dynamics to simulate the morphology development and to predict mechanical properties will be helpful to understand the process in detail. Specifically, in this study, the following tasks are performed:

1. To set up a series of experiments including injection molding, morphology examination, measurement of mechanical properties, and rheological measurement.
2. To develop a computational process to simulate and analyze the injection process.
3. To develop a new method to analyze the flow in the advancing melt front region.
4. To conduct experimental studies in conjunction with the computer simulation and analysis to better understand the formation and development of fibrous morphology.
5. To develop a new method incorporating the processing parameters to calculate the moduli of PET/LCP blends in order to better understand the effect of processing parameters on the mechanical properties with experiments and simulation.

CHAPTER 4

EXPERIMENTAL SETUP AND PROCEDURES

The objectives of the experimental studies are to evaluate the variation of morphologies and mechanical properties of PET/LCP blends as a function of processing parameters, to explore the possibility of improving mechanical properties of the flexible thermoplastic, and to validate the predictions of the numerical analysis developed in this study. There are four types of experiments to be performed in this study:

- Measurement of rheological properties for the LCP blends and their components .
- Manufacturing of samples using injection molding at different processing conditions.
- Microscopic analysis of the morphologies of the LCP blends, and measurement of the thickness of the skin layer.
- Measurement of mechanical properties of the LCP blends.

4.1 Materials

4.1.1 Poly(ethylene terephthalate) (PET)

Poly(ethylene terephthalate), supplied by Shell Company as Cleartuf 7202C, was used as a matrix in this study. Its chemical structure is shown in Figure 4.1. PET is one of the most commercially important polymers and is suitable for the manufacture of fibers,

beverage-bottles, and films (magnetic recording tape and photographic films). PET has

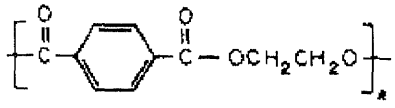

Figure 4.1 Chemical structure of PET

high strength, rigidity and toughness, excellent dimensional stability, low coefficient of friction, high transparency to light, and good resistance to chemicals and grease, but it is moisture sensitive and should be dried prior to final processing to ensure optimum physical properties of the final products. The main characteristics of PET, provided by the supplier, are shown in Table 4.1.

Table 4.1 Characteristics of Cleartuf 7202C (C7202C) and VECTRA A950 (VA950)

Material	Processing Temp. (°C)	Melt Temp. (°C)	Density kg/m^3	Thermal Conductivity (W/mK)	Specific Heat (J/kgK)	Tensile Modulus (GPa)
C7202C	265 - 290	257	1.2E3*	0.141*	1.356E3	2.9
VA950	280 - 310	280	1.4E3*	0.322*	3.594E4	9.7

- Data for 250 °C
-

Typical drying conditions for the PET are an air temperature of 175 °C, 4 hours residence time at a dehumidifier, and a minimum air flow rate of 1.0 cubic foot per pound of the PET, as suggested by the supplier. In this study, different drying conditions (Mehta and Deopura 1993) for the PET were used, including a drying temperature of 100 °C, a residence time of 12 hours in an oven, and a vacuum condition.

4.1.2 Liquid Crystalline Polymer (LCP)

The liquid crystalline polymer (LCP), supplied by Hoechst-Celanese as VECTRA A950, is a random aromatic copolyester of 73 mol% hydroxybenzoic acid (HBA) and 27 mol% hydroxy-2-naphthoic acid (HNA). Its chemical structure is shown in Figure 4.2. Due to

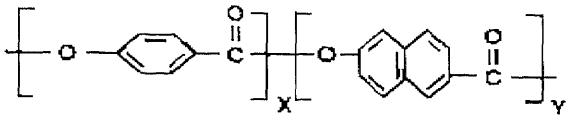

Figure 4.2 Chemical structure of LCP

the high modulus and strength, good dimensional stability, and high thermal stability, LCPs have many special applications such as electronic components (e.g., computer memory modules), housings for light-wave conductors, and a variety of aerospace applications. In this study, LCP was used as a reinforcing component. This is due to easy formation of LCP fibers in elongation and shear flow, and their good mechanical properties. The main characteristics of VECTRA A950, provided by the supplier, are listed in Table 4.1

The supplier suggests that VECTRA A950 should be dried before processing for the purpose of reducing the possibility of hydrolytic degradation. In this study, drying conditions (Yi et al. 1996) for the LCP were used including a drying temperature of 100 °C, a drying time of 12 hours in an oven, and a vacuum condition.

4.2 Measurement of Rheological Properties

Rheological measurements are very useful in simulations, determination of large-scale processing conditions, and structure development in TP/LCP blends. In this study, a

capillary rheometer was used to measure apparent shear viscosity over a range of shear rates encountered in injection molding.

4.2.1 Rheological Instrument

The rheological instrument used here is the Monsanto Automatic Capillary Rheometer as shown in Figure 4.3. The shear viscosity of materials used in this investigation as the

Table 4.2 Specifications of Monsanto automatic capillary rheometer

Shear Rate Range (1/S)	Viscosity Range (Pa.s)	Piston Force (kgf)	Temperature Range (°C)	L/D of Orifice	Diameter of Orifice (mm)
$1 - 10^4$	5 - 24E6	18 - 360	70 - 340	15	1.05

function of shear rate is measured using the rheometer. The rheometer consists mainly of rheometer pressure stand, rheometer extruder barrel, ram assembly, programmer and temperature control cabinet, and orifice. The test material is placed in an electrically heated barrel. A compressed gas driven piston applies a controlled force on the material and extrudes it through a capillary die (orifice). By adjusting the pressure on the piston and recording the extrusion time measured, the relationship between the viscosity and shear rate can be determined. The specifications of the rheometer are listed in Table 4.2.

4.2.2 Viscosities

The PET and LCP were dried in a vacuum oven at 100 °C for 12 hours before measurement, and were loaded directly from the oven into the rheometer barrel, the

objective of which is to avoid the effect of moisture on the measurement of viscosity. All measurements were done with a single capillary (L/D of orifice is 15) and no end corrections were applied to the data. The PET was tested at 260, 280, and 290 °C and the LCP at 280, 290, and 310 °C. The readings obtained from the measurements are the piston pressure and extrusion time. Shear rate and apparent shear viscosity are calculated using the following equations:

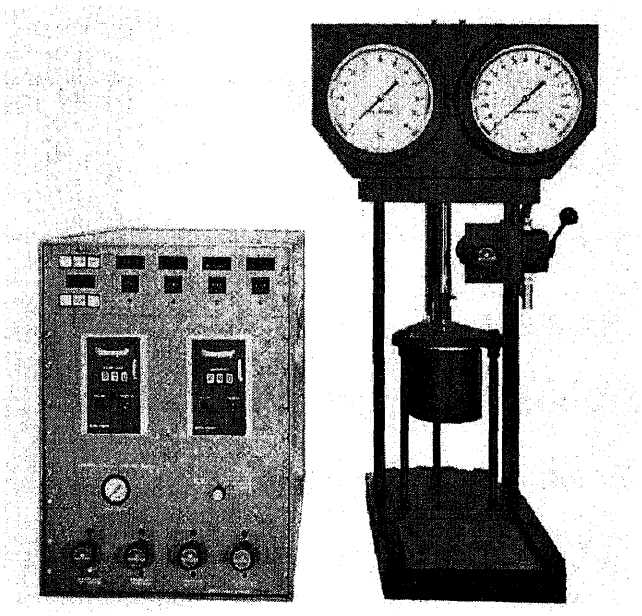

Figure 4.3 Automatic Capillary Rheometer.

$$\dot{\gamma} = \frac{4V}{\pi r^3 t} \tag{4.1}$$

where $\dot{\gamma}$ is the shear rate, sec.$^{-1}$; V is the volume of material extruded, 0.2883 in^3; r is the orifice radius, inch; t is the extrusion time, second (read from testing), and

$$\eta_a = \frac{Fr^4 t}{8R^2 LV} \times 6.895 \times 10^3 \tag{4.2}$$

where η_a is the apparent melt viscosity, N.s/m^2; F is the load on the ram and is equal to 5 times of the piston pressure (read from testing, unit: psi), lbf; R is the barrel radius, 0.188 inch; L is the orifice length, inch.

In this study, the shear viscosity of PET/LCP blends were measured at different LCP concentrations. Before measurement, the PET and LCP were mixed using a single

Table 4.3 Extruder variables and extrusion conditions for PET/LCP blends for all runs

Diameter of Screw (inch)	Ratio of Length to diameter	Revolution of Screw (rpm)	Temperatures of Barrel (°C)	Temperature of Die (°C)
1	15	50	1st Zone: 260 2nd Zone: 288	288

screw extruder (Model D-3002, produced by C. W. Brabender) and pelletized. The extrusion conditions are listed in Table 4.3. Drying conditions for the pelletized blends before use are the same as the conditions used to dry the PET and LCP in the measurement of shear viscosity. The blends were tested at 260. 280, and 290 °C.

4.3 Injection Molding

4.3.1 Injection Molding Machine

The injection molding machine used in this study is Toyo Plastar Ti-90G, produced by Toyo Machinery, a reciprocating screw injection molding machine. All samples used in the measurement of mechanical properties and the microscopic studies of morphology are injection molded with this machine at different processing conditions. The machinery consists mainly of an injection unit, a clamp unit, and heating and cooling system. The

details of the injection unit and clamp unit are illustrated in Figure 4.4. As the screw turns (40 - 80 rpm) the solid plastic in pellet or granular form stored in the hopper is

Table 4.4 Specifications of Toyo Plastar Ti-90G

Clamp Force (tons)	Shot Capacity (in^3)	Plasticating Capacity (lb./hr.)	Screw Diameter (in^3)	Max. Injection Pressure (psi)	Max. Inject. Rate in^3/min	Max. Inject. Speed in/min.
90	9.9	157.5	1.57	24088	624	5.372

conveyed forward, melted and pressurized. As plastic melts and is accumulated in front of the screw tip, the injection cylinders are free to force the screw forward rapidly, injecting the melt into the empty mold cavity through the gate of the mold.

The speed of the screw's forward axial movement is defined as the injection speed, which is one of important processing parameters and its effect on the structure and the properties of the LCP blends was investigated. Mold temperature is controlled by circulation of liquid coolant, either soft water or oil, which is arranged to flow turbulently through drilled channels in the mold cavity and core plates. In this study, soft water is used as the coolant. The main parameters of Toyo Plastar Ti-90G are shown in Table 4.4.

4.3.2 Preparation of Materials and Injection Molded Samples

PET pellets were manually mixed with LCP pellets and then dried in a vacuum oven at 100 °C for 12 hours before use, and loaded into the hopper of the injection molding machine. In order to evaluate the effect of LCP concentration on the morphology and

mechanical properties of LCP blends, blends were prepared with 5, 15, and 25 weight percent of LCP concentrations.

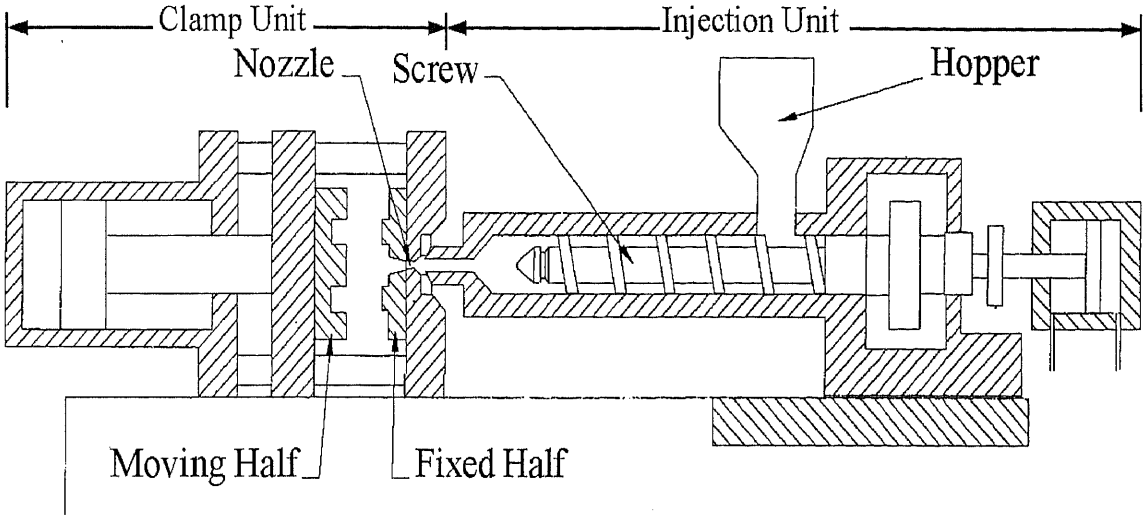

Figure 4.4 Injection unit and clamp unit.

The injection molded part used in this study consists of two portions: a dogbone and a runner as shown in Figure 4.5. The dogbone is a tensile test specimen referenced to ASTM D 638 Type I. The volume of runner and tensile test specimen is 0.8235 in^3. Considering the volume of nozzle, sprue, and the flash in parting plane, the total injection volume in one injection shot is set to be 1.25 in^3 in this investigation.

4.3.3 Processing Conditions and Procedure

To evaluate the effect of processing parameters on the morphology and mechanical properties of the LCP blends, and to explore the possibility of improving mechanical properties of the flexible thermoplastics, the samples of the blends were manufactured using the Toyo Plastar Ti-90G, under different processing parameters. The most

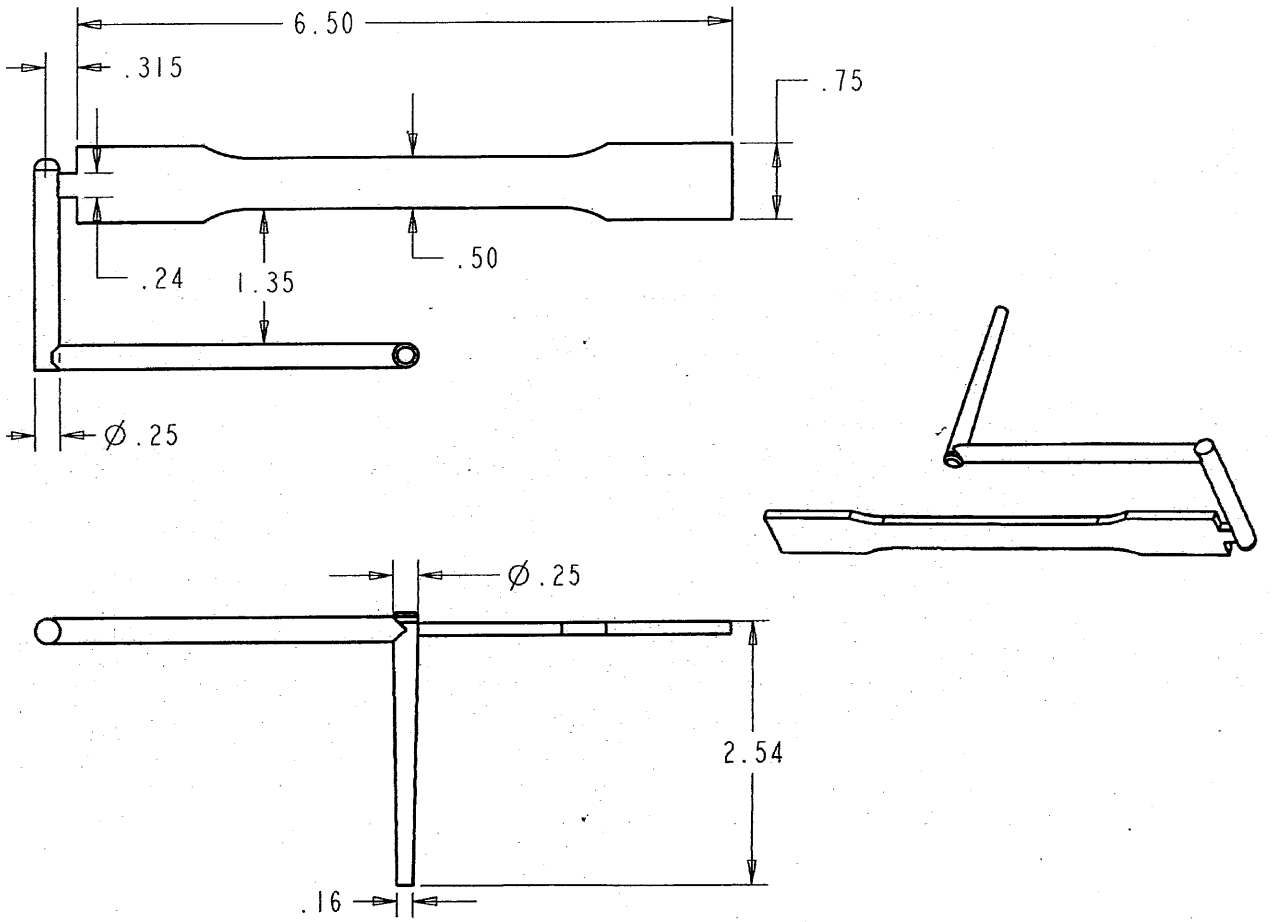

Figure 4.5 A dogbone and a runner.

important parameters in injection molding are the injection speed (or filling time), mold temperature, and melt temperature. In this investigation, the three parameters were varied to determine their effects on the morphology development and mechanical properties of the LCP blends.

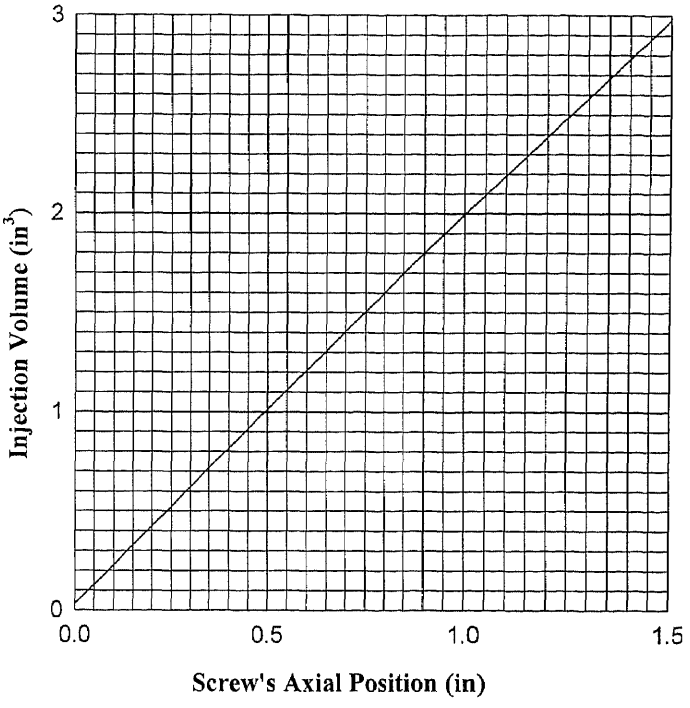

Figure 4. 6 Relationship between injection volume and screw axial position.

In injection molding, many machines equipped with sophisticated process controllers are capable of injecting the melt at a variable rate with typically 3 or ten control stages. Variable-rate injection of the melt provides many advantages. For example, a high injection speed is needed at the thinner portion of mold cavity to protect against early solidification of melt or short shots. But excess flash on the parting plane of mold will result if the flow speed of melt still is maintained high when the melt reaches

the extremities of the mold cavity, which shows that lower injection speeds are desired. Toyo Plastar Ti90-G provides three control stages for injection speed. In this experiment, higher injection speeds were used when melt fills the runner and the mold cavity; lower injection speeds was used when the melt reaches the extremities of the mold cavity. Variable-rate injection of the melt is completed by adjusting the ram speed. The two parameters, which need to be set for variable-rate injection, are the stroke of ram or screw axial position and the injection speed, expressed as the percentage of the maximum injection rate (MIR). The stroke of the ram or screw axial position can be determined using Figure 4.6, which shows the relationship between injection volume and the screw axial position. The screw axial position corresponding to the total volume of 1.25 $inch^3$ in one injection shot is 0.625 inches. During filling of sprue and runner, the screw is set to move from 0.625 to 0.5 inches according to the volume of the sprue and the runner. The screw axial position is set to be from 0.5 to 0.05 inches while the mold cavity is filled. The rest of the stroke from 0.05 to 0 is used to pack the cavity. Because this study has focused on the morphological development during filling of the mold cavity, which takes place under the second control stage for injection speed, the injection speeds or the percentages of MIR under the first and third control stages were kept constant in this experiment and the injection speeds under the second control stage were varied to evaluate their effects on the morphology development and mechanical properties. The injection speeds are listed in Table 4.5.

Melt temperature is defined as the temperature of the molten polymer exiting from the nozzle of the injection molding machine. The melt temperature was adjusted by changing the barrel temperature setting of the injection molding machine. Since the

diameter of the nozzle is very small (about 4 - 5 mm), the heat from the heater near the nozzle is easily transferred to the polymer melt, which enables its temperature to be close to nozzle temperature setting. In general, the difference between the melt temperature and the setting is assumed to be compensated for by the viscous heating effects in the nozzle. Therefore, the melt temperature is approximately equal to the temperature at the nozzle. The barrel temperature settings are listed in Table 4.6. In Toyo Plastar Ti90-G, multiple control zones (five zones) of barrel temperature were used. The temperature of the nozzle was changed in order to adjust the melt temperature. In this study, we used the settings of temperature at the nozzle to approximately express the melt temperature.

Table 4.5 Injection speeds and screw axial position in one injection shot

Process	Filling Runner	Filling Mold Cavity	Packing
S. A. Position (in)*	0.625 - 0.5	0.5 -0.05	0.05 - 0.00
Injection speed 1 (%)	20	10	0.6
Injection speed 2 (%)	20	12	0.6
Injection speed 3 (%)	20	14	0.5
Injection speed 4 (%)	20	16	0.4

*: S. A. Position = Screw axial position in one injection shot.

Mold temperature usually indicates the temperature of cavity surfaces which are in contact with the melt. Mold temperature directly influences the cooling rate in the mold cavity. In this investigation, the coolant temperature was used as the mold temperature because the coolant temperature is proportional to the mold temperature, and in our simulations the coolant temperature is used as the input data. The adjustment of the

mold temperature was completed by changing the setting of the coolant temperature. Generally, molding is conducted with the mold temperature between 20 °C and 150 °C, depending on the polymers. Therefore, coolant temperatures in this experiment were set to be 18, 35, 50, and 57 °C.

Table 4.6 Barrel temperature settings

Barrel Position	Nozzle	1st Zone	2nd Zone	3rd Zone	Feed Zone
Temperature 1 (°C)	304	298	287	270	232
Temperature 2 (°C)	310	304	287	270	232
Temperature 3 (°C)	320	310	287	270	232

Other processing conditions used in this experiment were kept the same for all runs, which are listed in Table 4.7.

Table 4.7 Other processing conditions used in this study

Packing Pressure (psi)	Holding Time, (sec.)	Screw Rotation Speed* (rpm)		Back Pressure* (psi)	
700	15 – 20	50	5	0	2418

*: The first value is applied to screw's axial position from 0 to 0.623 inches.
The second value is applied to this position from 0.623 to 0.625 inches.

Before starting to manufacture samples, the machine need to be preheated about 30 to 60 minutes in order to obtain a steady state, and then all processing parameters are set except barrel temperatures which are set before preheating. When starting to produce samples or changing the concentration of LCP, the machine need to be cleaned using 5 ~

10 injection shots in order to eliminate the effect of residual materials in the machine barrel on the quality of injection molded samples. The 5 ~ 10 injection shots are also needed to reach a steady state when processing parameters such as injection speed and melt temperature are changed. From the injection pressure curve recorded on-line, the steady state can be determined. Figure 4.7 shows the variation of injection pressure as a function of screw axial position. When the machine reaches a steady state, the pressures of all injection shots fall into a narrow range.

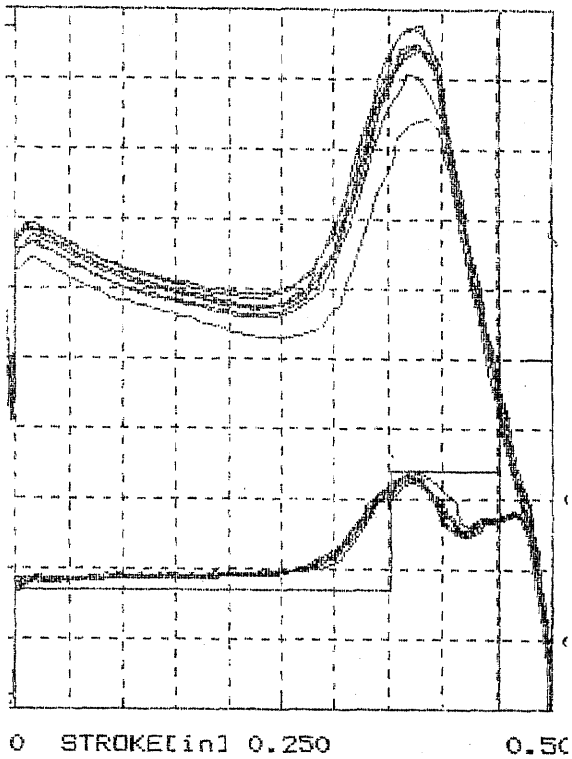

Figure 4.7 Injection pressure (top) and injection speed (bottom) as a function of screw axial position.

About 10 samples under each processing condition and LCP content were made for the measurement of mechanical properties and morphological observation.

4.4 Morphology Examination

4.4.1 Sample Preparation

The samples (approximately 10 mm long, 6 mm width, and 0.125 mm thick) for morphological analysis were cut from the injection molded parts. The cross sections of those samples were chosen as shown in Figure 4.6. The testing surface was polished starting with 400 emery sand cloth, then polishing with finest emery polishing paper, and finishing with Billiard cloth. These polished samples were placed in a confined glass bottle, then etched with 40% by weight aqueous methylamine solution to remove the PET for 24 hours. The etched samples were washed with distilled water, and finally dried in air at room temperature.

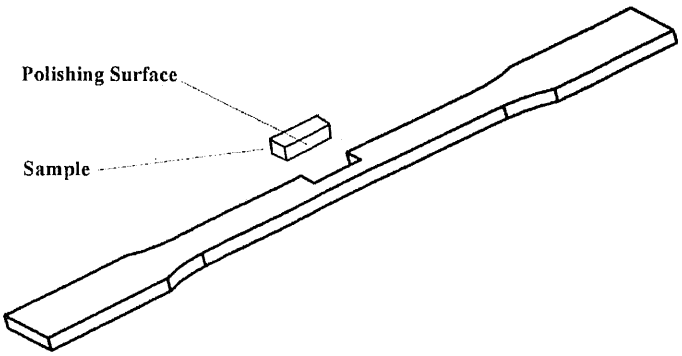

Figure 4.6 Sample used for morphology examination.

4.4.2 Morphological Analysis

The morphological analysis for LCP/PET blends was carried out using three types of instruments: scanning electron microscope (SEM), optical microscope (OM), and matrix videometrix econoscope (MVE).

SEM is a necessary tool for studying the surface morphology of LCP blends because it can show the detailed characteristics of the surface morphology of the blends at different processing conditions. The SEM provides a narrow beam of electrons that can be focused on a sample for the purpose of image formation or elemental analysis. The beam may be moved or scanned across the sample surface, or fixed at one point.

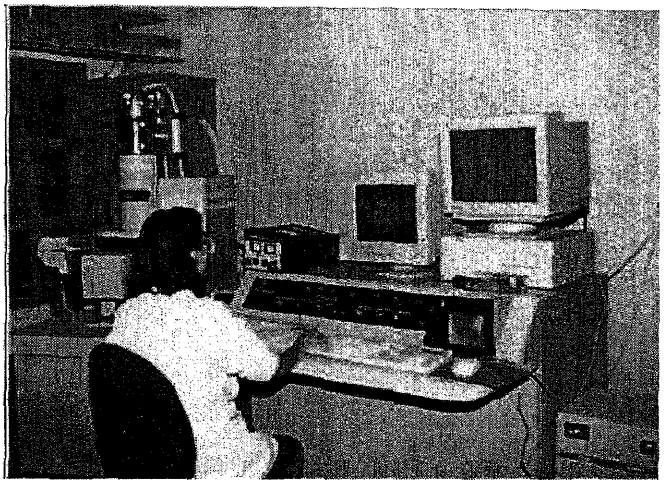

Figure 4.9 Scanning electron microscopy.

For this investigation, SEM examinations were carried out for characterizing the structure of the PET/LCP blends at the Geo-Environmental Engineering Laboratory in NJIT, using a ESEM 2020 as shown in Figure 4.9. The 270 - 450X magnifications were selected due to LCP fiber's or particle's size ranging from 5 to 50 μm. The same magnification was used for all samples in order to compare structure characteristics. An accelerating voltage of 20 KV was used for the photographs. The examinated sample was situated in the position that the electron beam from electron microscope is perpendicular to the viewed surface of the sample. The electron beam is scanned in a gapwise direction across the cross section of the sample, starting from the sample edge to its center with the

270X magnification. Therefore, the gradual change of morphology across the thickness of the sample can be viewed. A more detailed structure of a domain at the surface of samples, 150 ~ 200 μm away from the edge of the samples, was observed using the 450X magnification in order to analyze the size and shape of LCP fibers.

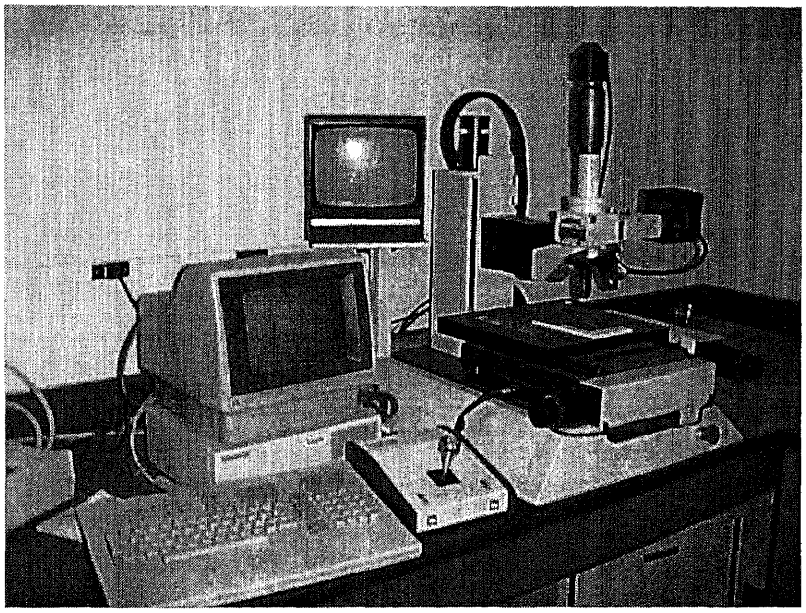

Figure 4.10 Matrix Videometrix Econoscope.

The Matrix Videometrix Econoscope (MVE) was used to measure the thickness of skin layer. The MVE uses a non-contact technique to provide rapid dimensional verification of complete parts or specified features of a part. The MVE comprises a general purpose computer (HP-9000 series), a 3-axis positioning control system, a digital image processor, and a part monitor section, as shown in Figure 4.10. The software used in the computer HP-9000 is divided into six major functions. TOPO function, one of the six major functions, was used in this study. During measurement, magnification lenses,

and the light intensity are specified after the points on the viewed surface to be sampled. It executes the automatic measurement of the main features of the surface. The data representing the surface profile include X, Y, and Z coordinates of the pointed sample. The measurement results are shown on the computer screen. In this study, two points on the viewed surface were sampled: one is on the edge of sample, another is on the interface between skin and core layers. Each value of the thickness of the skin layer is the average of 4 - 6 measurements.

The optical microscope can help us to examine the entire cross section of samples and was used to analyze the variation of the skin layer. The samples, which were used in SEM analysis, were also used in OM analysis.

4.5 Measurement of Tensile Properties

The mechanical tester used in this investigation is the Instron Universal Testing Instrument (Model 1125). The instrument is a highly reliable precision system for evaluating the tensile properties of materials including tensile modulus, tensile stress, and elongation.

In this study, the crosshead speed is set to be 5 mm/min for polymers and the chart speed is set to be 100 mm/min. Gage length is 50 mm. Before starting measurement, A warm-up period of 15 minute minimum is need to assure load cell stability.

The modulus, E (unit: Pa), of PET/LCP blends is calculated as follows:

$$E = \frac{9.8\Delta P}{A}\frac{ML_g}{\Delta l} \tag{4.3}$$

where ΔP is the difference in load which is read from the initial straight line portion of the stress-strain curve, kg; Δl is the difference in the corresponding displacement on the chart, m; M is the magnification ratio, which is equal to the chart speed divided by crosshead speed; A is the cross section area of the mold cavity, 40.3225×10^{-6} m^2; L_g is the gauge length, 0.05 m. The crosshead displacement approximately equals specimen extension, if the gage length equals the initial separation between the grips, and when non-rigid materials are tested, as suggested by the user manual (Instron 1979). In our case, a error may be involved because of the semi-rigid materials, which were measured in this study. The error has not been calculated. The stress at break and the elongation at break are calculated as follows, respectively:

$$S = \frac{9.8 P_{\max}}{A} \tag{4.4}$$

and

$$\varepsilon = \frac{\Delta l_y}{L_o M} \times 100 \tag{4.5}$$

where S is the stress at break, Pa; P_{max} is the maximum load recorded on chart, kg; Δl_y is the displacement at break point on chart, m; L_o is the original length of sample, which is equal to gauge length in this study, m; ε is the elongation at break (%).

CHAPTER 5

NUMERICAL MODELING AND ANALYSIS

This chapter presents and discusses the simulations of the injection process and the flow analysis of the advancing melt front (AMF), in order to understand the effect of process parameters on the morphology development and mechanical properties of PET/LCP blends. Due to the flow complexity in mold cavity, it is necessary to perform numerical simulations corresponding to the injection process of PET/LCP blends. The parameters that govern the injection process are involved in the simulations. A finite element model is presented so that the morphology and mechanical properties of PET/LCP blends can be quantitatively studied. A series of computational simulations is performed to predict the modulus of PET/LCP blends at various injection conditions. The simulated predictions are then compared with measurements which are reported in the next two chapters.

5.1 General Description

In injection molding the molten polymer is forced to flow into an empty cold cavity of desired shape and is allowed to solidify under high holding pressure. At the beginning of the injection cycle, the molten polymer, which has been maintained at a uniform temperature inside the barrel of the injection molding machine, is forced to flow through the nozzle into the sprue under variable flow rate or pressure depending on the control scheme of the injection unit. The runner system delivers the melt from the sprue to the entrances (gates) of the part cavity. At the end of the filling stage, the injection machine switches over to constant holding-pressure control which initiates the post-filling stage of the cycle. During post-filling stage, injection speed is very low (about 0.1 ~ 0.5% of normal injection speeds) and the flow of the polymer melt in mold cavity could be ignored. The structure development of LCP blends during injection molding mainly

occurs during the filling stage because the deformation of LCP domains is induced by the melt flow in the mold cavity as discussed in Chapter 2. Therefore, our numerical analysis is focused on the filling stage.

The important feature of the mold-filling process is the existence of an advancing melt front (AMF). As many investigators (Tadmor 1974; Beery, 1991) pointed out or suggested, the AMF is a major source of deformation and orientation of fluid elements. Therefore, it is necessary to analyze the flow field in the AMF region. The flow field is determined by the shear flow behind the AMF, the frozen layer, and the geometry of the mold cavity. The melt flow in mold cavity is very complex and CMOLD (Version 98.7), a commercial software for the simulation of injection molding, was used to analysis the flow. CMOLD did not provide a analysis and simulations for the melt flow in the AMF region. Therefore, the melt flows in the AMF region and behind the AMF were analyzed separately. First, we simulated the injection molding or the shear flow behind the AMF using CMOLD, and calculated velocity in mold cavity; the outputs from CMOLD simulations were the velocity profiles behind the AMF at various processing conditions. The velocity profile and the distribution of elongational strain in the AMF region were then calculated with a new method developed in this study. Finally, the deformations of the LCP domains in the matrix were determined by introducing a new model to describe the relationship between the elongational strain and the aspect ratio of the LCP fibers.

5.2 Simulation of Injection Molding

5.2.1 Governing Equations

The finite element method for the simulation of the injection molding fully utilizes the advantages of computer capacity in performing speedy and reliable calculations for a wide range of engineering problems. This is particularly true when the problem is difficult to solve by using a traditional mathematical model or when the geometry and

flow are too complex. In this study, a finite element package, CMOLD, is utilized for simulation and prediction of the melt flow in mold cavity.

A CMOLD analysis includes three phases: design, analysis applications, and postprocessing. In the design phase, the solid model of the part to be injection molded and its finite element mesh are created. Material properties and processing parameters needed to perform the analysis are specified in this phase. The simulations of injection molding are performed in the phase of analysis applications, which provides access to different injection stages including: filling, cooling, postfilling, and shrinkage and warpage. Since the deformation and orientation of the LCP phase occur during the filling stage, simulations were performed for the filling phase in this study. The postprocessing phase of CMOLD program follows the design and analysis application phases. The analysis results are shown in a graphical display and/or tabular form.

Momentum and energy equations governing the behavior of all common fluid motion are very complicated. With today's computer hardware and material testing technology it is not feasible to solve them in complicated domains such as injection mold cavities. To make solution times and material data requirements more reasonable, a number of assumptions are made.

A schematic diagram of flow in a mold cavity and a coordinate system are shown in Figure 5.1. The gravitational and inertial forces compared with viscous forces are very small and can be ignored. Since most injection molded parts are thin walled, the Y component of velocity (across the gapwise of part cavity) can be neglected while considering the flow in mold cavity. But the Y component of velocity is very important in considering the melt flow in the AMF region. In the energy equation, the terms to be neglected include total rate of energy change due to compression/expansion of the melt, convective heat transfer in the Y direction, and conduction heat transfer in the X and Z directions. Using the above assumptions, the governing equations are reduced to the following:

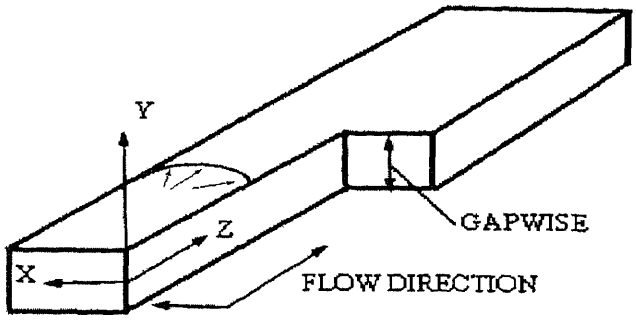

Figure 5.1 Schematic diagram of flow in mold cavity and the coordinate system

Continuity equation

$$\frac{\partial V_x}{\partial x}+\frac{\partial V_y}{\partial y}+\frac{\partial V_z}{\partial z}=0 \tag{5.1}$$

Momentum equations

$$\frac{\partial p}{\partial x}=\frac{\partial}{\partial y}(\eta\frac{\partial V_x}{\partial y}) \tag{5.2}$$

$$\frac{\partial p}{\partial z}=\frac{\partial}{\partial y}(\eta\frac{\partial V_z}{\partial y})$$

$$\frac{\partial p}{\partial y}=0$$

Energy equation

$$\rho c_p(\frac{\partial T}{\partial t}+V_x\frac{\partial T}{\partial x}+V_z\frac{\partial T}{\partial z})=\eta\dot{\gamma}^2+k\frac{\partial^2 T}{\partial y^2} \tag{5.3}$$

where p is the pressure; V_X and V_Z are the velocities in the X and Z directions, respectively; η is the shear viscosity of the melt; ρ is the density of the melt; c_p is the specific heat of melt; $\dot{\gamma}$ is the shear rate; T is the temperature of the melt; k is the heat conductivity of the melt. CMOLD solves Eqs. 5.1 - 5. 3 and gives out velocity and pressure profiles in the mold cavity.

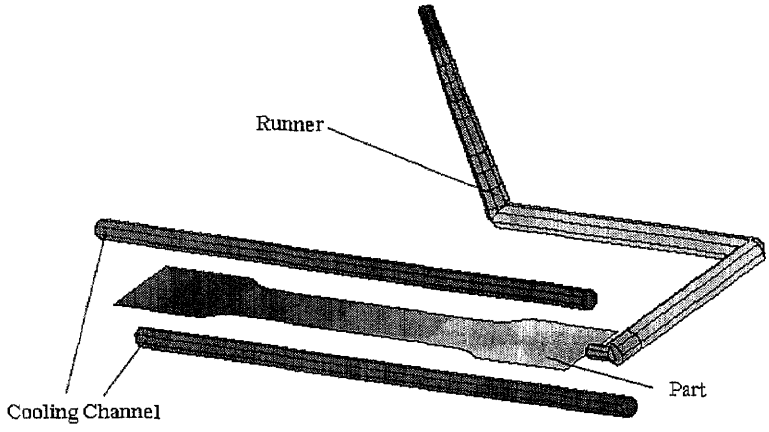

Figure 5.2 A solid model for simulations including a part, cooling channels and a runner.

5.2.2 Solid and Finite Element Mesh Models

Figure 5.2 shows a solid model including three portions: part (the dogbone, an ASTM standard tensile test specimen), melt-delivery systems (the runner), and cooling channels. Since most injection molded parts are thin compared with their global dimensions, they can be approximated by their mid-planes or surfaces. The thickness of the part is used to incorporate the actual geometry features. The solid model part was first created using PRO/ENGINEER (Version 20), a commercial CAD/CAM software, then a mid-plane was created based on the solid model. This mid-plane was meshed in PRO/ENGINEER with triangular shell elements with 6 nodes and then exported to CMOLD for the simulation of injection molded part. An example of the meshed model is shown in Figure 5.3. The runner was meshed with one-dimensional elements using CMOLD as shown in Figure 5.3.

The cooling channels are important for controlling the heat transfer in injection molding. In this study, two cooling channels arranged on both sides of the part (Figure 5.2) were used. In CMOLD, the cooling channels were meshed with one-dimensional elements. The final mesh geometry of the cooling channels is shown in Figure 5.3.

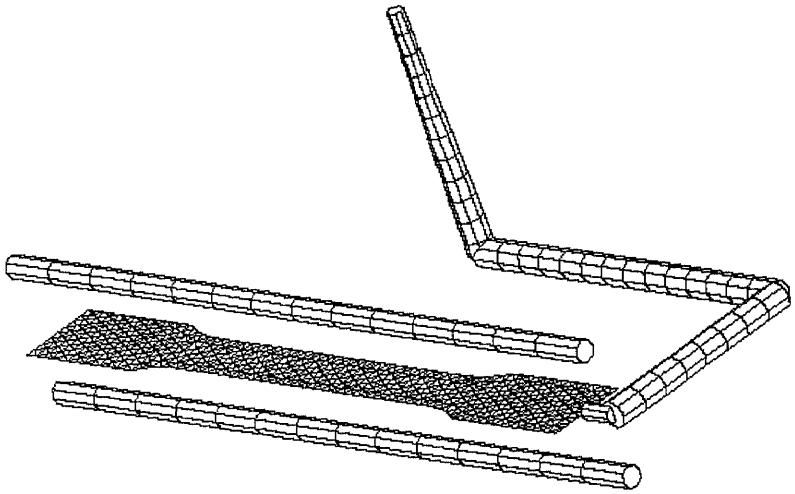

Figure 5.3 A mesh model including triangular shell elements for the part and one-dimensional elements for both cooling channels and runner.

5.2.3 Material Properties

Analysis of the filling stage requires data on the physical properties of the plastic material, mold material, and coolant.

A viscosity function is required for the simulation of the filling stage. According to the user's manual (CMOLD, 1997), the Cross-exponential model was used in this study for simulation of the filling stage in injection molding because the model treats polymer viscosity as a function of temperature, shear rate, and pressure. It handles both the Newtonian and the shear-thinning flow regimes found in polymer rheology and is expressed as follows:

$$\eta(T,\dot{\gamma},p) = \frac{\eta_0(T,p)}{1+(\frac{\eta_0\dot{\gamma}}{\tau^*})^{1-n}} \tag{5.4}$$

with

$$\eta_0(T,p) = B\exp(\frac{T_b}{T})\exp(\beta p)$$

where T is the temperature; $\dot{\gamma}$ is the shear rate; p is the pressure; η_0 is the zero-shear viscosity. n, τ^*, T_b, β, and B are 5 constants of this model; n is the power law index; τ^* characterizes the shear stress level of the transition region between the Newtonian and power-law asymptotic limits; T_b characterizes the temperature sensitivity of η_0; β characterizes the pressure dependence of η_0. For PET/LCP blends with different LCP concentrations, the 5 constants, which are regressed from rheological measurements by CMOLD, have different values and are listed in Table 5.1.

Table 5.1 Main properties of PET/LCP blends

Properties	LCP Concentration (wt %)		
	5%	15%	25%
N	0.7954	0.7451	0.4226
τ^* (Pa)	57.19	685.6	18060
β	0	0	0
B (Pa.s)	$6.178\text{X}10^{-11}$	$4.753\text{X}10^{-12}$	$2.223\ \text{X}10^{-15}$
T_b (°C)	15886	17217	20731
Density (Kg/m^3)*	$1.209\ \text{X}10^3$	$1.226\ \text{X}10^3$	$1.244\ \text{X}10^3$
Specific Heat (J/Kg-K)*	$1.468\ \text{X}10^3$	$1.692\ \text{X}10^3$	$1.916\ \text{X}10^3$
Thermal Conductivity (W/m-K)*	0.1445	0.1522	0.1611
Volume Fraction of LCP*	0.0432	0.1314	0.2222

*Data are calculated using Eqs 5.5 - 5.8.

According to the suggestion in the user's manual (CMOLD 1997), the density, specific heat, and thermal conductivity of the PET/LCP blends with different LCP

contents (LCP is assumed to be the fillers) can be calculated using the following equations:

Density

$$\rho = V_f \rho_f + (1 - V_f)\rho_m \tag{5.5}$$

Thermal conductivity

$$\frac{1}{K} = \frac{1 - V_f}{K_m} + \frac{V_f}{K_f} \tag{5.6}$$

Specific heat

$$C_p = \phi_{wf} C_{pf} + (1 - \phi_{wf}) C_{pm} \tag{5.7}$$

where ρ_f and ρ_m are the densities of filler and matrix, respectively; K_f and K_m are the thermal conductivities of filler and matrix, respectively; C_{pf} and C_{pm} are the specific heats of filler and matrix, respectively; ϕ_{wf} is the weight fraction of filler; V_f is the volume fraction of filler, which can be determined from ϕ_{wf} as follows:

$$V_f = \frac{\phi_{wf}(\frac{\rho_m}{\rho_f})}{1 - \phi_{wf}(1 - \frac{\rho_m}{\rho_f})} \tag{5.8}$$

The density, specific heat, and thermal conductivity of PET/LCP blends with different LCP contents calculated using above equations are listed in Table 5.1. These properties of the components of the blends used in the calculations are listed in Table 4.1. The mold material is P-21 and its main properties are listed in Table 5.2. The coolant used in this study is pure water, the properties of which are also listed in Table 5.2

Table 5.2 Main properties of mold material and coolant from CMOLD database

Properties	Mold Material	Pure Water (20 °C)
Density (Kg/m^3)	7820	998
Specific heat (J/Kg-K)	460	4180
Thermal conductivity (W/m-K)	36.5	0.643
Viscosity (Pa.s)	N/A	1.0×10^{-3}

Table 5.3 Input data about processing parameters for simulations

Max. machine clamp force (N)	8.62745×10^{5}		
Max. machine injection volume (m^3)	15×10^{-5}		
Max. machine injection pressure (Pa)	1.99×10^{8}		
Max. machine injection rate (m^3/s)	1.7042×10^{-8}		
Fill time (s)	1.5		
F/P switch over by % volume	99%		
Absolute ram speed profile	Stroke	Stroke %	Inject. Speed
	0.625	0	0
	0.5	20	20
	0.5	21	10, 12, 14, 16
	0.05	99	10, 12, 14, 16
	0	100	1
Ambient temperature (°K)	298		
Inlet melt temperature (°K)	553, 560, 583, 593		
Coolant manifold control	Temperature, °K		Flow rate,
1	291,307, 323, 330		1.67×10^{-4}
2	291,307, 323, 330		1.67×10^{-4}

5.2.4 Processing Parameters

Processing parameters studied in the simulations are the injection speed, melt temperature, and mold temperature. As discussed in Chapter 4, the injection molding machine is capable of injecting the melt at three different injection speeds in one injection shot. In the CMOLD analysis, an absolute ram-speed profile is needed to simulate the three control stages. The two parameters specified in the absolute ram-speed profile are the percentage of ram stroke and the percentage of the maximum machine injection rate. According to the settings for screw axial position in the experiment discussed in Chapter 4, the stroke is from 0.625 to 0 inches. Percentage of stroke and injection speeds corresponding to the stroke are listed in Table 5.3.

The effect of melt temperature is simulated by changing the inlet melt temperature in the CMOLD input file as listed in Table 5.3. Coolant temperature needed in the CMOLD analysis was used to simulate the effect of mold temperature and is listed in Table 5.3. All other variables required in the CMOLD analysis are also listed in Table 5.3.

5.2.5 Results and Discussion

The main objective of the above simulations is to figure out the velocity profiles behind the AMF at various processing conditions. The velocity profiles are then used as the boundary conditions at the entrance of the AMF region. Tadmor (1974) suggested that a fully developed shear flow exists behind the AMF, which can be used as the boundary conditions at the entrance of the AMF region. Obviously, the average velocity of a fully developed shear flow does not vary with filling time. In this study, we used the velocity profiles at the location where average velocity is constant as the boundary conditions at the entrance of the AMF. Using CMOLD, it is easy to determine the location from the relationship between the average velocity and filling time. Figure 5.4 shows the average velocity as a function of filling time, which was obtained from the simulations of

injection molding. As we can see, the average velocity is constant after 0.49 s filling time. With the data in Figure 5.4, we can calculate the velocity profile of the fully developed shear flow, as well as the frozen layer, corresponding to this filling time.

Figures 5.5 and A1 - A5 (Figures A1 - A5 are shown in Appendix A) show the velocity profiles of fully developed shear flows behind the AMF at different injection speeds, melt temperatures, and mold temperatures for PET/LCP (85/15 wt %) blends. Due to the symmetry of the mold cavity, only the velocities of half cavity thickness are shown. The normalized thickness is the Y coordinate across thickness divided by half thickness of mold cavity. As seen, the velocity at center increases more than that away from center as the injection speeds increase and tends to zero at the interface between the melt and frozen layers.

The effect of melt temperature on the velocity profile is shown in Figure 5.6; the velocity increases as melt temperature increases. At the center of mold cavity, there is significant increase of velocity compared with area away from the center. The influence of mold temperature on velocity is shown in Figure 5.7. The variation of velocity with mold temperature is seen near the regions between center and cavity wall. Frozen layers also vary with injection speed, melt temperature, and mold temperature as shown in Figures 5.8 - 5.9. The effect of these parameters on thickness of frozen layer is very distinct. As seen, the thickness of frozen layer changes from 0.101 to 0.118 mm, which is about 6 % to 7.5 % of half thickness of mold cavity; at large injection speed, high mold temperature, and high melt temperature, thin frozen layers are obtained.

5.3 Flow Analysis of Advancing Melt Front (AMF) Region

5.3.1 Description of Problem

Both deformation and orientation of LCP phase originate from the fountain flow in the AMF region. In this section, analysis of fountain flow in the AMF region is presented.

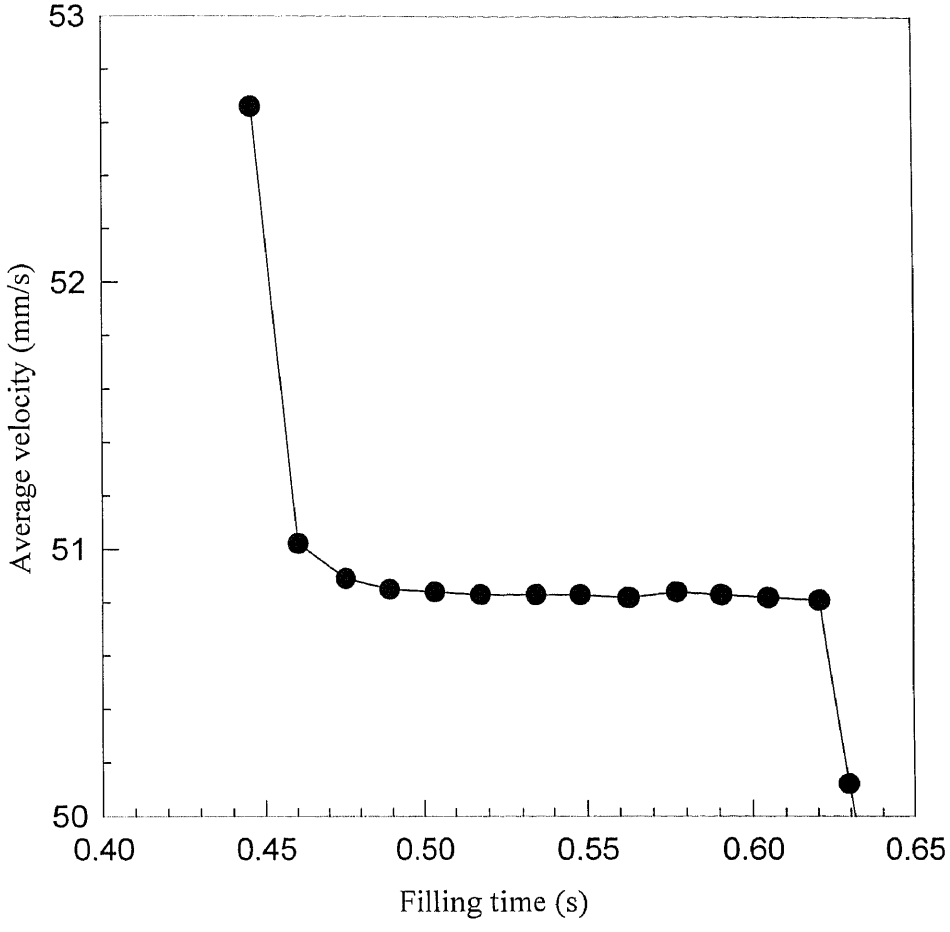

Figure 5.4 Average velocity as a function of filling time.

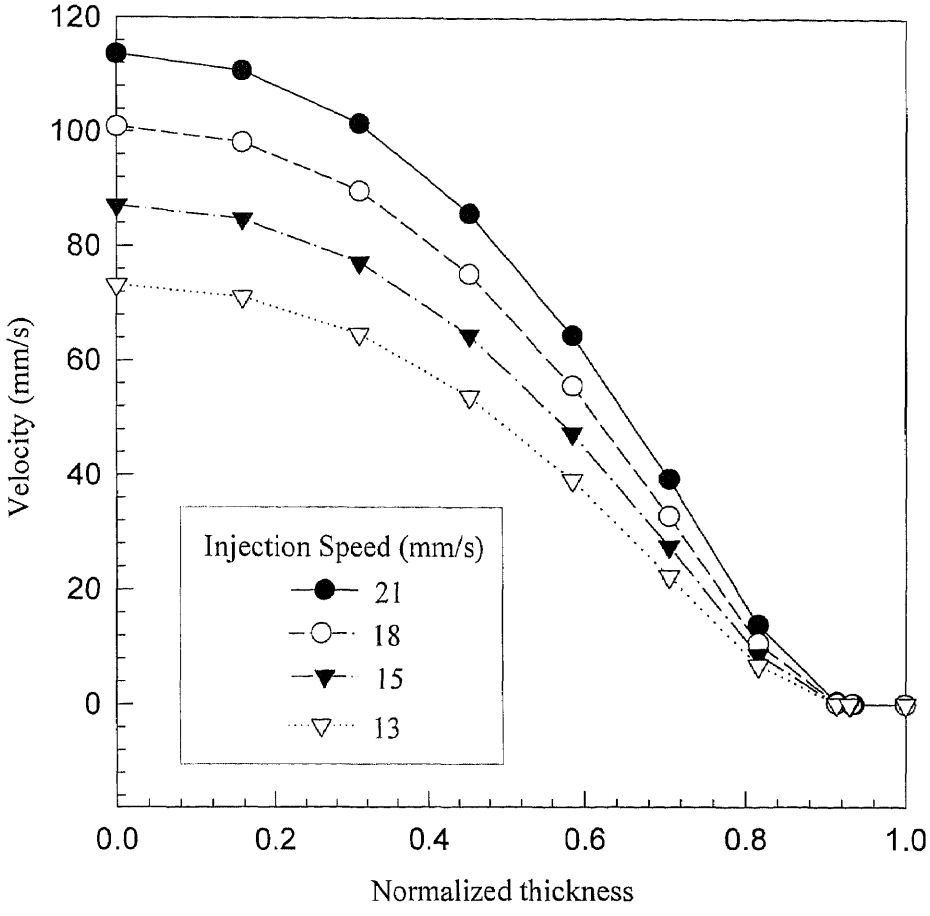

Figure 5.5 Velocity profiles behind the AMF at a melt temperature of 320 °C and a mold temperature of 18 °C for PET/LCP (85/15 wt %) blend. 0.0 is the center of mold cavity and 1.0 is the mold wall.

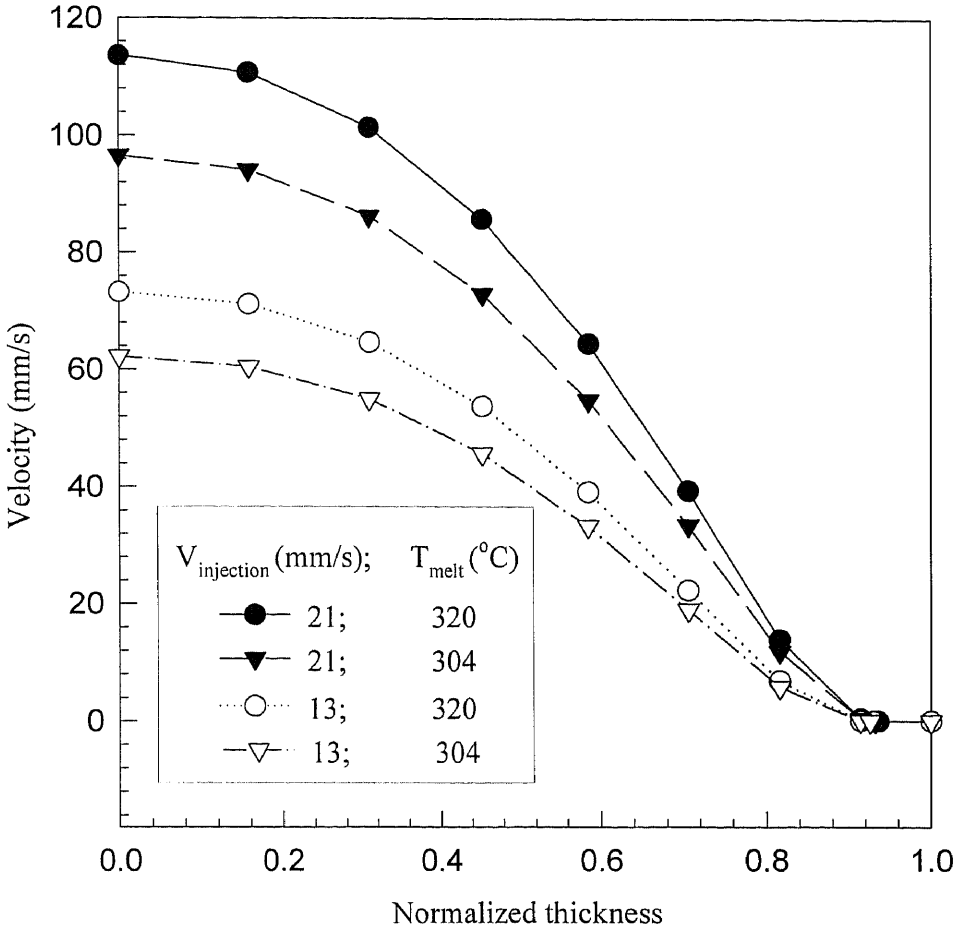

Figure 5.6 Effect of melt temperature on velocity profile at mold temperature of 18 °C for PET/LCP (85/15 wt %) blend.

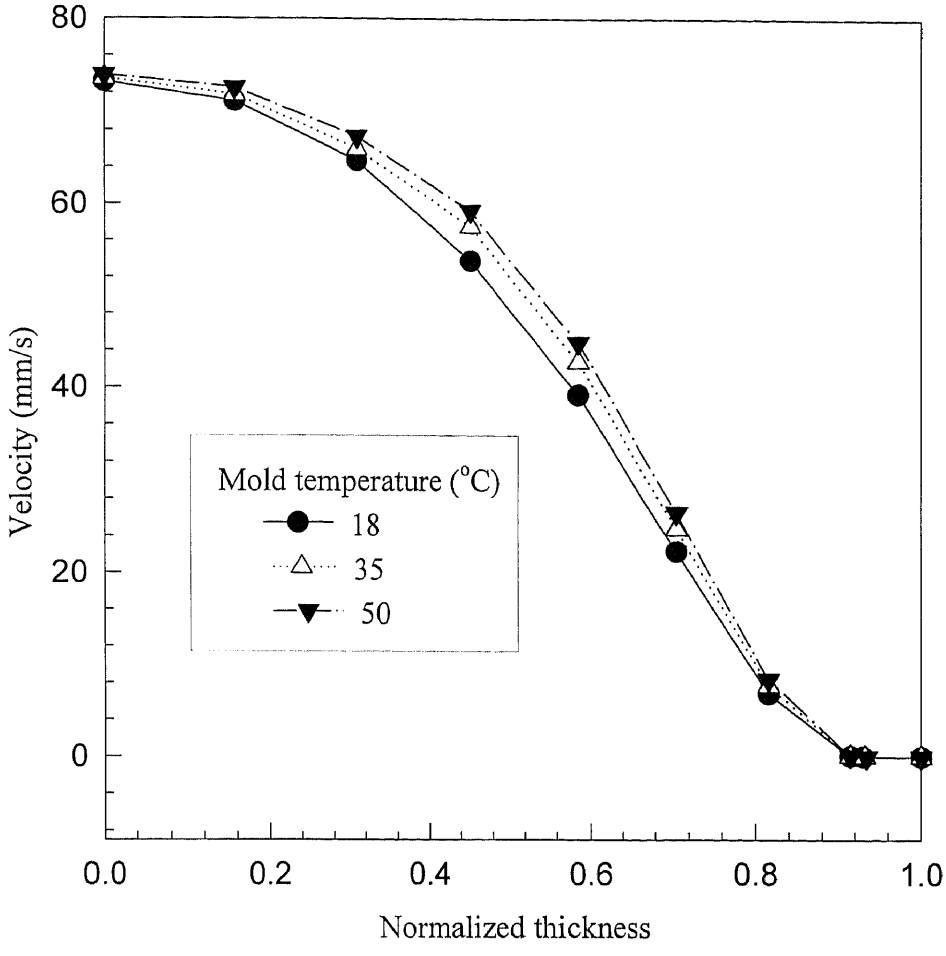

Figure 5.7 Effect of mold temperature on velocity at melt temperature of 320 °C and injection speed of 13 mm/s for PET/LCP (85/15 wt %) blend.

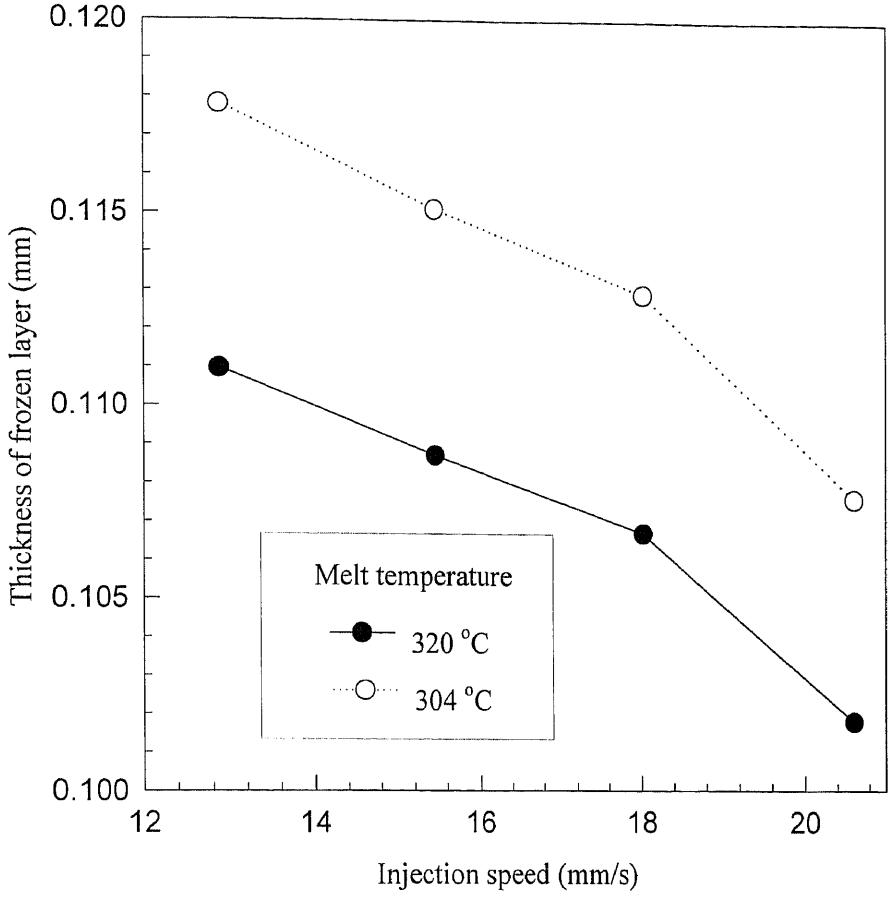

Figure 5.8 Effect of injection speed and melt temperature on the thickness of the frozen layer at a mold temperature of 18 °C for PET/LCP (85/15 wt %) blend.

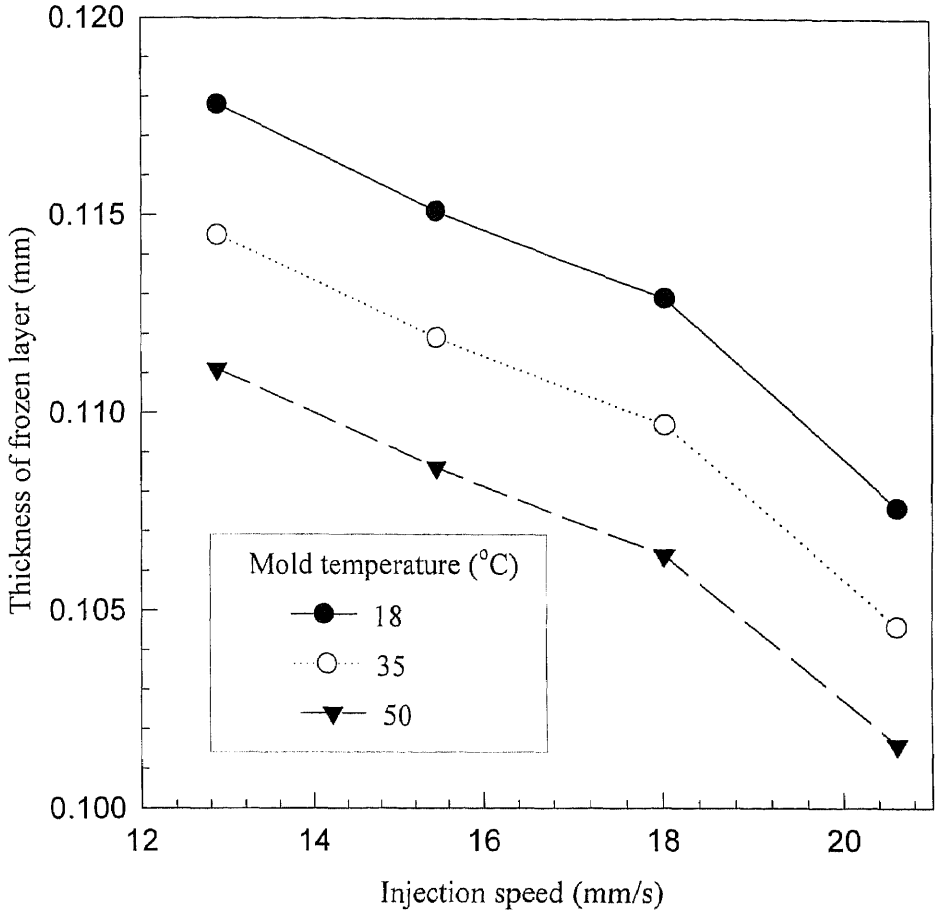

Figure 5.9 Effect of mold temperature on the thickness of the frozen layer at a melt temperature of 304 °C for PET/LCP (85/15 wt %) blend.

The thickness of most injection molded parts is usually very thin compared to other dimensions of the parts. The effect of two sides (A and B in Figure 5.10) of the injection molded part on the flow field in AMF region could be ignored. The flow field in the AMF region can be approximated by a planar flow between two parallel walls. The governing equations need only to be solved under half this domain because of symmetry. Injection molding filling involves unsteady flow of polymer melts and solidification of the melt on the cold wall. It appears that the fountain flow in the AFM region is influenced, but is not determined, by the unsteady or by the nonisothermal characteristics of the flow field (Mavridis et al. 1986, Behrens et al. 1987, Lee 1997). Accordingly, we decided to avoid the complications of unsteady and non-isothermal motion and assumed the fountain flow to be steady and the free surface of the AMF region to advance in the flow channel at a constant speed. The coordinate system is fixed on the AMF and moves with it (see Figure 5.11).

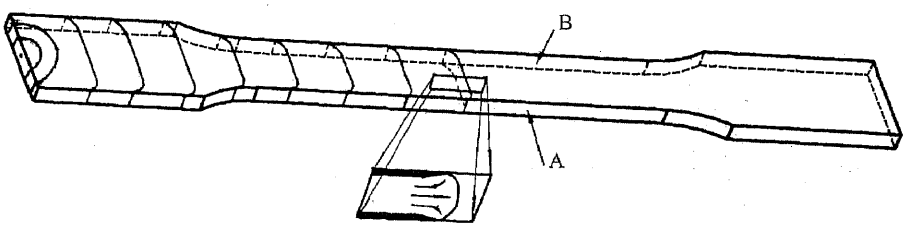

Figure 5.10 Schematic diagram of the flow field in mold cavity with microscopic view inserted for the AMF region.

Another factor which could influence the fountain flow is the curved shape of the free surface of the AMF (curved line BC in Figure 5.11). Tadmor (1974) used a semicircular shape to approximate the curved shape. The study of Mavridis (1986) shows that the shape of the free surface is surprisingly close to a semicircular for both Newtonian and power-law fluids as suggested by Tadmor (1974). Behrens (1987) and Lee (1997) also pointed out that a steady free surface shape can be obtained when the

movement of the AMF remains constant while the free surface shape changes toward a nearly semicircular. According to the treatment of Behrens (1987), when the geometry of mold cavity and injection speed are kept unchanged, a steady movement of the AMF could be obtained. Therefore, a semicircular shape has been used to approximate the free surface shape of the AMF in this analysis.

The frozen layer is considered in this analysis because its magnitude is crucial for the deformation and orientation of the LCP domains. The frozen layer varies with melt temperature, injection speed, and mold temperature as shown in Figures 5.8 and 5.9. The variations of the frozen layer with these variables were obtained from the simulations discussed in the preceding section.

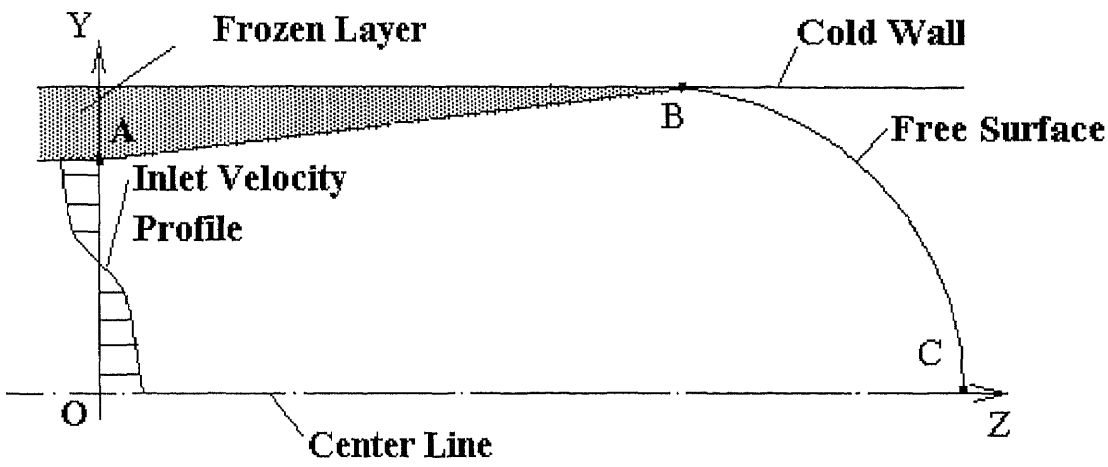

Figure 5.11 Schematic diagram of the fountain flow pattern in the AMF.

Based on the above discussions, the flow domain of the AMF region was defined as shown in Figure 5.11. The left boundary of the flow field includes a line OA and a frozen layer. The frozen layer at the point A decreases linearly to zero at the intersection of the cold wall and the free surface, the point B, and a straight line (AB) is formed as the top boundary of the field. The right boundary is the free surface with the half semicircular

of shape. The symmetry line or center line of mold cavity is used as the bottom boundary of the field.

5.3.2 Velocity Profile in AMF Region

The flow problems in the AMF were dealt with by Tadmor (1974), Dietz et al (1978), and H. Mavridis et al (1986). Tadmor suggested a model of planar elongational flow to describe the flow in the AMF region. The velocity profile is approximately given by:

$$V_y = \bar{k}\ y \tag{5.9}$$

$$V_z = -\bar{k}\ z \tag{5.10}$$

where $\bar{k}$ is the elongational strain rate, and

$$\bar{k} = \frac{V_{\max} - \bar{V}}{L} \tag{5.11}$$

$\bar{V}$ is the average velocity of the free surface along the Z direction, V_{max} is the maximum velocity of the fully developed shear flow behind the AMF, and L is the distance between the free surface of the AMF and the fully developed shear flow. In this model, Tadmor applied the elongational rate (Eq. 5.11) on the centerline of the AMF region to the whole melt front. In the present analysis, the model was applied to individual element and the elongational rate was defined for the element.

The AMF was partitioned into a collection of elements by lines parallel to OC (see Figure 5.11). The area near the cold wall has a higher concentration of the elements in order to capture the flow in detail in this region. The flow field after partitioning is shown in Figure 5.12a.

According to the mass continuity, for *i*th element (see Figure 5.12b), we have:

$$Q_{in}^{i} - Q_{out}^{i} = 0 \tag{5.12}$$

where Q_{in}^{i} and Q_{out}^{i} are the flow rates at which fluids in the element flow into and out of the element, respectively. For an element, fluids flow into the element through the left and lower sides of this element, and flow out of the element through the right and upper sides of this element. The flow rates are given, respectively, by the following expressions:

$$Q_{in}^{i} = \frac{VI_z^i + VI_z^{i-1}}{2} \times YI_i + \int_0^{Z_{i-1}} V_y^{i-1} dz \tag{5.13}$$

$$Q_{out}^{i} = \frac{VO_z^i + VO_z^{i-1}}{2} \times YI_i + \frac{VO_y^i + VO_y^{i-1}}{2} \times (Z_{i-1} - Z_i) + \int_0^{Z_i} V_y^i dz \tag{5.14}$$

where *VI* and *VO* are the velocities at the entrance and on the free surface, respectively; V_y^i and V_y^{i-1} are the velocities of the Y direction distributed along the top and bottom boundaries of the *i*th element; all other symbols in Eqs. 13 and 14 are as referenced in Figure 5.12b.

V_y^i and V_y^{i-1}, and V_z^i and V_z^{i-1}, based on Tadmor's model (Eqs. 5.9 and 5.10), are derived as follows:

$$V_y^i = \frac{VO_y^i - VI_y^i}{Z_i} Z \tag{5.15a}$$

$$V_y^{i-1} = \frac{VO_y^{i-1} - VI_y^{i-1}}{Z_{i-1}} Z \tag{5.15b}$$

$$V_z^i = \frac{VO_z^i - VI_z^i}{Z_i} Z \tag{5.16a}$$

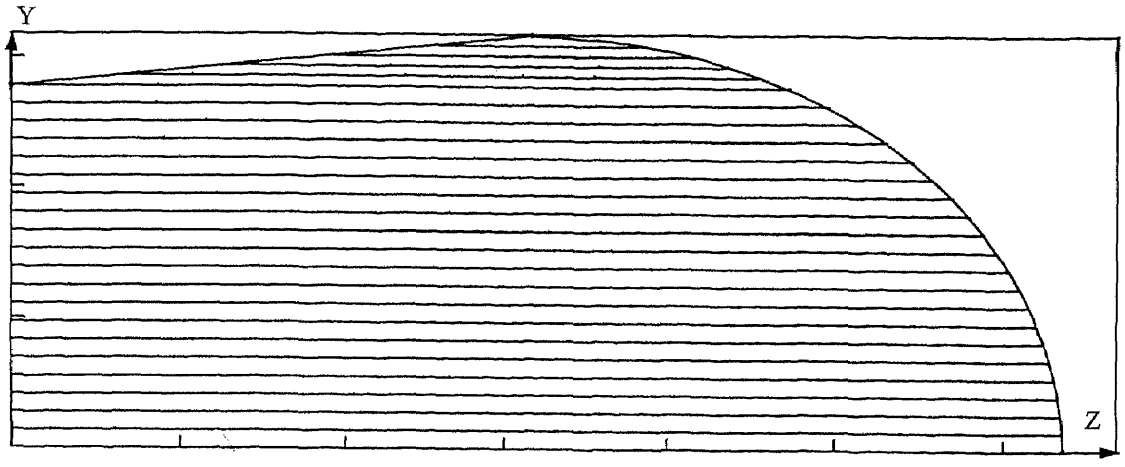

(a)

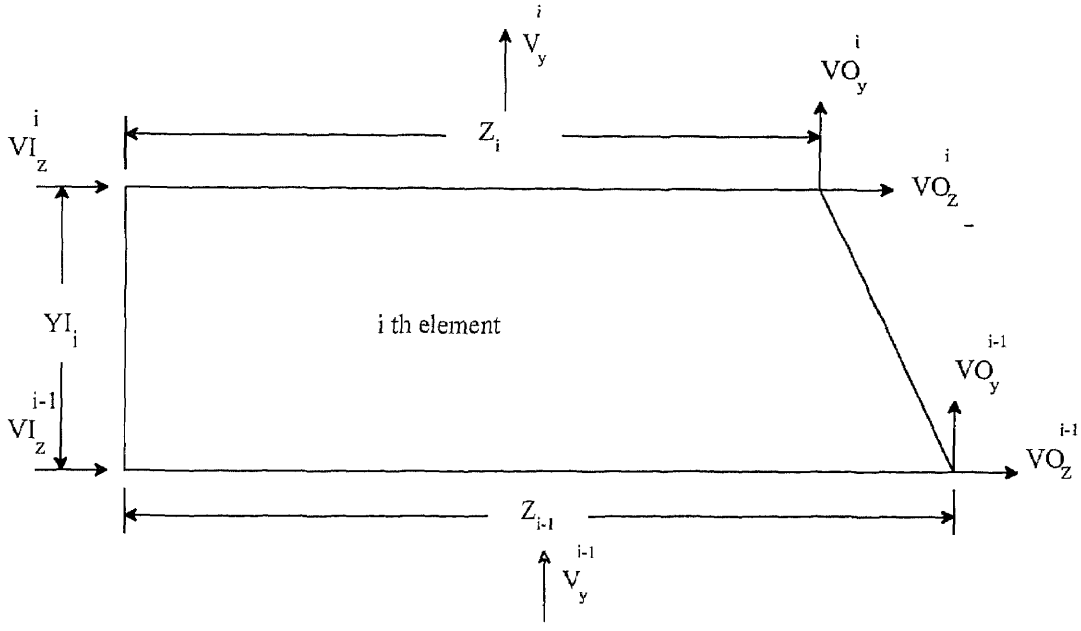

(b)

Figure 5.12 Typical meshed domain and an individual element.

$$V_z^{i-1} = \frac{VO_z^{i-1} - VI_z^{i-1}}{Z_{i-1}} Z \tag{5.16b}$$

All symbols in above two equations are as referenced in Figure 5.12b. Substituting Eqs. 5.13 - 4.16 into Eq. 12, we have:

$$VO_z^i + VO_z^{i-1} + \frac{Z_{i-1}}{YI_i} VO_y^i + \frac{Z_{i-1} - 2Z_i}{YI_i} VO_y^{i-1} = VI_z^i + VI_z^{i-1} + \frac{Z_i}{YI^i} VI_y^i - \frac{Z_{i-1}}{YI^i} VI_y^{i-1} \tag{5.17}$$

In order to solve Eq. 5.17, the variables in this equation must be defined at the boundary of the AMF region. As shown in Figure 5.11, at center line (line OC in Figure 5.11) there is a slip-free boundary condition which has a symmetric character and the transverse velocity component (the Y direction) is zero; at the entrance, there is no flow along vertical direction (the Y direction) and VI_y should be zero; at the wall of the mold cavity and the interface between melt and solidified layer (line AB in Figure 5.11) a no-slip boundary condition is applied and the velocity components, both normal and tangential to the wall and the interface, vanish. Hence, we have

$$\text{OC}, \quad V_y^i = 0 \tag{5.18}$$

and

$$\text{AB}, \quad V_z^i = 0, \quad V_y^i = 0. \tag{5.19}$$

The inlet velocity profile at entrance of the AMF region (the line AO in Figure 5.11) is derived from the simulations of injection process using CMOLD as shown in Figures 5.5a - 5.5f. Considering that the fountain flow is simply a hydromechanical phenomenon, the following boundary condition at the free surface can be incorporated under moving coordinate system:

$$\tilde{V} \cdot \tilde{n} = 0 \tag{5.20a}$$

where $\tilde{V}$ is the velocity vector on the free surface and $\tilde{n}$ is the normal vector on the free surface. They are expressed as follows, respectively:

$$\tilde{V} = (VO_z^i - \bar{V})\tilde{j} + VO_y^i \tilde{k} \tag{5.20b}$$

$$\tilde{n} = \cos\theta_i \, \tilde{j} + \sin\theta_i \, \tilde{k} \tag{5.20c}$$

where θ_i is the angle between the Z coordinate axis and the normal vector; $\tilde{j}$ and $\tilde{k}$ are the unit vectors along the Z and Y coordinate axes, respectively; $\bar{V}$ is the average velocity of the free surface along the Z direction. Rewriting Eq. 5.20a by substituting Eq. 5.20b and 5.20c

$$VO_z^i = \bar{V} - VO_y^i \tan\theta_i \tag{5.20d}$$

Combining Eq. 5.17 with Eqs. 5.18 - 5.20, we have

$$VO_y^i = \frac{1}{A}(B \times VO_y^{i-1} + VI_z^i + VI_z^{i-1} - 2\bar{V}) \tag{5.21a}$$

with velocity in first element (i = 1, and $VO_y^{i-1} = 0$)

$$VO_y^1 = \frac{1}{A}(VI_z^1 + VI_z^0 - 2\bar{V}) \tag{5.21b}$$

where

$$A = \frac{Z_{i-1}}{YI_i} - \tan\theta_i \tag{5.21c}$$

$$B = \tan\theta_{i-1} - \frac{Z_{i-1} - 2Z_i}{YI_i} \tag{5.21d}$$

After we have the velocity on the melt front, based on the above equations, the velocity profile in the whole AMF region can be obtained from Eqs. 5.15a and b - 5.16a and b. Algorithms were written to perform these calculations, and are shown in Appendix C.

The average velocity $\bar{}$ is derived as follows. Considering the mass continuity, the flow rate at the line OA is equal to the flow rate at the line BC (see Figure 5.11), then we have

$$\frac{2}{3}(\frac{H}{2}-\delta)V_{\max}=\frac{1}{2}\bar{V}H \tag{5.22a}$$

or

$$\bar{V}=\frac{2}{3}\frac{H-2\delta}{H}V_{\max} \tag{5.22b}$$

where H is the thickness of the mold cavity; δ is the thickness of the frozen layer.

Figures 5.13a and 5.13b are the distributions of velocity vectors at a fixed and a moving frame of references, respectively. Figure 5.14 shows the comparison between the velocity profile on the free surface of the AMF obtained from ANSYS (Version 5.4), a commercial software, and from Eqs 5.21a - 5.21d. As seen, the computational results of Eq. 5.21 are in line with the ANSYS calculations for the AMF region. It is shown that the simple method developed in the above analysis can be used to analyze the fountain flow in the AMF region. The disagreement between the two results occurs near the point B (see Figure 5.11). This is because of a singularity of velocity field near the point B.

5.3.3 Deformation of Fluid Element

Now consider a material point *P* which at time t = 0 is at the position (y_{po}, z_{po}). The coordinates (y, z) refer to the moving frame of reference. The trajectory of the material point in the moving frame of reference can be mathematically described by the initial value problem:

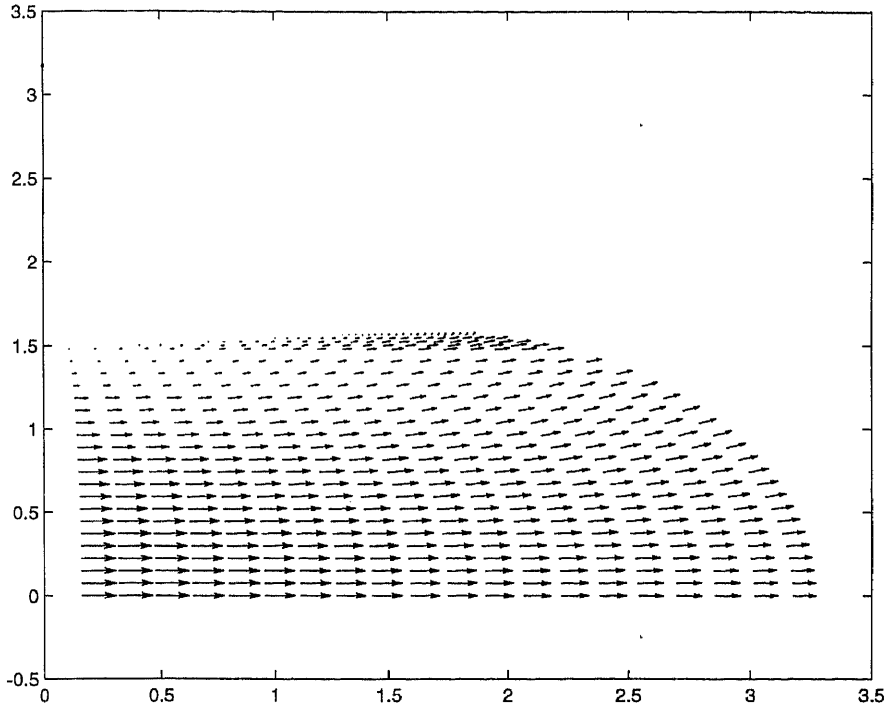

Figure 5.13a Velocity vector at a fixed frame of reference.

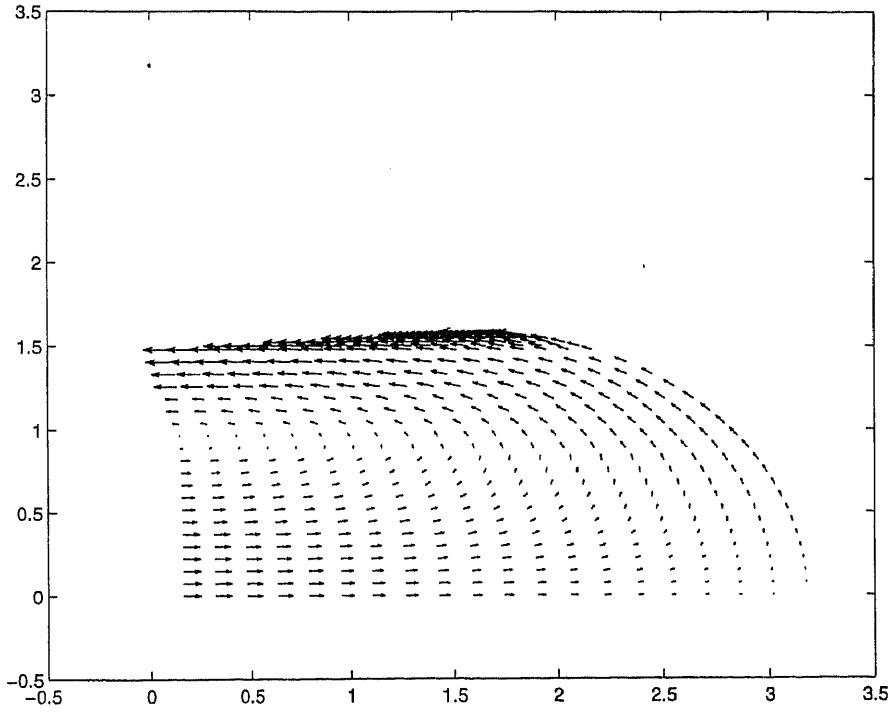

Figure 5.13b Velocity vector at a moving frame of reference.

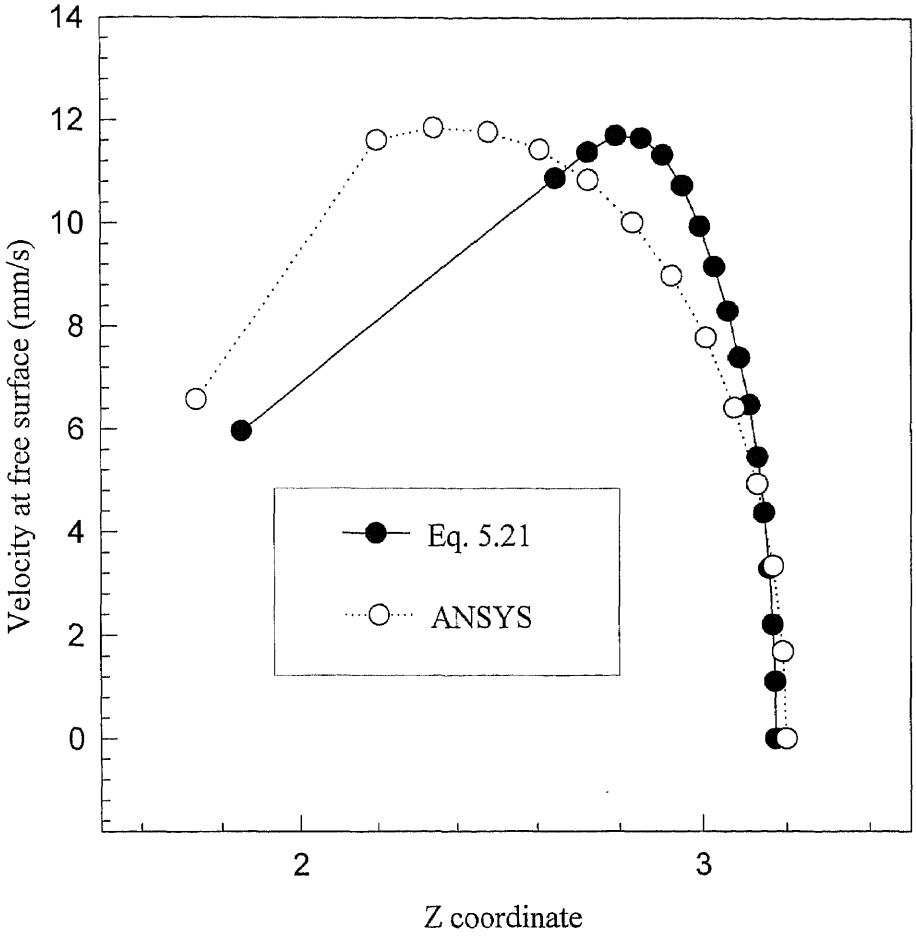

Figure 5.14 Comparison of the computational method developed in this study with ANSYS.

$$\frac{d}{dt}\begin{bmatrix} y_p \\ z_p \end{bmatrix} = \begin{bmatrix} V_{yp} \\ V_{zp} \end{bmatrix} \tag{5.23a}$$

$$\begin{bmatrix} y_p \\ z_p \end{bmatrix} = \begin{bmatrix} y_{p0} \\ z_{p0} \end{bmatrix} \quad \text{at } t = 0 \tag{5.23b}$$

where V_{yp} and V_{zp} are the velocity components along the Y and Z directions in the moving frame of reference, which are calculated using the simple method we derived above. The complete deformation history can be obtained by applying Eqs. 5.23a and 5.23b for all the points in the whole AMF region. Figure 5.15 is the deformation history of two fluid elements which get distorted and stretched while moving toward the walls in full agreement with Tadmor's sketch (1974) for a moving frame of reference. This figure also shows the characteristic splitting patterns of a fluid element along the centerline as it approaches the tip of the melt front. The deformation of the fluid element away from the center line is smaller than that of the fluid element near the center line. The latter experiences longer distance or a longer deformation time in the AMF region than the former. This is a direct consequence of the fountain flow behind the AMF. Mass continuity results in a vertical component of velocity that causes splitting of the flow field.

Before the relationship between morphology and mechanical properties can be accurately predicted, we must determine the distribution of elongational strain. With Eqs. 5.23, the final length and final coordinates of each fluid element can be determined. So the elongational strain that the element experiences can be calculated using equation:

$$\varepsilon = \frac{L - L_o}{L_o} \tag{5.24}$$

where L and L_O are the final and original lengths of a fluid element, respectively.

Figures 5.16 and A6 - A10 (Figures A6 - A10 are shown in Appendix A) show the distributions of the elongational strains across the thickness of the mold cavity at different processing conditions. As seen, the elongational strains decrease with increasing injection speed. But for all the cases considered, at the locations from 0.9 mm to 1.0 mm away from the center of the mold cavity, there is almost no influence of injection speed on the elongational strains.

Figures 5.17 and 5.18 give the effect of melt and mold temperatures on the elongational strains. At low mold and melt temperatures, large elongational strain was obtained. But the influence of mold temperature is more pronounced than that of melt temperature.

5.4 Calculation of Modulus of PET/LCP Blends

5.4.1 The Composite Model

The flow analysis in the AMF region and the deformation calculations discussed in the above sections have shown that particles of the dispersed phase in a matrix are elongated while flowing through the AMF region, and form a layered structure: fiber-like dispersed phase is formed near the wall of mold cavity and non-deformed particles occur in the core region. Experimental studies presented in Chapter 6 have confirmed the theoretical prediction. From the experimental and theoretical results, we can conclude that the final structure of PET/LCP blends is identical to that of short fiber reinforced composites. The differences in morphology between the two composites are the distribution of the fiber aspect ratio and orientation of fibers. The aspect ratio of fibers of PET/LCP blends varies

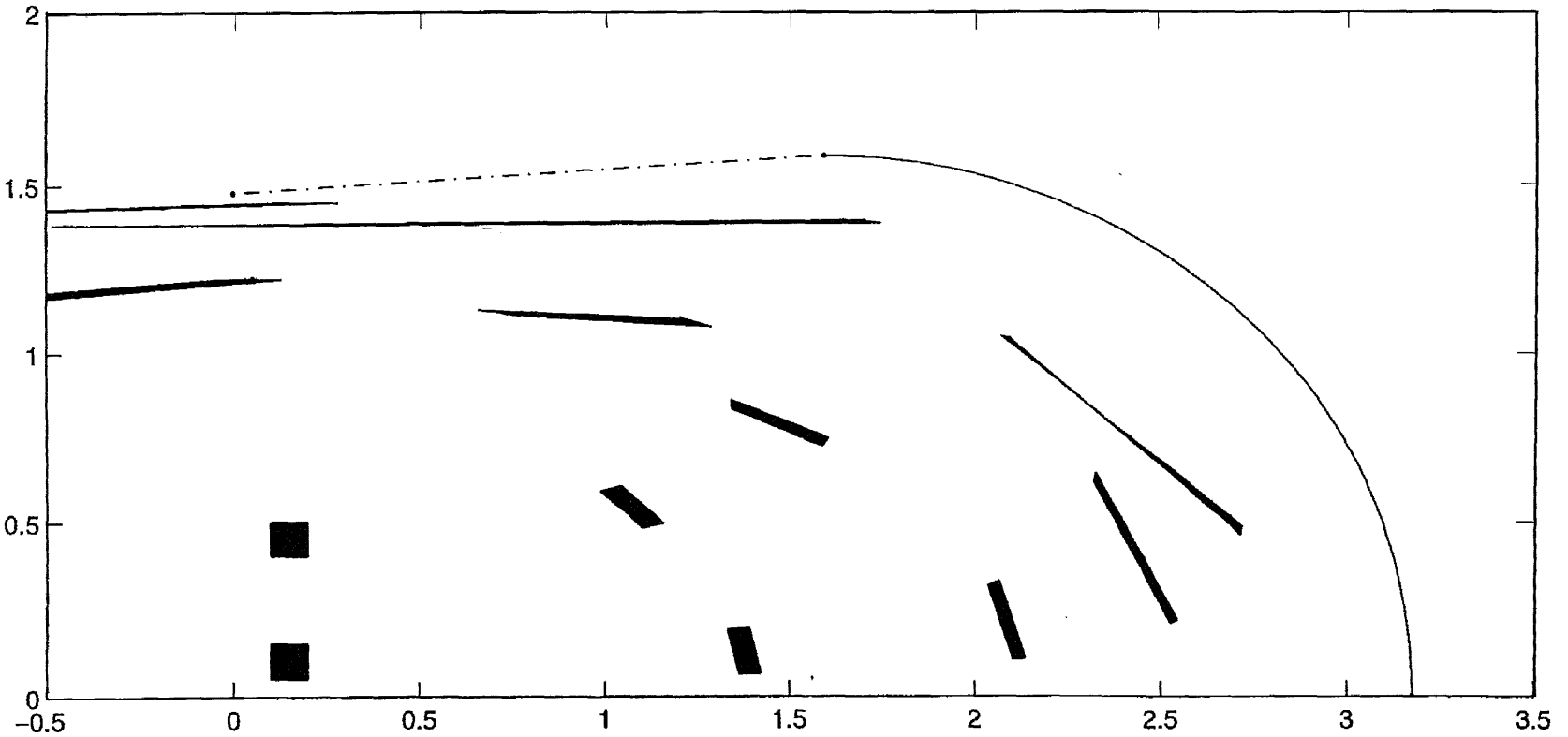

Figure 5.15 Deformation history of two fluid elements in the AMF region.

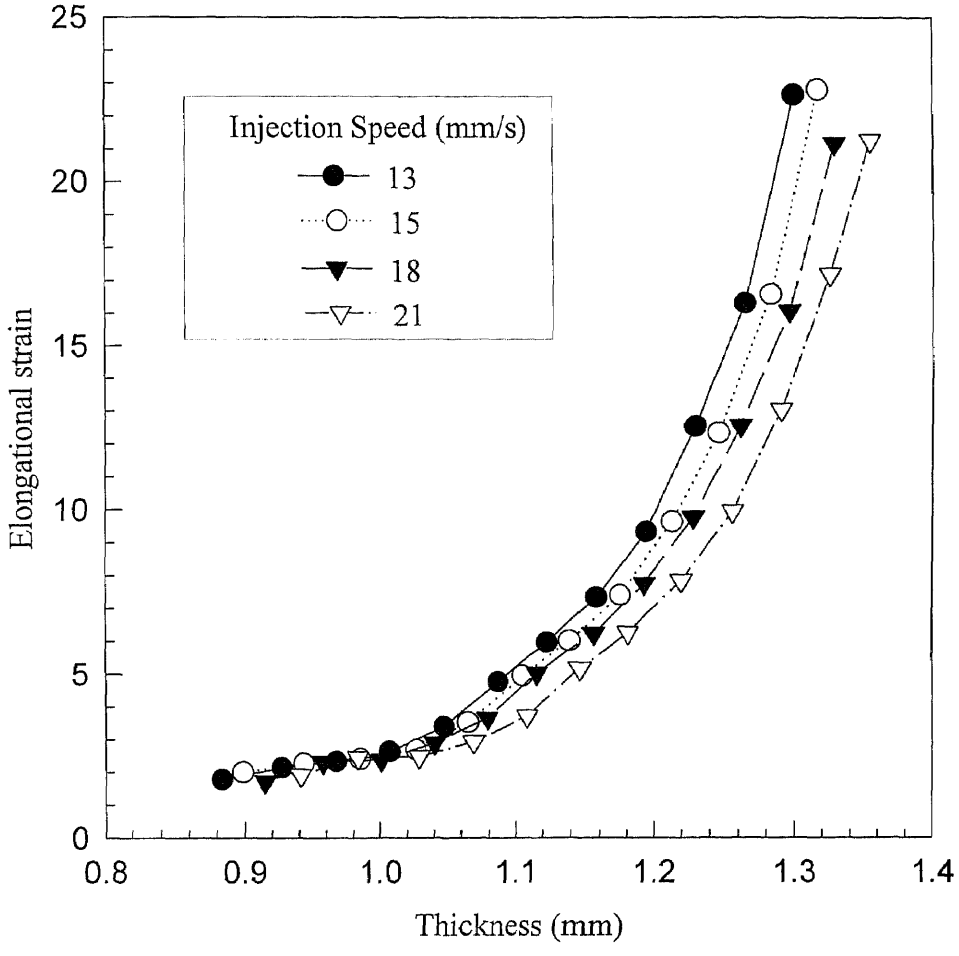

Figure 5.16 Elongational strain distribution across the thickness of mold cavity at a melt temperature of 320 °C and a mold temperature of 18 °C for PET/LCP (85/15 wt %) blend.

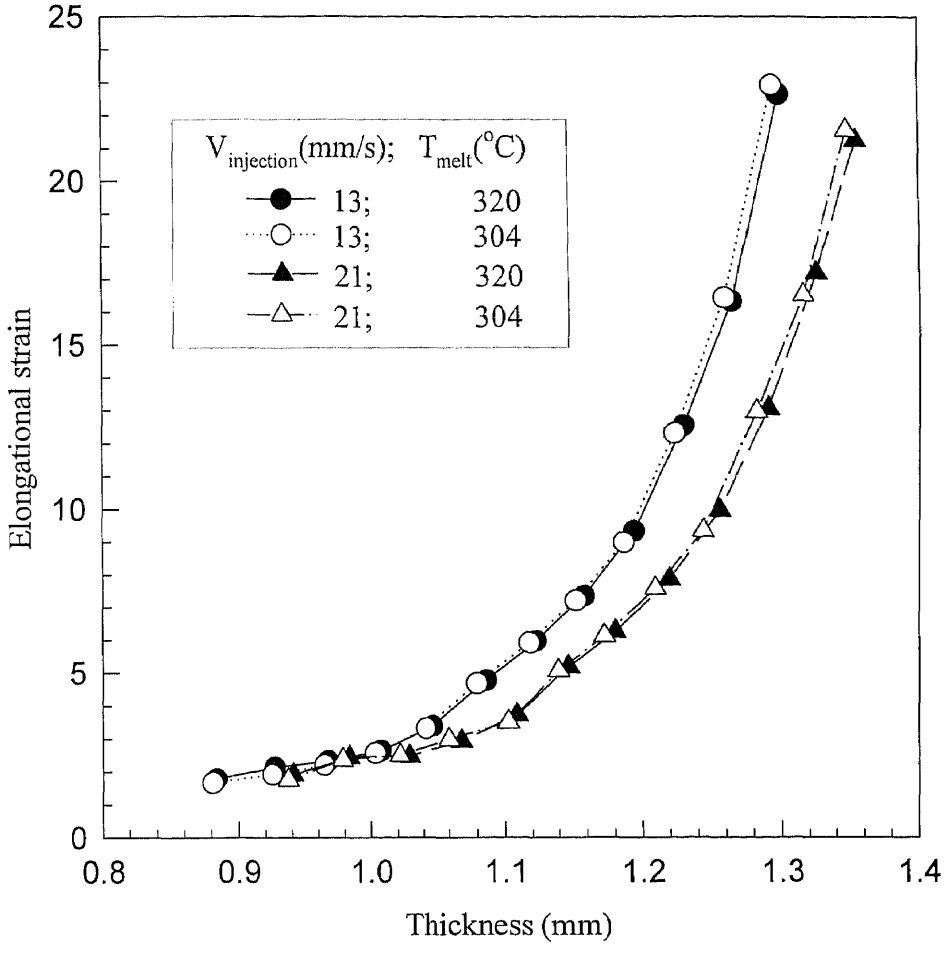

Figure 5.17 Effect of melt temperature on elongational strain at a mold temperature of 18 °C for PET/LCP (85/15 wt %) blend.

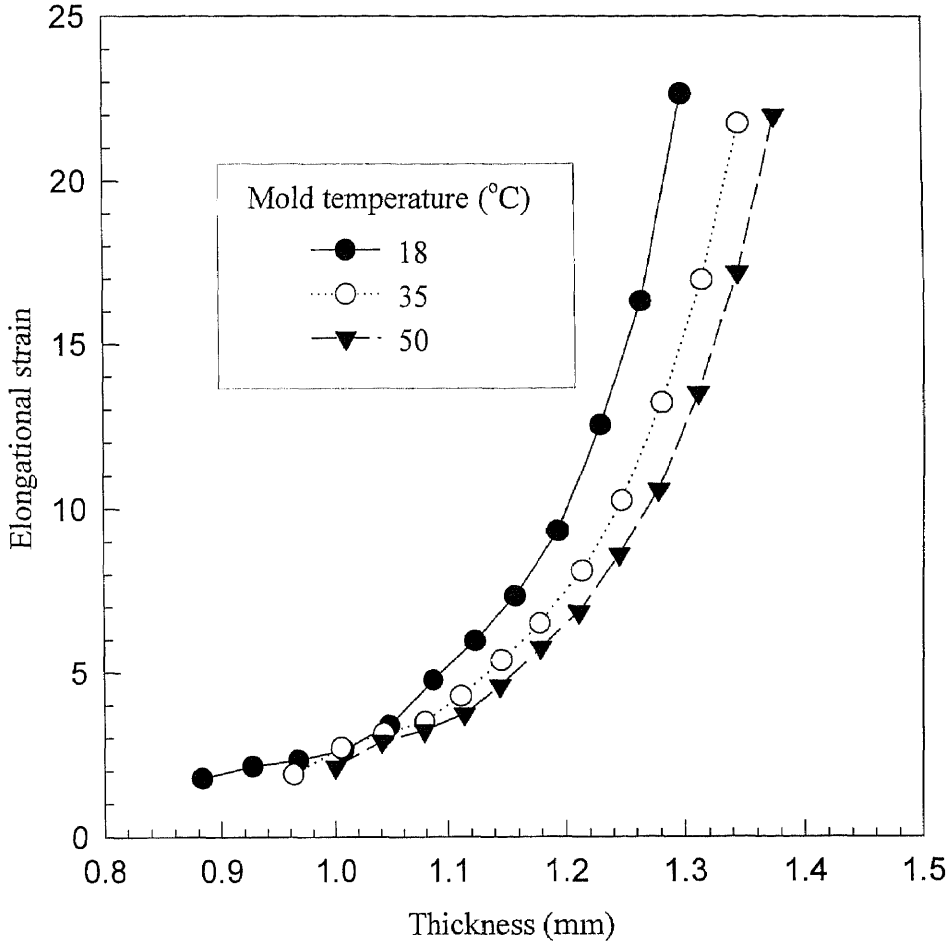

Figure 5.18 Effect of mold temperature on elongational strain at a melt temperature of 304 °C and an injection speed of 13 mm/s for PET/LCP (85/15 wt %) blend.

from large near the skin to small in the core. Hence the traditional composite model can be used to predict the mechanical properties of the PET/LCP blends. In this study, the Halpin-Tsai composite model (Halpin 1969, Tsai 1968) is applied to predict the modulus of PET/LCP blends with the assumptions of (1) perfectly oriented fibers and (2) good interfacial adhesion. The first assumption is reasonable since our results presented in Chapter 6 show that the LCP fibers are almost parallel to each other and to the flow direction (perfect orientation). The second assumption can only be validated with a fracture test which we have not yet performed. But Li et al (1992) reported that there is a good adhesion between the LCP and PET at room temperature. The model is given as follows:

$$\frac{E}{E_m} = \frac{1 - ABV_f}{1 - BV_f} \tag{5.25}$$

with

$$B = \frac{E_f / E_m - 1}{E_f / E_m + A} \qquad \text{and} \qquad A = 2\frac{L}{D}$$

where E, E_f and E_m are the moduli of the composite, the reinforcing phase, and the matrix, respectively; L and D are fiber length and diameter, respectively; V_f is the volume fraction of dispersed phase. But, for the PET/LCP blends, the aspect ratio L/D is a function of the processing parameters. As stated earlier, unlike the modulus of the fibers in conventional fiber reinforced composites, the modulus of the LCP fibers in the blends is not constant but varies with the aspect ratio. In next two sections, the relationship between the aspect ratio of the LCP fibers and elongational strain, and that between the modulus of the LCP fibers and the aspect ratio are established.

5.4.2 Relationship between Aspect Ratio and Elongational Strain

It is essential to obtain the relationship between the size of LCP fibers and the elongational strain in the AMF region, in order to predict the distribution of LCP fibers in the mold cavity. The following assumptions were made in our analysis: that the fluid particle is potentially forming a fiber under elongational flow conditions, and that the LCP domain before deformation is a sphere. Furthermore, we have assumed that the elongation and contraction of the LCP domain maintains a uniform deformation as reported by several authors (Song et al. 1993, Lee et al. 1993). Finally, assuming that there is no change of volume before and after deformation of the LCP domain, then equating the volume of a sphere to that of a cylinder, we have:

$$\frac{\pi D_o^3}{6} = L(\frac{\pi D^2}{4}) \qquad (5.26a).$$

where D_O and D are the diameters of the LCP domains before and after deformation, respectively; L is the length of the fiber. Substituting Eq. 5.24 in Eq. 5.26a with $D_O = L_O$, for a sphere, we have:

$$\frac{L}{D} = \sqrt{\frac{3}{2}}(\varepsilon + 1)^{\frac{3}{2}} \qquad (5.26b)$$

where L/D is the aspect ratio of the LCP domain after deformation. Upon substituting the results shown in Figures 5.16 into Eq. 5.26b, we obtained the distribution of aspect ratio of the LCP fibers across the thickness of the mold cavity at different processing conditions. Here, we assume that the original aspect ratio of the LCP fibers is unity. From the results presented in Chapter 6, the aspect ratio of non-deformed LCP domains in the core region is almost one. Figures 5.19a - 5.19c show the variation of the aspect ratio

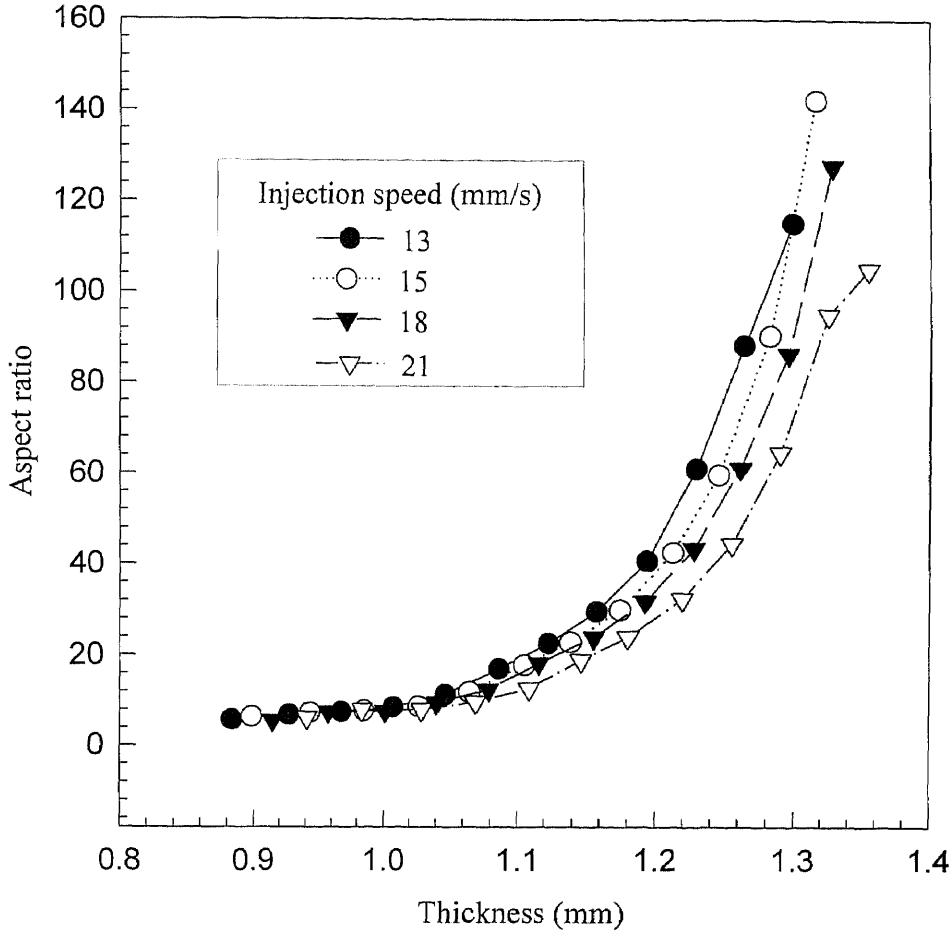

Figure 5.19a Aspect ratio distribution across sample thickness at a melt temperature of 320 °C and a mold temperature of 18 °C for PET/LCP (85/15 wt %) blend.

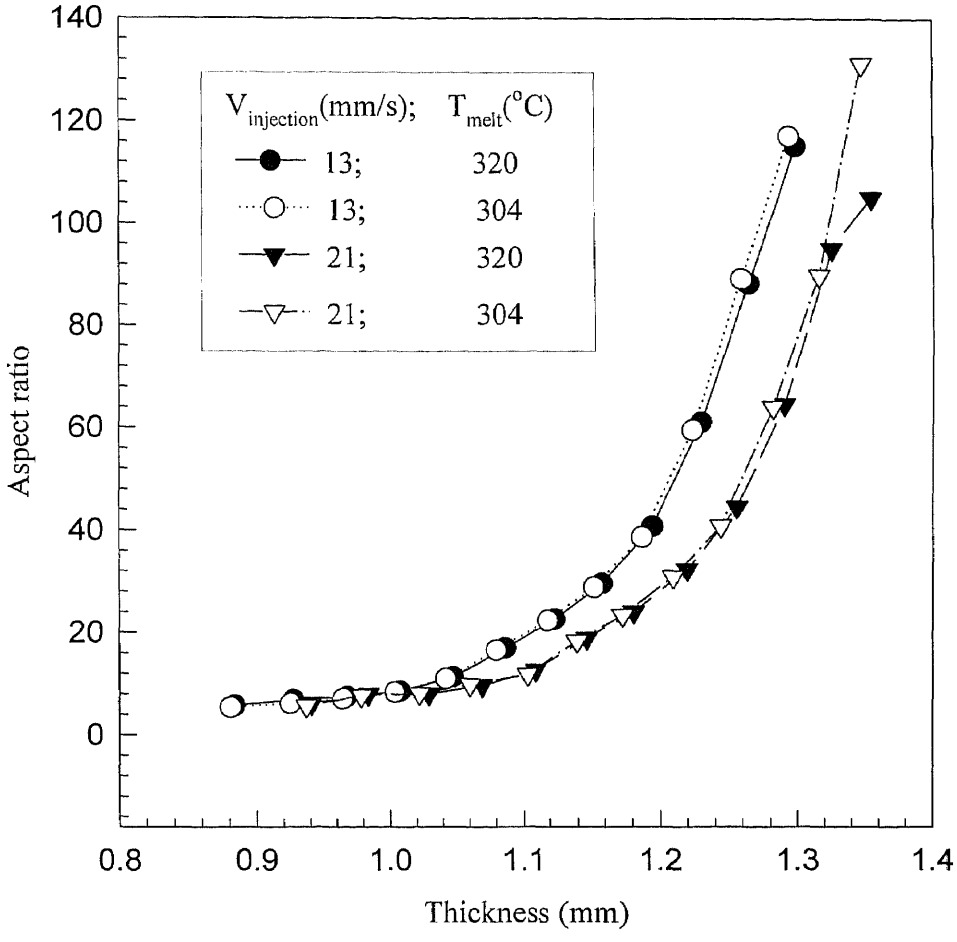

Figure 5.19b Effect of melt temperature on aspect ratio at a mold temperature of 18 °C for PET/LCP (85/15 wt %) blend.

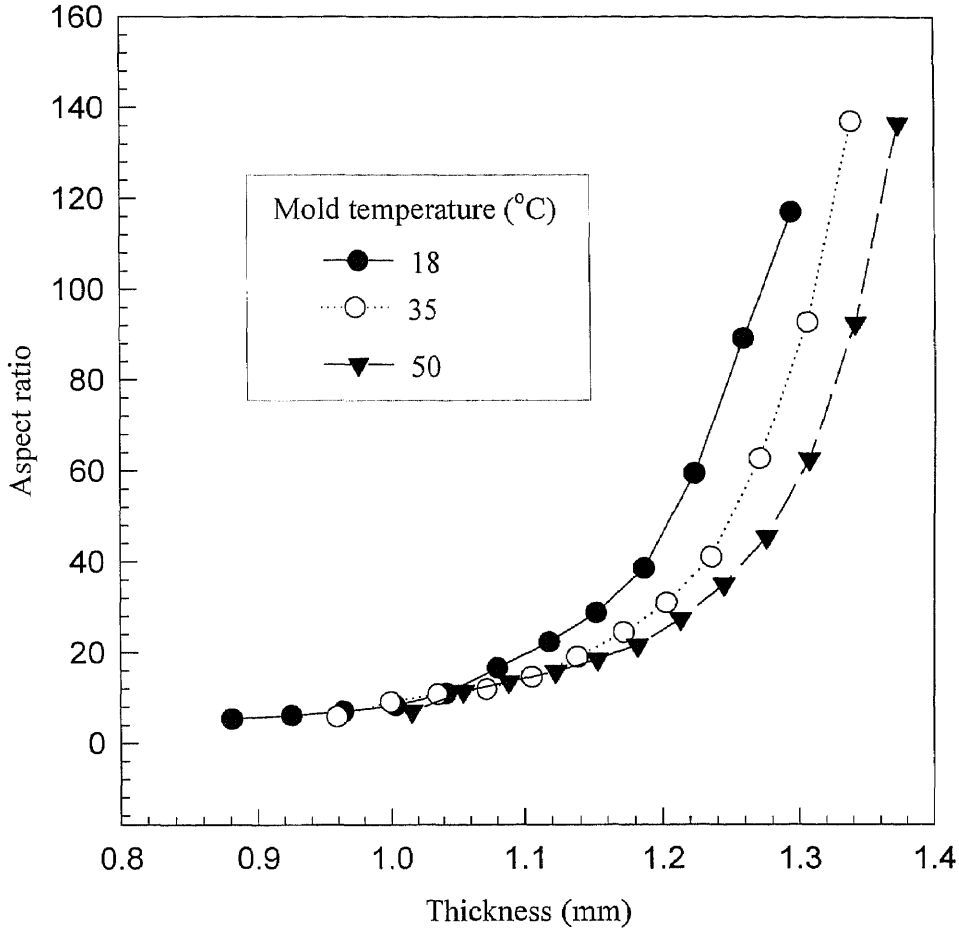

Figure 5.19c Effect of mold temperature on aspect ratio at a melt temperature of 304 °C and an injection speed of 12 mm/s for PET/LCP (85/15 wt%) blend.

with injection speed, mold and melt temperatures: the effects of injection speed and mold temperature are more distinct than that of melt temperature.

5.4.3 Relationship between Aspect Ratio and Modulus of LCP Fiber

Several researchers (Yi et al. 1996, Zachariades et al. 1979) have reported that the modulus of LCP fibers is a function of fiber aspect ratio, and increases monotonically with fiber length, and more rapidly as fiber diameter decreases. Yi et al. (1996) gave an approximate linear function to describe the relationship between the modulus and aspect ratio of Vectra A950 fiber in the form:

$$E_f = 17.4 + 0.33\frac{L}{D} \tag{5.27}$$

With this function, the modulus of the LCP has a minimum of 17.73 GPa when the aspect ratio is unity. But some experimental studies have reported that the modulus could be as low as 9.7 GPa (Acierno and Nobile 1993). The large difference between the two values could be explained by the fact that a linear relationship between the modulus and aspect ratio can not accurately describe the variation of the modulus through all range of the aspect ratio. It is possible that when the aspect ratio decreases to unity, the modulus decreases abruptly to 9.7 GPa. Eq. 5.27 also shows that there is no limiting value for the Vectra A950 if the aspect ratio of the LCP fibers increases infinitely. Obviously, this is not reasonable. Several researchers (Zachariades et al. 1979, Carfagna et al. 1991, Nobile et al. 1989) have pointed out that most LCP moduli approached a limited value at high aspect ratio up to 150. In this study, we use a logarithmic polynomial to describe the

relationship between the modulus of LCP and its fiber aspect ratio, as suggested by Zachariades et al. (1979). This relationship is given as:

$$\log\frac{1}{E_f} = C_1 + C_2\log(X) + C_3\log(X)^2 \tag{5.28}$$

where $X = (L/D)^{-2}$ and C_1, C_2, and C_3 are constants. In the present study, Yi's data (see Table 2.1) and a value of 9.7 GPa as a minimum modulus of Vectra A950 are used to fit Eq. 5.28. A least square analysis yields the following numerical equation for Eq. 5.28:

$$\log(\frac{1}{E_f}) = -2.2722 + 0.1834\log(X) + 0.0045\log(X)^2 \tag{5.29}$$

Figure 5.20 shows the modulus of the Vectra A950 as a function of aspect ratio. We can see that the modulus increases sharply at low aspect ratio and increases slowly as the aspect ratio exceeds 40. The results from Eq. 5.29 are comparable to those given by others (Blizard et al. 1990, O'Donnell et al. 1996). Blizard et al. reported a maximum value of E_f = 28 GPa for the Vectra A950. This corresponds to our data, when the aspect ratio is above 40. O'Donnell et al. presented a range of modulus, from 10.3 to 18.2 GPa, for the Vectra A950 at different mold temperatures and plaque thickness, which corresponds to our calculations with aspect ratio ranging from 2 to 10.

5.4.4 Modulus of PET/LCP Blends

According to the preceding analysis, we have determined the model (Eq. 5.25) to describe the modulus of injection molded PET/LCP blends. The relationship between the aspect ratio and elongational strain, and that between the aspect ratio and the modulus of the LCP fibers are described by Eq. 5.26b and Eq. 5.29, respectively. Combining these two

equations together, we can predict the modulus of the PET/LCP blends using the following:

$$\frac{E}{E_m} = \frac{1 - 2B\sqrt{\frac{3}{2}}(\varepsilon+1)^{\frac{3}{2}} V_f}{1 - BV_f} \tag{5.30a}$$

with

$$B = \frac{E_f / E_m - 1}{E_f \Big/ E_m + 2\sqrt{\frac{3}{2}}(\varepsilon+1)^{3/2}}$$

and

$$E_f = \frac{1}{\exp(-2.2722 + 0.1834\log(2\sqrt{\frac{3}{2}}(\varepsilon+1)^{3/2})^{-2} + 0.0045\log(2\sqrt{\frac{3}{2}}(\varepsilon+1)^{3/2})^{-4})} \tag{5.30b}$$

We can deduce from Eq. 5.30 that the modulus of PET/LCP blends is actually a function of the elongational strain which, in turn, is determined by melt temperature, mold temperature, injection speed, and geometry of the mold cavity. Due to variation of the elongational strain with the Y coordinate as shown in Figures 5.16, and A6 - A10, the modulus E in Eq. 5.30 is that at a particular location of the mold cavity. We solved Eq. 5.30 by integrating it with respect to y, giving the modulus of PET/LCP blends as follows:

$$\begin{aligned} E_{total} &= \frac{2}{H}\int_0^{H/2} E dy \\ &= \frac{2E_m}{H}\int_0^{H/2} \frac{1 - \sqrt{6}B(\varepsilon+1)^{3/2} V_f}{1 - BV_f} dy \end{aligned} \tag{5.31}$$

A numerical integration is used to solve Eq. 5.31. The derivation of the integration (Eq. 5.31) is presented in Appendix D and the algorithm written to perform the numerical calculation was shown in Appendix C.

In the present study, the measured PET modulus ranging from 2.75 - 2.9 GPa, and three different volume fractions of the LCP (see Table 5.1) are used to calculate the modulus of the blends. The calculated results are shown in Figures 7.1 - 7.7, and discussion about these results are also presented in Chapter 7.

A flow diagram of the calculations for the velocity profile in the AMF region and the modulus of the LCP blends is shown in Figure 5.21.

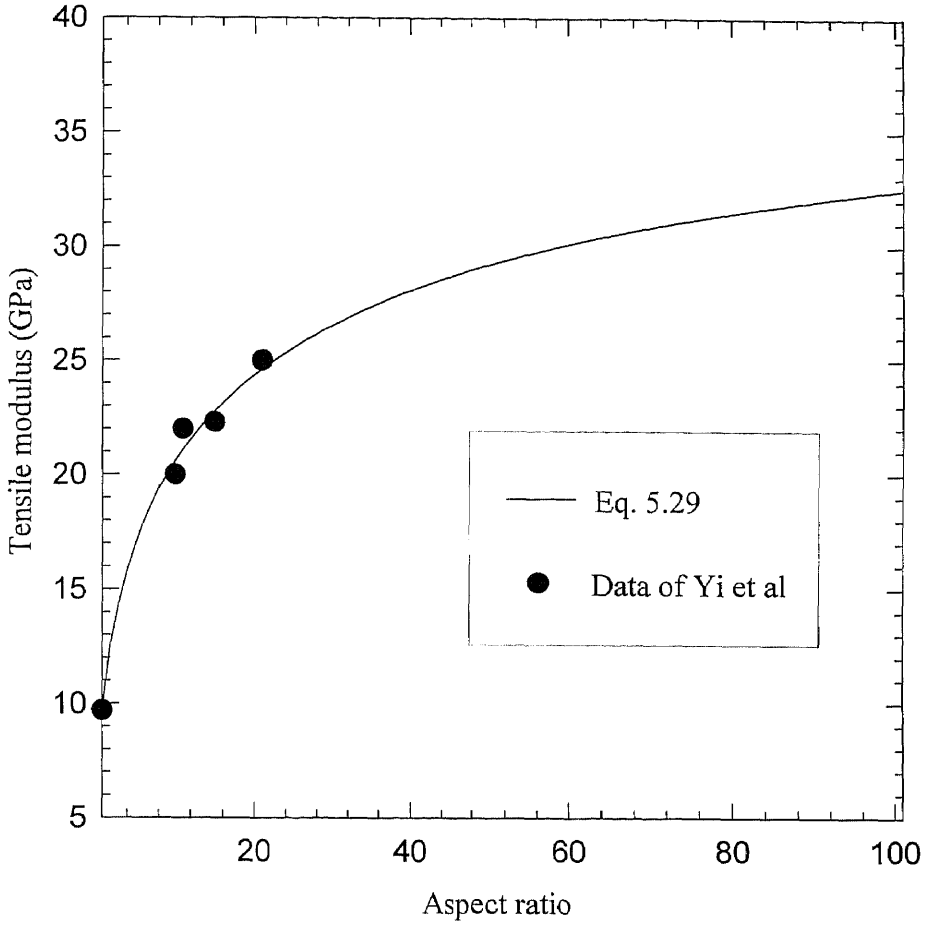

Figure 5.20 Modulus of Vectra A950 as a function of aspect ratio.

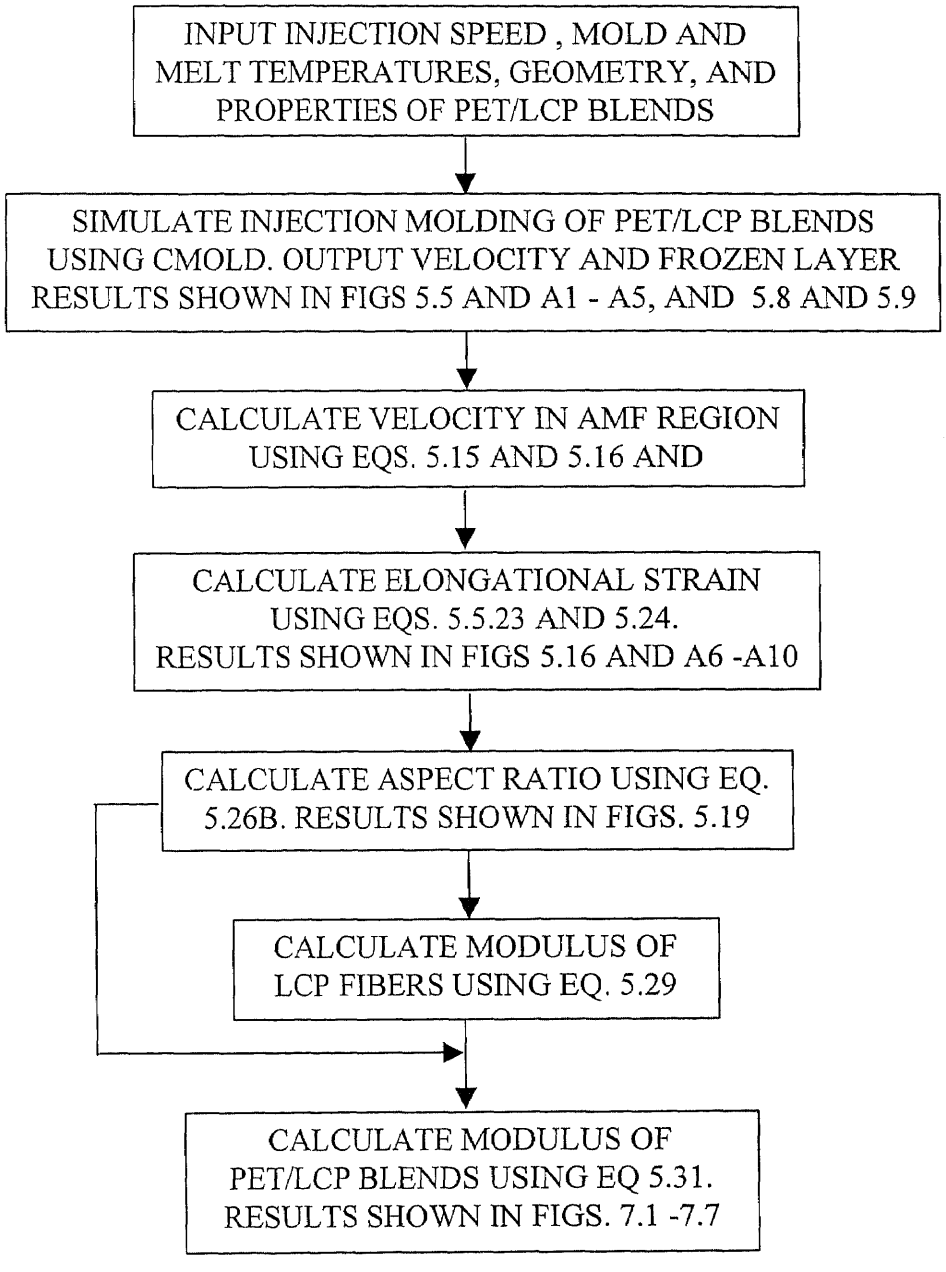

Figure 5.21 Flow diagram of the calculations for the velocity in the AMF region and the modulus of PET/LCP blends.

CHAPTER 6

MORPHOLOGY OF INJECTION MOLDED PET/LCP BLENDS

6.1 General

In order to complement the studies of mechanical properties of PET/LCP blends, the developing morphology of the blends as manifested in the solid state should be investigated. The reason is that the microstructure of the blends is as important as the molecular structure in determining the performance of these materials, and allows one to elucidate the variation of properties by correlating morphology development with properties.

In this chapter, emphasis is on the description of morphology of injection molded PET/LCP blends, and a distinct skin/core morphology of PET/LCP blends is presented. The effects of processing parameters such as injection speed, melt temperature, and mold temperature on the morphology development are discussed. We also predict the morphology development, and explain the relationship between the processing parameters and the morphology using our numerical analysis. Optical microscopy (OM) and scanning electron microscopy (SEM) were used in the analysis of morphology.

6.2 Skin/Core Structure of Injection Molded PET/LCP Blends

LCP blends are melt processed to form highly oriented and fibrous solid state materials with exceptional mechanical properties. In this study, injection molding process was used to produce the blends. The high orientation and fibrous structure in the blends develop as

a result of the effect of elongational flow on the easily extended chain molecules of LCPs. A highly anisotropy structure is developed during injection molding, including layers, parallel to the flow direction, and a skin-core morphology.

Layered structures in moldings are easily observed by optical microscopy even at a low magnification (60X). Figure 6.1 shows a reflected light micrograph of a polished half section of an injection molded sample (PET/LCP blend, 85/15 wt %). The light area in Figure 6.1 is the surface of the sample and the interface of light and dark areas is the edge of the sample. The arrow in the picture indicates the flow direction. The micrograph shows morphology variations from fiber-like textures near the skin area (right side of light area in the picture) to particles near the core area (left side of light area in the picture). The highly oriented structures are exhibited in the skin region and a sharp skin-core interface can be observed. The thickness of the skin zone is about 0.30 ~ 0.50 mm, 18 ~ 30% of half thickness of the sample. But we cannot observe the variation of fiber size along the thickness of the sample utilizing such low magnification.

The scanning electron micrograph in Figure 6.2 presents a detailed view of morphology variation of injection molded PET/LCP (85/15 wt %) blend from fibers in the skin region to particles in the core region. The LCP domains in the picture are easily distinguished from the dark PET matrix. The left side in the picture is the edge of the sample and the arrow indicates the flow direction of melt in the mold cavity. The individual fibers can be clearly observed in the skin zone and appear to be highly aligned in the flow direction, and many non-deformed LCP domains exists in the core region. Three sublayers can be approximately distinguished in the micrograph through differences in the size, shape, and orientation of the LCP domains. The first layer is the

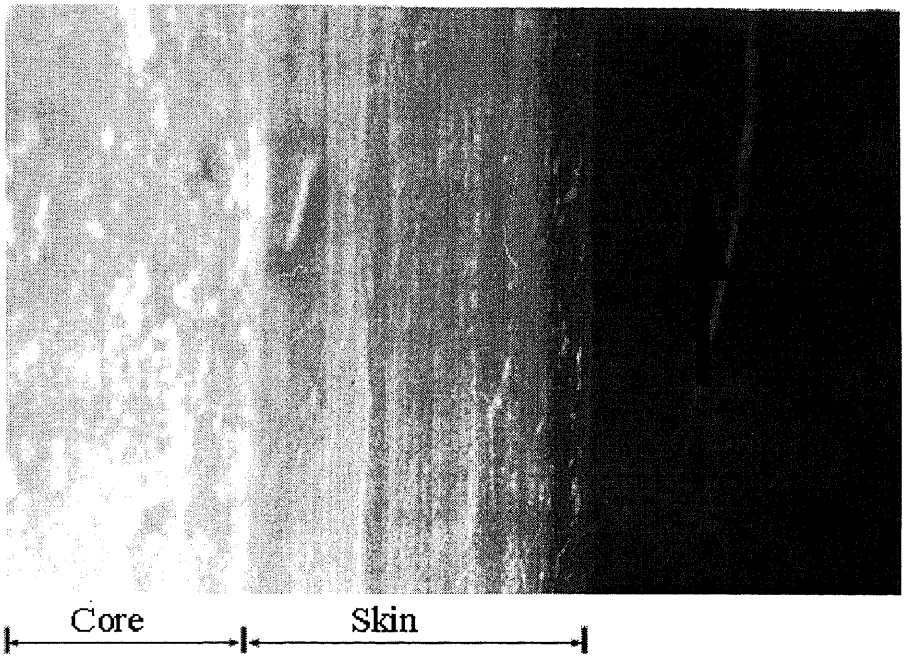

Figure 6.1 A reflected light micrograph (60X) of a polished half section of injection molded PET/LCP (85/15 wt %) blend at an injection speed 18 mm/s, a melt temperature of 320 °C, and a mold temperature of 18 °C.

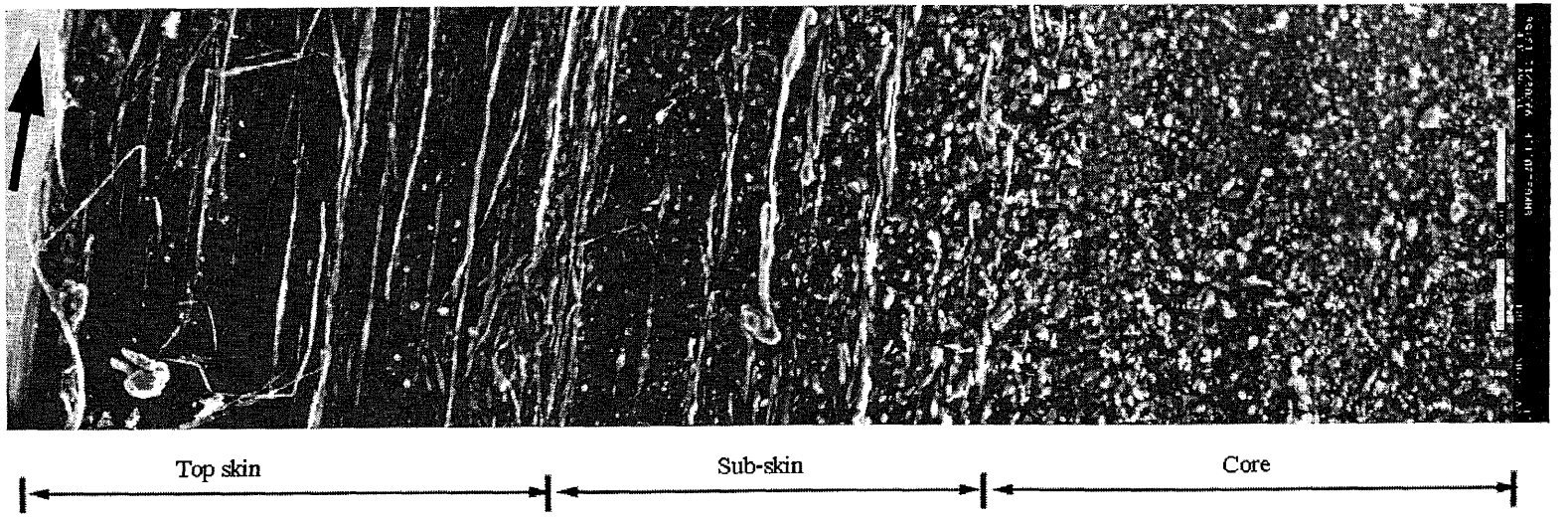

Figure 6.2 A SEM mircograph of a polished half section of injection molded PET/LCP (85/15 wt %) blend.

top skin, approximately 390 μm thick close to the edge of the sample, and consists of longer and highly oriented fibers. The diameters of the fibers range from 1.6 to 3.2 μm. The second is subskin, approximately 310 μm thick. Compared with the fibers in the top skin, the fibers in the subskin are shorter and less oriented, and the diameters of the fibers in the subskin range from 3.5 to 6.0 μm. But almost all of the fibers in the skin area (top and sub skins) are parallel to each other. Therefore, it is reasonable that the influence of the degree of fiber orientation on the mechanical properties of PET/LCP blends was not considered in the numerical analysis. The third layer is the core with non-deformed LCP domains. The aspect ratio of these non-deformed LCP domain is approximately equal to one.

The distribution of the LCP domains described above is a manifestation of effect of the fountain flow in the AMF (see detailed analysis in Chapter 5). In the fountain flow, the fluid elements near the center line flow towards the area close to the cavity wall and form the top skin area; the elements are stretched into long fibers and aligned along the flow direction in that area; the fluid elements away from the center line form many short fibers compared with those in the area close to the cavity wall (see Figure 5.15). The formation of the morphology in the core area is mainly controlled by shear flow behind the fountain flow in the AMF because the LCP domains in the core region did not experience the elongational flow in the AMF region. Elongational strains are very small in the core area as shown in Figures 5.16 - 5.18. As discussed in Chapter 2, the effect of shear flow on the deformation of LCP phase is very minimal. Therefore, one can deduce that the LCP phase in the core area exists in the form of spheres or ellipsoids because of low shear rate in the core area.

Figure 6.3 shows the distribution of fiber size across the thickness of a sample, based on Eqs 5.23 and 5.26b. In Figure 6.3, the center of mold cavity is at 0, and the cavity wall is at about 1.6. From 0 to approximately 0.9, the lengths of the fibers are

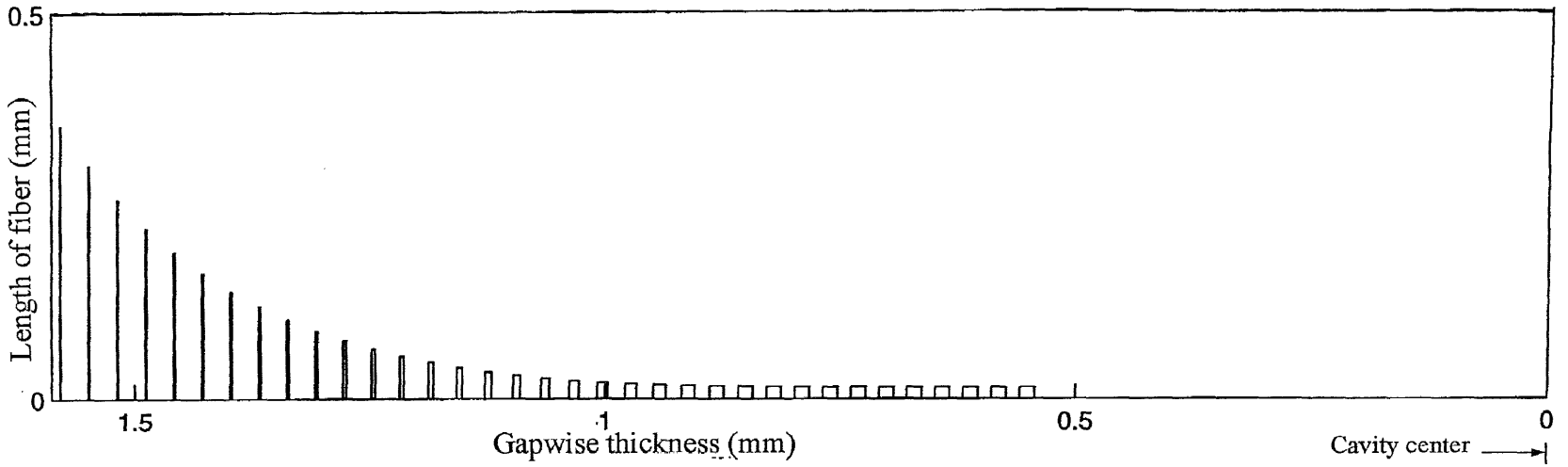

Figure 6.3 Prediction of fiber distribution across the thickness of mold cavity.

Figure 6.4 A SEM micrograph of LCP fibers following extraction of PET matrix from PET/15 % LCP blend.

approximately equal to their diameters. This corresponds to the core region in Figure 6.2. From 0.9 to approximately 1.3, many short fibers exist. This distribution is similar to that in the subskin shown in Figure 6.2. Above 1.3, there is a sharp increase in length of the fibers; such an increase can be observed on the top skin in Figure 6.2. From the above discussions, we can deduce that the prediction shown in Figure 6.3 is in a very good agreement with the experimental results shown in Figures 6.1 and 6.2. Obviously, the LCP domains in the top skin experienced higher elongation than those in the subskin, and the core regions, as shown in Figures 5.16a -5.16f. From the edge of the sample to the core, the lengths of the fibers change gradually from large to small across the thickness direction.

Figure 6.4 shows a more detailed morphology of the LCP fibers in the PET/ 15% LCP blend at 450X, taken from the area between the top skin and subskin. The microstructure of the skin material shows fibers with 1.5 ~ 4.5 μm in diameter. The fibrous LCP particles are still very non-uniform in their length. Some non-deformed LCP domains can be seen in the micrograph.

6.3 Effect of Injection Molding Parameters on Morphology of PET/LCP Blends

In this section, the morphologies of samples created by varying injection speeds, melt temperatures, and mold temperatures are analyzed in attempts to determine some morphological differences, which could be related to the differences in the mechanical properties of the LCP blends. The morphological variation could be determined in terms of orientation of the LCP phase, aspect ratio of the LCP fibers, and the skin layer.

6.3.1 Injection Speed

Increase of injection speed results in a fast advancing melt front. In the fountain flow region, fluid elements flow towards the skin area in a short time, and if the melt front moves fast, then their deformation time will be small. As seen from the predictions of

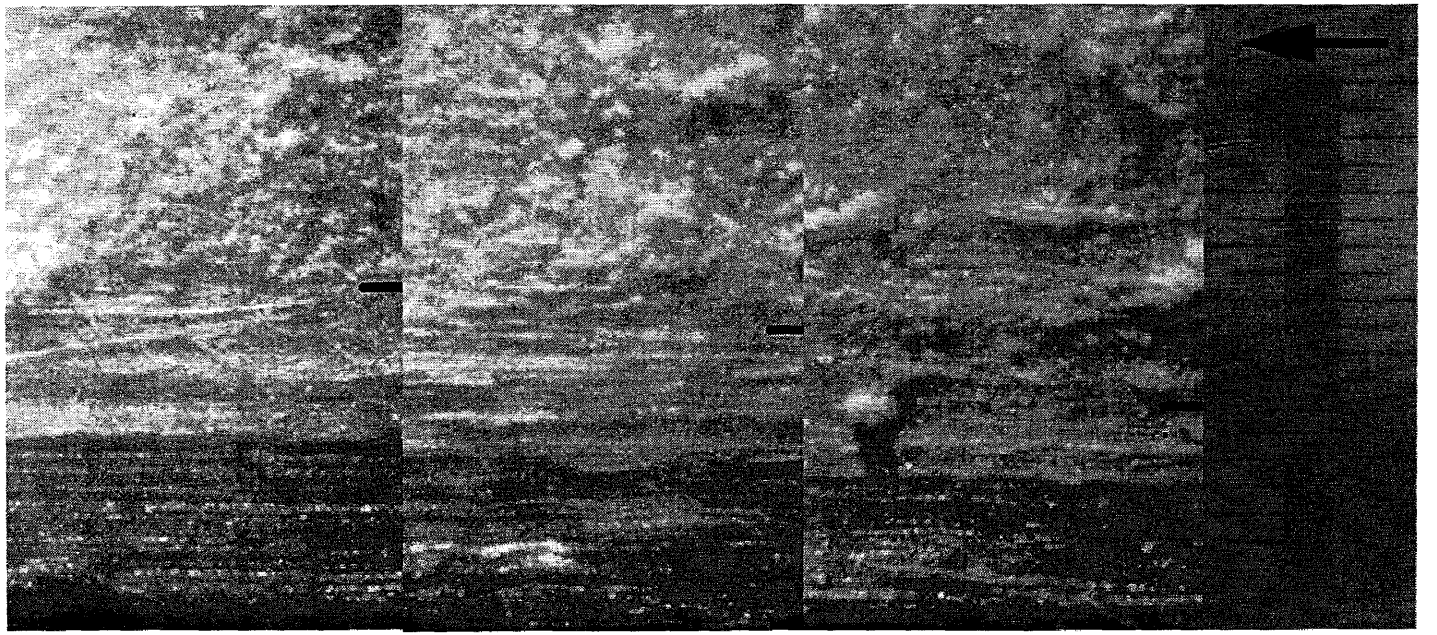

(a) (b) (c)

Figure 6.5 Optical micrographs of structure development of PET/LCP (85/15 wt %) blend at a melt temperature of 320 °C, a mold temperature of 18 °C, and different injection speeds of (a)13, (b) 15, and (c) 21 mm/s from left to right, respectively. The black bars represent approximately the interface between skin and core regions. The arrow indicates the flow direction. The scale is in mm and each major division is 0.1 mm.

Figures 5.16a - 5.16f, high injection speed generates small elongational strain. This means that fluid elements are stretched longer at low injection speeds than at high injection speed and more fluid elements are subjected to elongation at low injection speed. The generation of much more deformed fluid elements results in a thick skin layer.

Injection speed also has an effect on the aspect ratio of the fibers (see Figure 5.19); the aspect ratio increases as the injection speed decreases. But we cannot validate the calculation results using experiment because it is difficult to measure the aspect ratio at our present experimental conditions.

Figure 6.5 presents the different morphologies of injection molded PET/LCP (85/15 wt %) blends created by varying injection speeds. These photographs were taken with an optical microscope at 60X. The bottom of each photograph is the edge of the samples and the top is the core of the samples. From the bottom to the top, distinct variation in morphology can be seen. In the skin region (close to the edge) there are many highly oriented textures. The black bars in the pictures indicate, approximately, the interface of the skin and core regions. From left to right of the picture, the injection speed increased from 13 to 21 mm/s, and the skin layer is reduced. The thickness of the skin layer in Figure 6.5 (a) ranges from 0.60 ~ 0.62 mm while the thickness of skin layer in Figure 6.5 (c) is about 0.40 mm. The thickness of the skin layer decreases by approximately 30% while the injection speed increases by 60 %.

Figure 6.6 shows the results of measuring the skin layers using the Matrix Videometrix Econoscope mentioned in Chapter 4. When injection speed is increased from 13 to 21 mm/s, the thickness of the skin layers changes from 0.575 to 0.410 mm at a melt temperature of 320 ^{o}C, and from 0.605 mm to 0.426 mm at 304 ^{o}C. Figure 6.6 also shows the calculated skin layers at different injection speeds. The calculated thickness of the skin layer is defined as half the thickness of the samples minus the Y coordinate where the calculated aspect ratio tends to approximately 1 ~ 2. As shown in Figure 6.6, predictions presented the same decreasing trend in the thickness of the skin layer as the

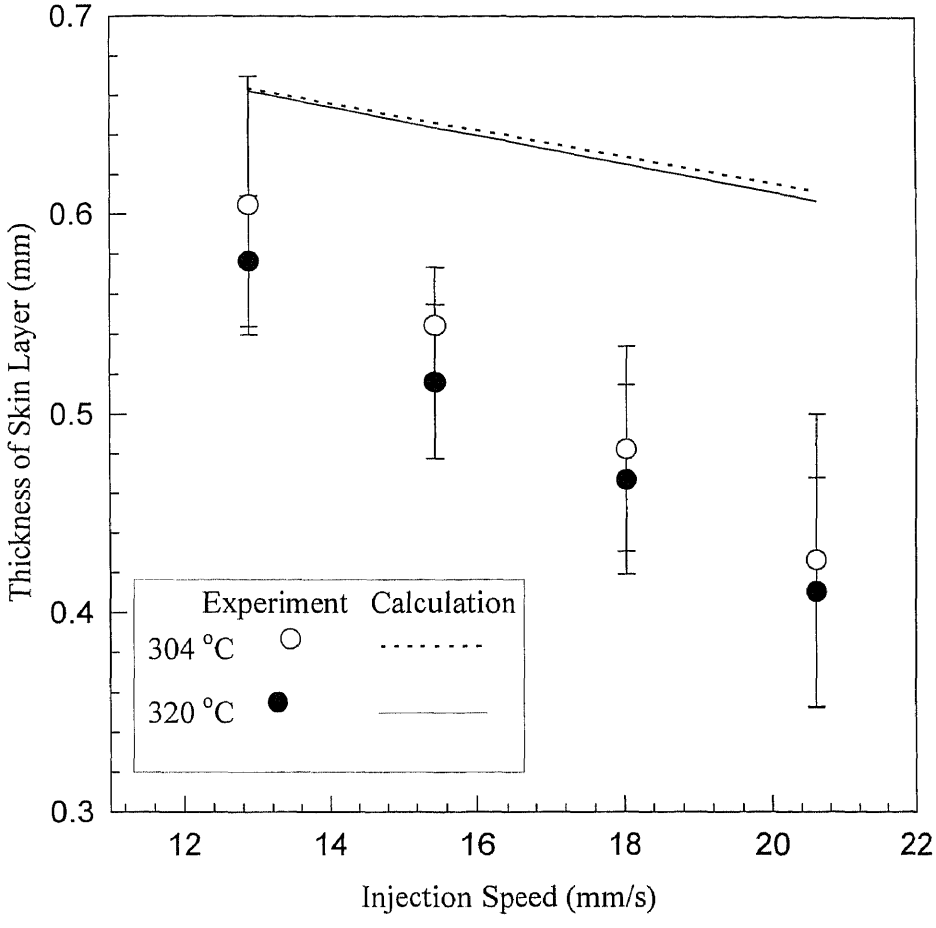

Figure 6.6 Thickness of skin layer as a function of injection speed for PET/LCP (85/15 wt %) blend at a mold temperature of 18 °C. The date are shown with ±1δ.

experimental results with increasing injection speed although there is a large discrepancy between calculated and experimental data. The large discrepancy results from the different criteria used to determine the interface of skin and core layers in measurement and calculation. In the measurement of the skin layer, the area where most of the LCP domains exist in the elongated shape is defined as the skin region. In the calculation of the skin layer, the region where the aspect ratio of LCP domains is larger than unity is defined as the skin region. We can see from Figure 6.2 that even in the core area many deformed LCP domains exist but we cannot say that the area belongs to the skin region. Obviously, the measured values of the skin layer are less than the calculated ones.

Figures 6.7 - 6.10 are the SEM micrographs of injection molded PET/LCP (85/15 wt %) blends, at different injection speeds: 13, 15, 18, and 21 mm/s, and at a melt temperature of 320 °C and a mold temperature of 18 °C. The left of the top micrograph is the edge of the samples. The right of the bottom micrograph is the core of the samples. Black triangles identify identical areas on the top and bottom micrographs. The arrow indicates the flow direction. From these micrographs, distinct variation in the thickness of the skin layers can be observed. In Figure 6.7, the thickness of the skin layer is about 0.6 mm. In Figure 6.10, the skin layer is approximately 0.53 mm thick. There are many long LCP fibers in the skin region of the sample shown in Figure 6.7 compared with those shown in Figure 6.10. But it is difficult to see significant differences in diameter and length of the LCP fibers from these micrographs.

These SEM micrographs have shown that an increase of the injection speed has resulted in a decrease of the thickness of the skin layer. This is in agreement with the analysis made previously in this section. It is also seen that longer LCP fibers were observed at low injection speed than at high injection speed. The variation in the skin layer with the injection speed is also reflected in the mechanical properties of the blends. The latter is discussed in Chapter 7.

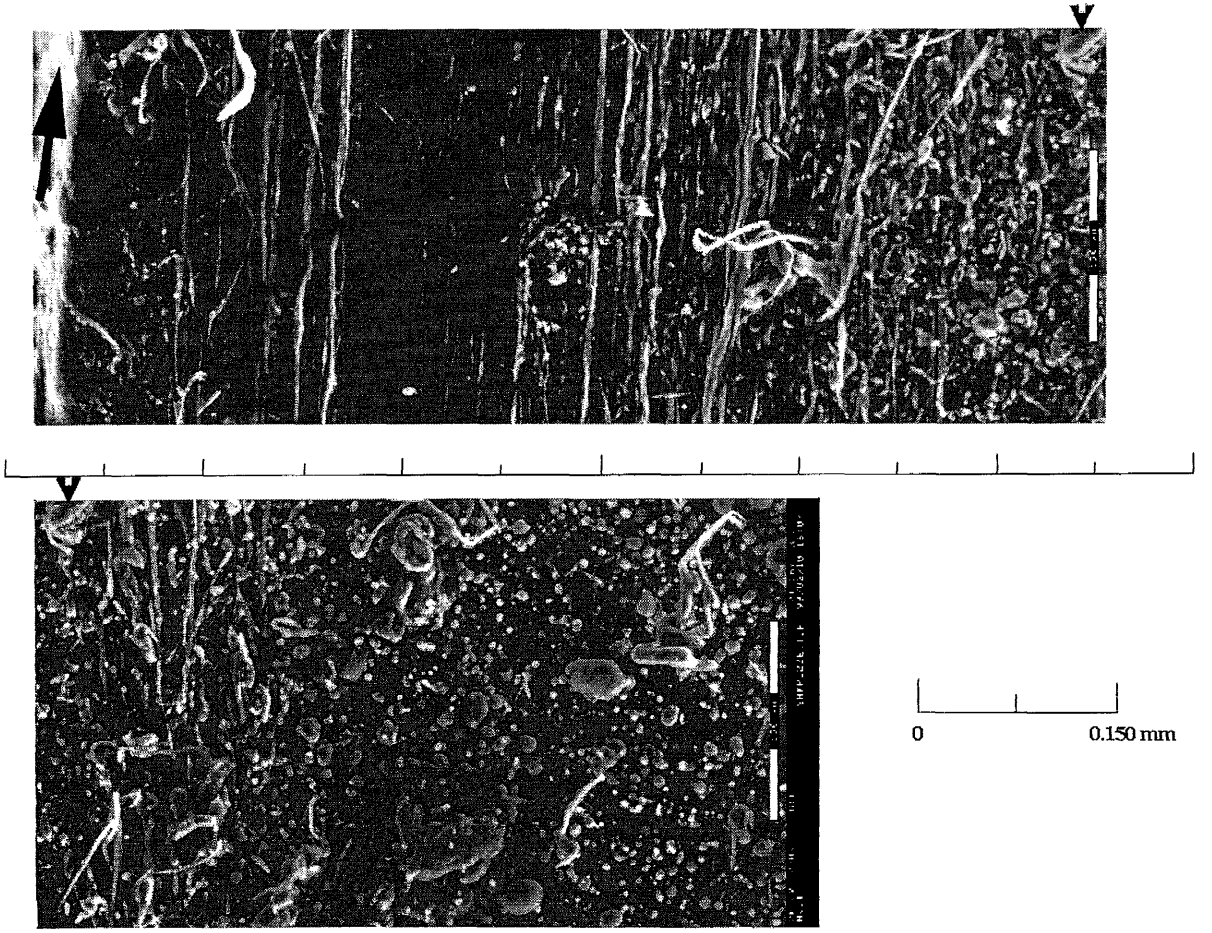

Figure 6.8 A SEM micrograph of injection molded PET/LCP (85/15 wt %) blend at a mold temperature of 18 °C, a melt temperature of 320 °C, and an injection speed of 15 mm/s.

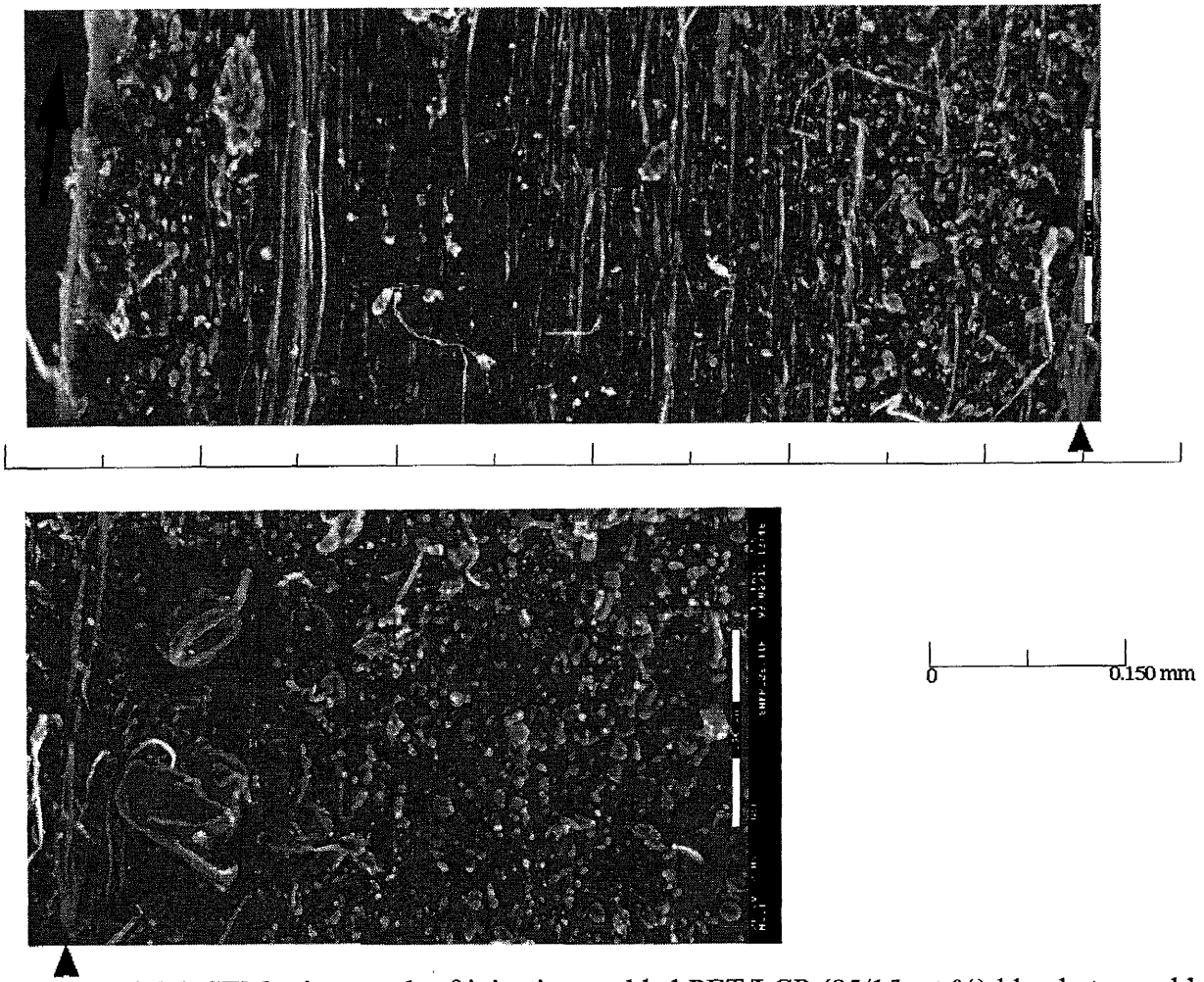

Figure 6.7 A SEM micrograph of injection molded PET/LCP (85/15 wt %) blend at a mold temperature of 18 °C, a melt temperature of 320 °C, and an injection speed of 13 mm/s.

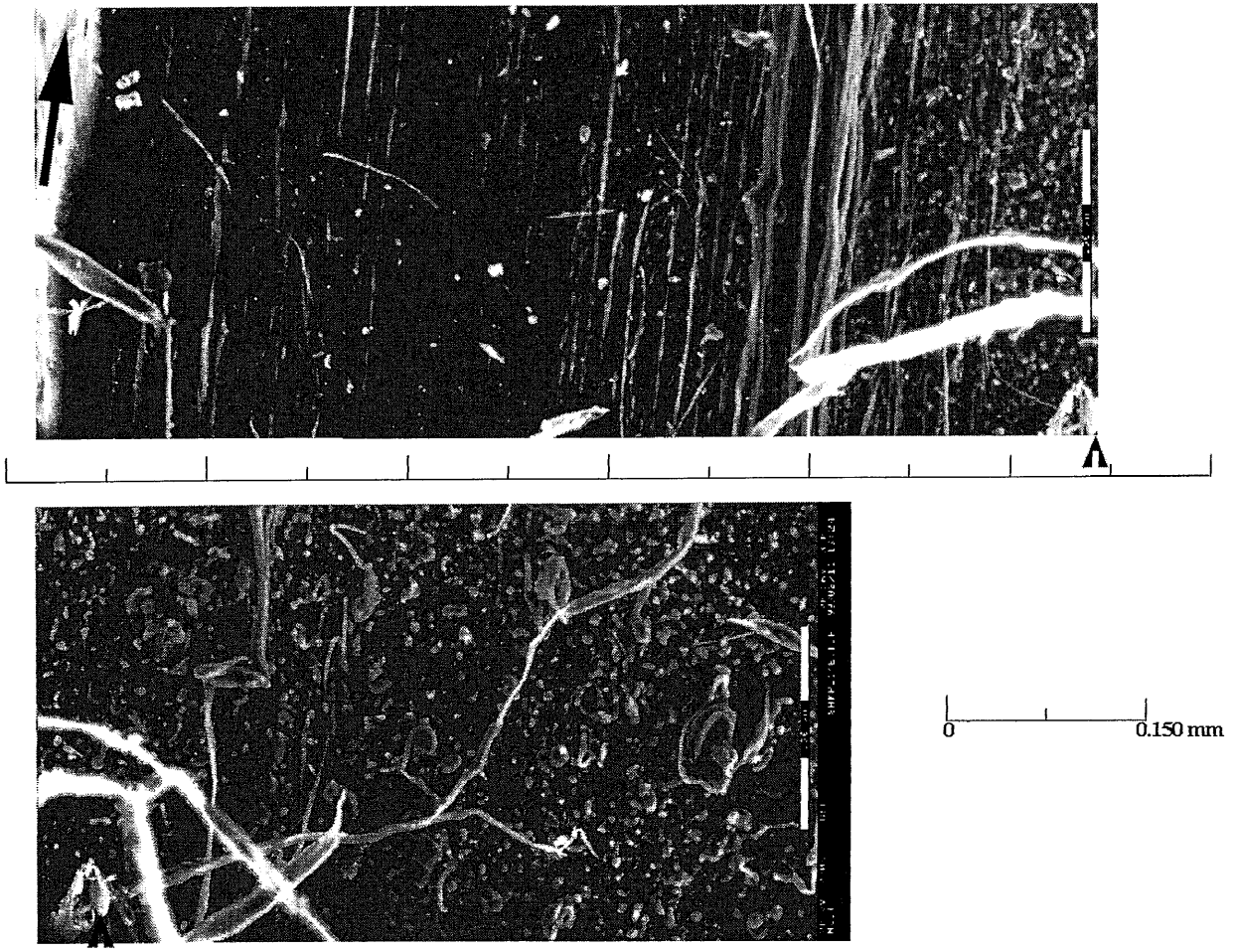

Figure 6.9 A SEM micrograph of injection molded PET/LCP (85/15 wt %) blend at a mold temperature of 18 °C, a melt temperature of 320 °C, and an injection speed of 18 mm/s.

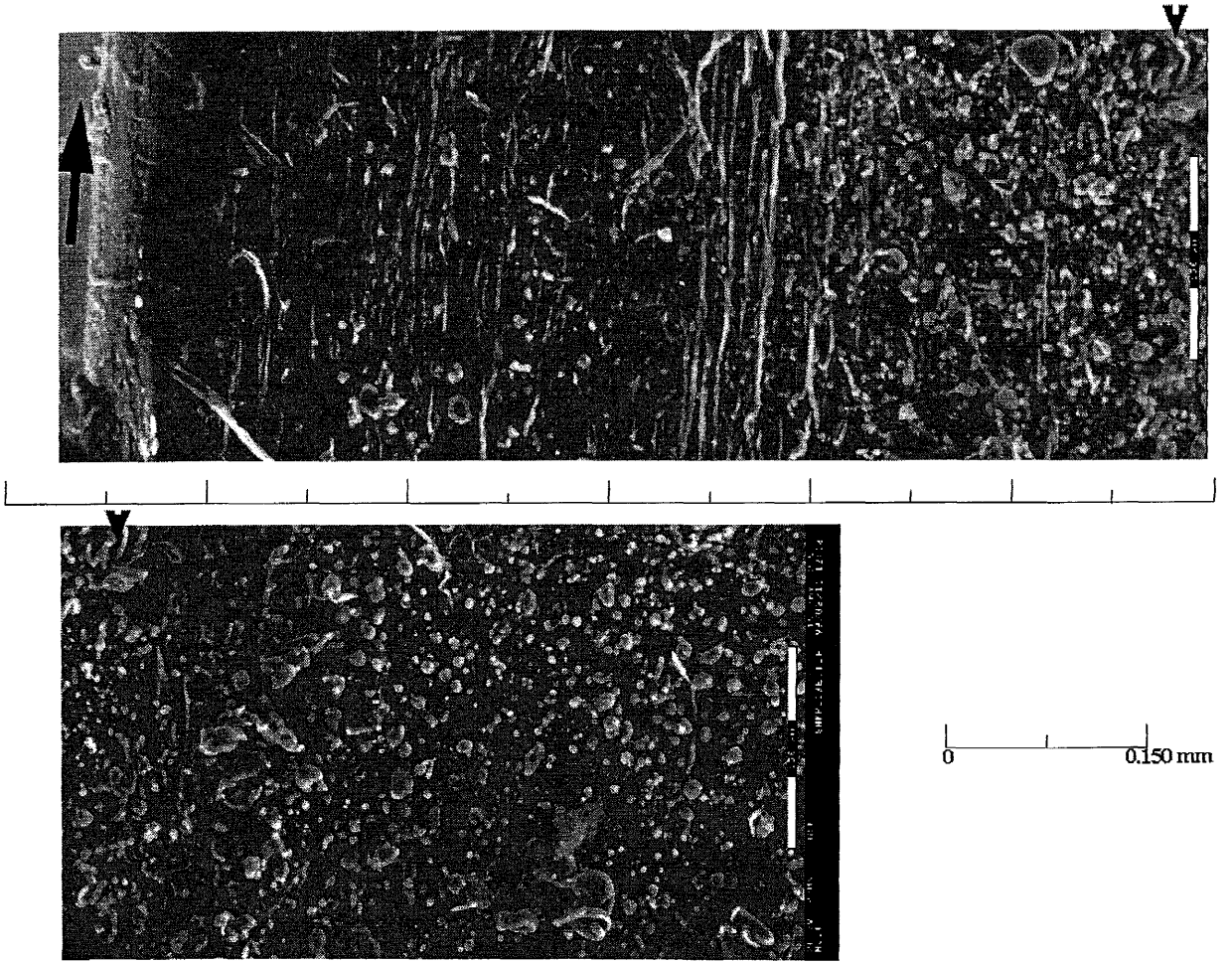

Figure 6.10 A SEM micrograph of injection molded PET/LCP (85/15 wt %) blend at a mold temperature of 18 °C, a melt temperature of 320 °C, and an injection speed of 21 mm/s.

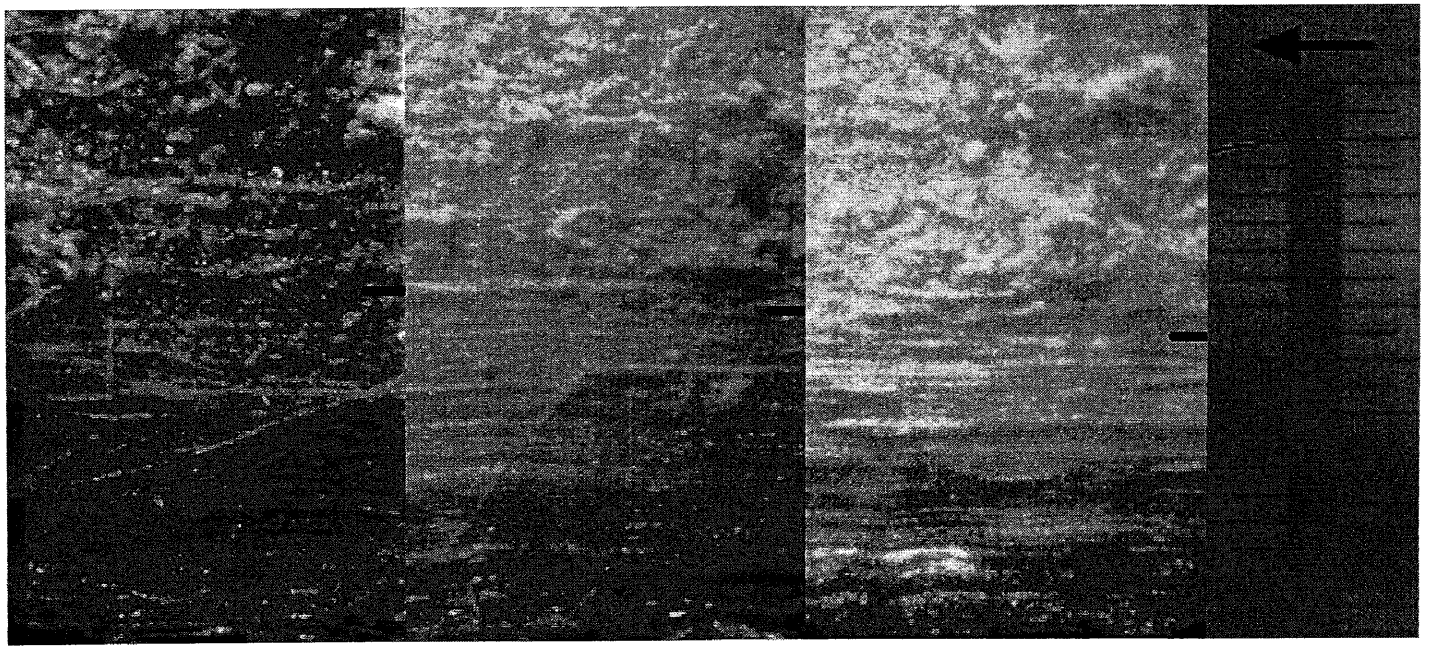

(a) (b) (c)

Figure 6.11 Optical micrographs of structure development of PET/LCP (85/15 wt %) blend at a mold temperature of 18 °C, and an injection speed of 15 mm/s, and different melt temperatures of (a) 304, (b) 310, and (c) 320 °C from left to right, respectively. The black bars represent approximately the interface between skin and core regions. The arrow indicates the flow direction. The scale is in mm and each major division is 0.1 mm.

6.3.2 Melt Temperature

Figure 6.11 presents the morphologies of injection molded PET/LCP (85/15 wt %) blends at different melt temperatures. From left to right, melt temperatures are 304, 310, and 320°C, respectively. As seen, low melt temperature favor the formation of thick skin layers. This is because high melt temperatures reduce the viscosity of polymer melt resulting in the fast movement of the polymer melt. The fast movement of the polymer melt will weaken the formation of a thick skin layer as discussed in section 6.3.1. Figure 5.5 also shows that the polymer melt in the mold cavity flows faster around the center of the mold cavity at high melt temperature than at low melt temperature. Here, the effect of crystallization of PET is not considered because the rate of crystallization of PET is very low at present processing conditions (Chan and Isayev 1992). The samples of PET produced at present processing conditions is almost transparency. It is shown that the rate of crystallization is very low.

Dietz et al. (1978) have reported that melt temperature is inversely proportional to the thickness of the frozen layer, and that this follows the relationship:

$$\delta \approx 1.9\left(\frac{T_T - T_w}{T_m - T_w}\right)\sqrt{\alpha t_c} \tag{6.1}$$

where δ is the thickness of the frozen layer; T_T, T_w, and T_m are the transition temperature, the mold temperature, and melt temperature, respectively; α is the thermal diffusivity; and t_c is the contact time between melt and mold wall. Eq. 6.1 indicates that the thickness of the frozen layer increases with decreasing melt temperature. It is shown that more deformed LCP domains can be frozen in skin layer while a thick frozen layer occurs, which aids the formation of a thick skin layer. Our numerical analysis also shows that thinner frozen layer is obtained at high melt temperature (see Figure 5.8).

The melt temperature can also influence the magnitude of fiber aspect ratio (see Figure 5.19). At low melt temperature many more fibers can be generated, which should result in a thick skin layer. But the effect on the aspect ratio is not distinct.

The effects of melt temperature on the thickness of skin layer for PET/LCP (85/15 wt %) blend are shown in Figure 6.12. As the melt temperature changes from 304 to 320 ^{o}C, the thickness of the skin layers vary from about 0.545 to 0.510 mm. Although melt temperature increases by 16 ^{o}C, the thickness of the skin layer changes slightly. Compared with the effect of injection speed on the thickness, the effect of melt temperature is not apparent. In Figure 6.12, the calculated thickness of the skin layer is presented. Both calculated and experimental results show that the skin layer can not be changed much by increasing melt temperature. This is because the formation of morphology near the interface between the skin and core regions, or the thickness of the skin layer is dependent mainly on the flow of the polymer melt near the interface. But the flow of the polymer melt near the interface varies slightly with melt temperature, and the variation of melt temperature changes mainly the flow in the center of cavity (see Figure 5.7). The reason of big discrepancy between the calculations and measurements shown in Figure 6.12 is the different criteria used to determine the interface of the skin and core layers as discussed in section 6.3.1. Figures 6.8 and 6.13 - 6.14 are the SEM micrographs of injection molded PET/LCP (85/15 wt %) blends at different melt temperatures of 320, 310, and 304 ^{o}C, respectively. It is difficult to discern any large change in the thickness of the skin layer at different melt temperatures. It is also shown that melt temperature can change the morphology of the blends but the variation in the morphology with of melt temperature is not distinct.

6.3.3 Mold Temperature

Low mold temperature means a higher temperature difference between the polymer melt and the wall of the mold cavity. Therefore, the rate of heat conduction to the cavity wall

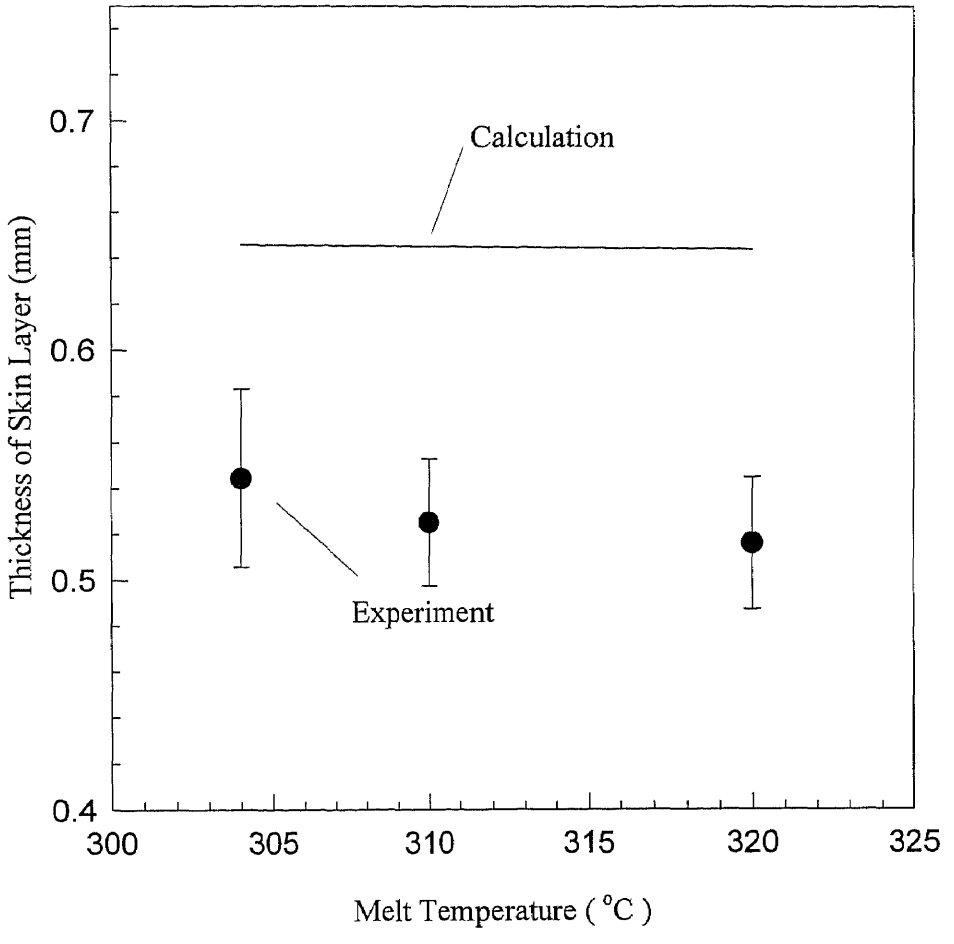

Figure 6.12 Thickness of skin layer as a function of melt temperature for PET/LCP (85/15 wt %) blend at an injection speed of 15 mm/s and a mold temperature of 18 °C. The date are shown with ±1δ.

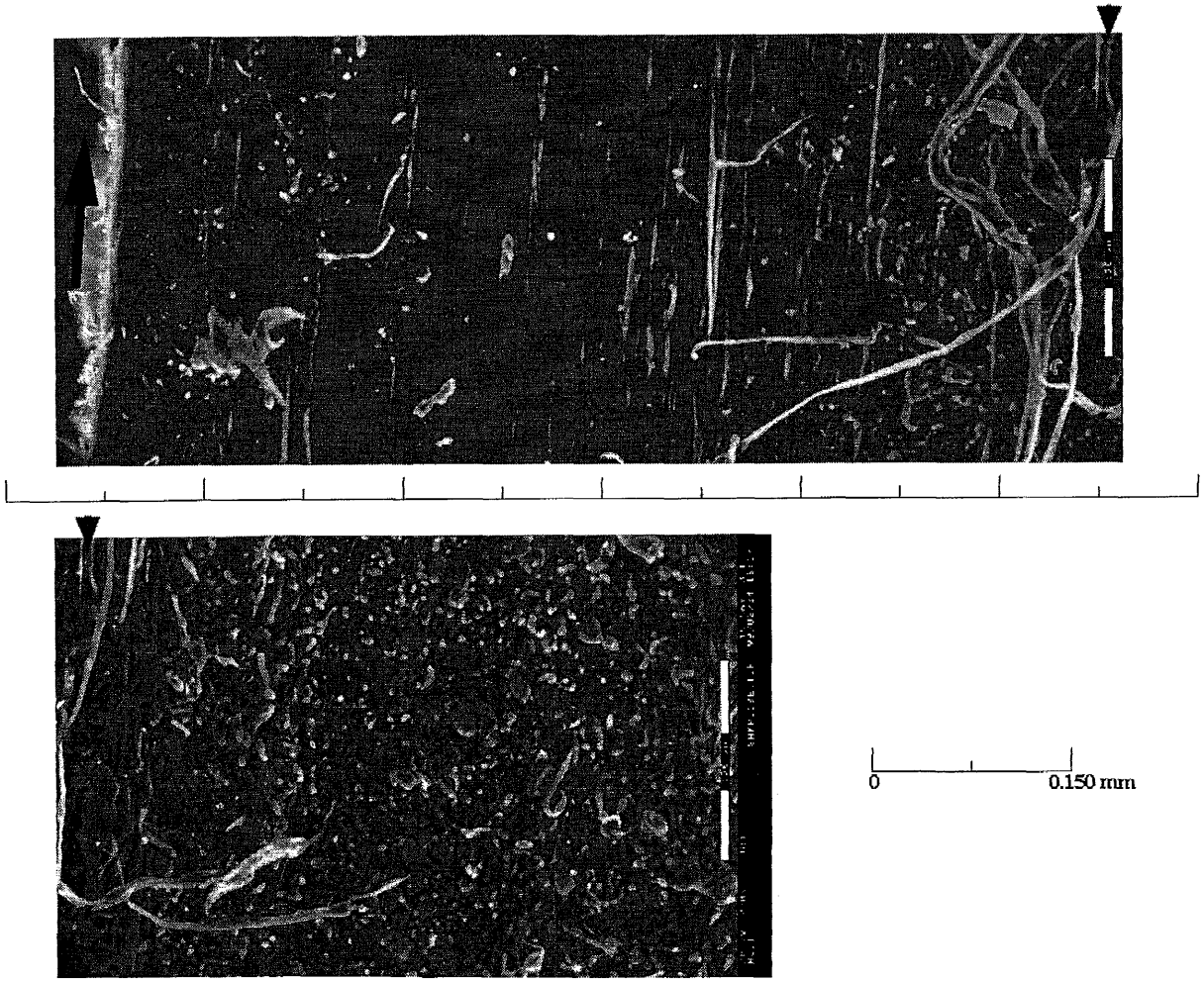

Figure 6.13 A SEM micrograph of injection molded PET/LCP (85/15 wt %) blend at a mold temperature of 18 °C, a melt temperature of 310 °C, and an injection speed of 15 mm/s.

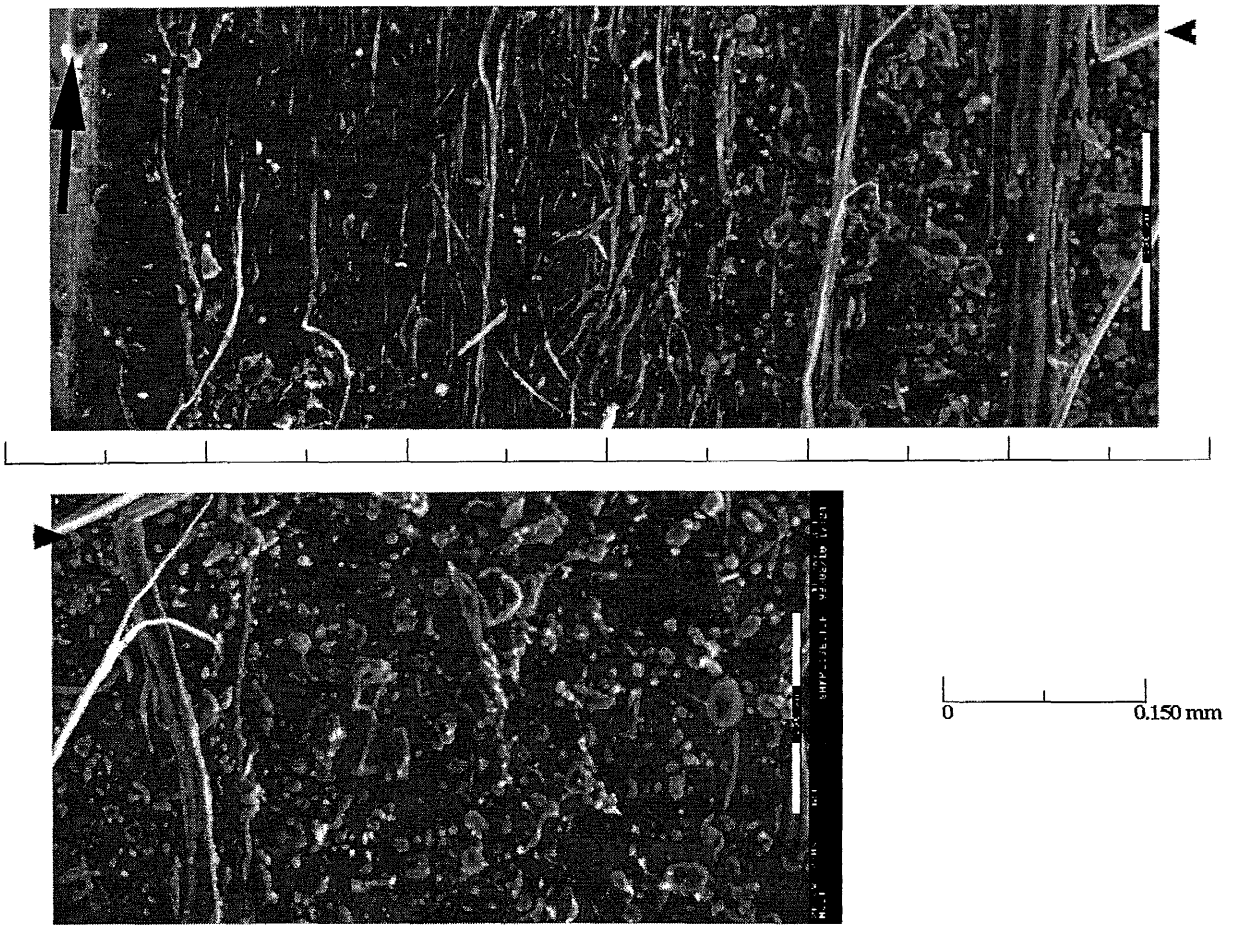

Figure 6.14 A SEM micrograph of injection molded PET/LCP (85/15 wt %) blend at a mold temperature of 18 °C, a melt temperature of 304 °C, and an injection speed of 15 mm/s.

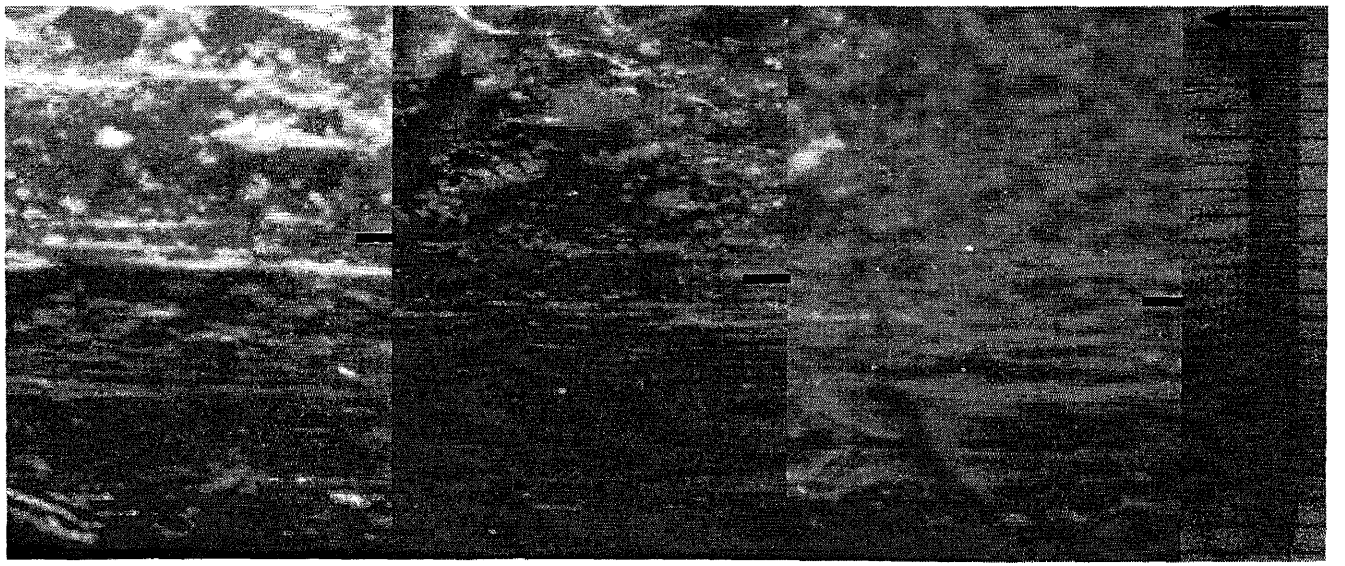

(a) (b) (c)

Figure 6.15 Optical micrographs of structure development of injection molded PET/LCP (85/15 wt %) blend at a melt temperature of 320 °C, and an injection speed of 15 mm/s, and different mold temperatures of (a) 18, (b) 35, and (c) 50 °C from left to right, respectively. The black bars represent approximately the interface between skin and core regions. The arrow indicates the flow direction. The scale is in mm. and each major division is 0.100 mm.

will increase rapidly and a thicker frozen layer will form. Figure 5.9 also shows the variation of the thickness of frozen layer as a function of the mold temperature based on the simulation of injection molded PET/LCP blends. Thicker frozen layer can result in the formation thick skin layer as discussed in section 6.3.2.

Figure 6.15 shows the photographs of three samples (PET/15% LCP blend) with different skin layers, which were created by varying mold temperature. From left to right, the thickness of the skin layer changes approximately from 0.570 mm to 0.490 mm with the mold temperature increasing from 18 °C to 50 °C. The reason for the variation of the

skin layer as a function of the mold temperature could be that the formation of the interface between the skin and core regions is dependent mainly on the flow of polymer melt near the interface, which is largely influenced by the mold temperature (see Figure 5.7). Another possible reason is that lower mold temperature aids the formation of LCP fibers because the aspect ratio of the fibers increase with decreasing mold temperature (see Figure 5.18). If there are many LCP fibers to form near the interface, a thick skin layer is induced. Therefore, at low mold temperature, a thick skin layer occurs.

Figure 6.16 compares the predicted and the measured thickness of the skin layer as a function of mold temperature for injection molded PET/LCP (85/15 wt %) blend. Both predicted and measurement results show the same trend, i.e. that the thickness of the skin layer increases as the mold temperature decreases. The reason of big discrepancy between the calculations and measurements is referenced to the discussion in section 6.3.1.

Figures 6.14 and 6.17 - 6.18 are SEM micrographs, showing the different morphologies formed at different mold temperatures of 18, 35, and 50 °C. As seen, the thickness of the skin layers increases as the mold temperature increases.

The experimental results confirm the analysis made above, i.e. that the skin layer is thicker at low mold temperature. We also found from these Figures that, at high mold

temperatures, the size of the LCP domain in the core region is small. The reason is not clear at this stage and we are investigating it further.

6.4 Morphologies of PET/LCP Blends with Different LCP Contents

Figures 6.17 and 6.19 - 6.20 show the morphologies at LCP contents of 5 %, 15 %, and 25 %. As expected, much more LCP fibers were found at the skin region for PET/LCP (75/25 wt %) blend. The skin layer of the blend is obviously thicker than that of others. The fibers of PET/LCP (75/25 wt %) blend in the skin region are very uniform. From these pictures, we can see that it is the most effective way to change the morphologies of PET/LCP blends by increasing LCP content but the cost of the materials also increases.

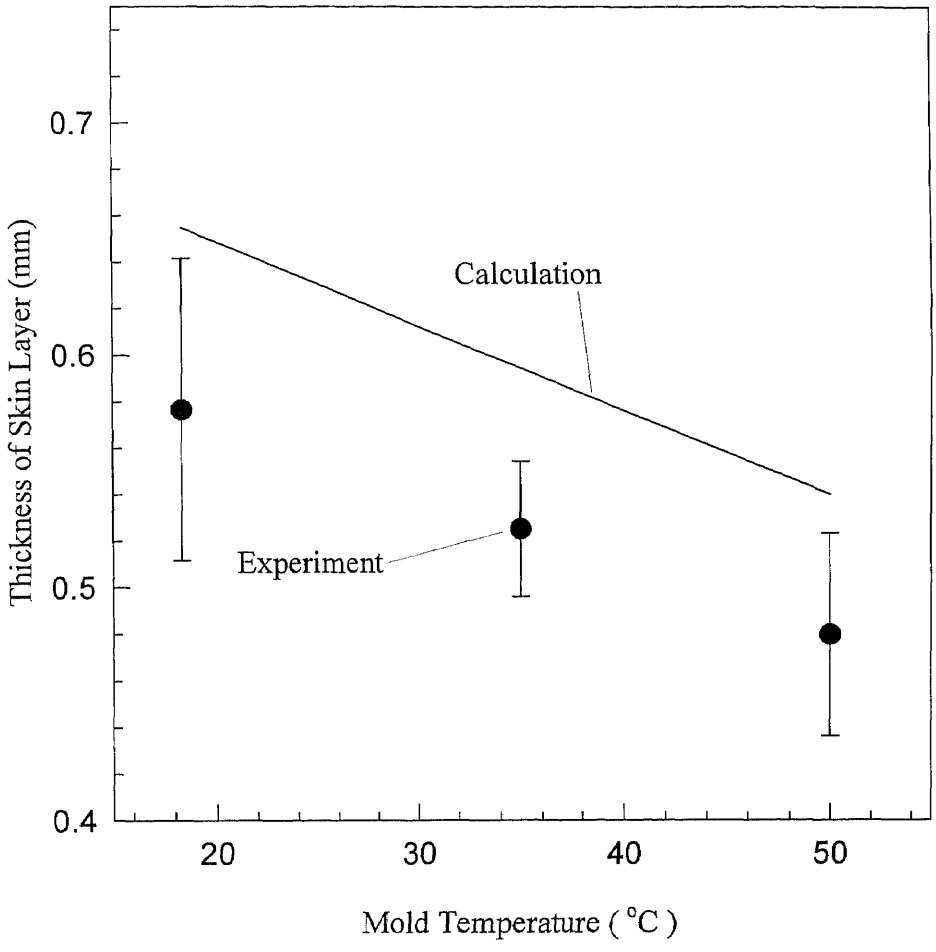

Figure 6.16 Thickness of skin layer as a function of mold temperature for PET/LCP (85/15 wt %) blend at an injection speed of 13 mm/s and a melt temperature of 320 °C. The date are shown with ±1δ.

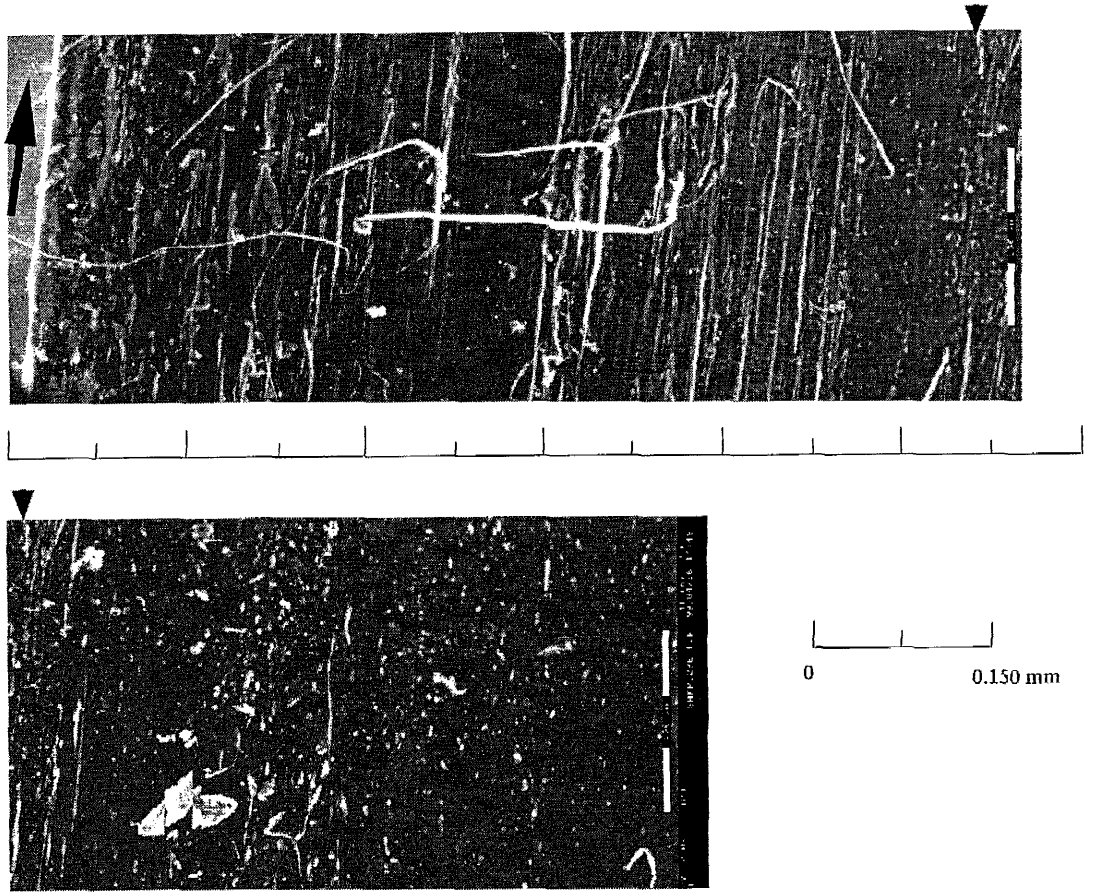

Figure 6.17 A SEM micrograph of injection molded PET/LCP (85/15 wt %) blend at a mold temperature of 35.00 °C, a melt temperature of 304 °C, and an injection speed of 15 mm/s.

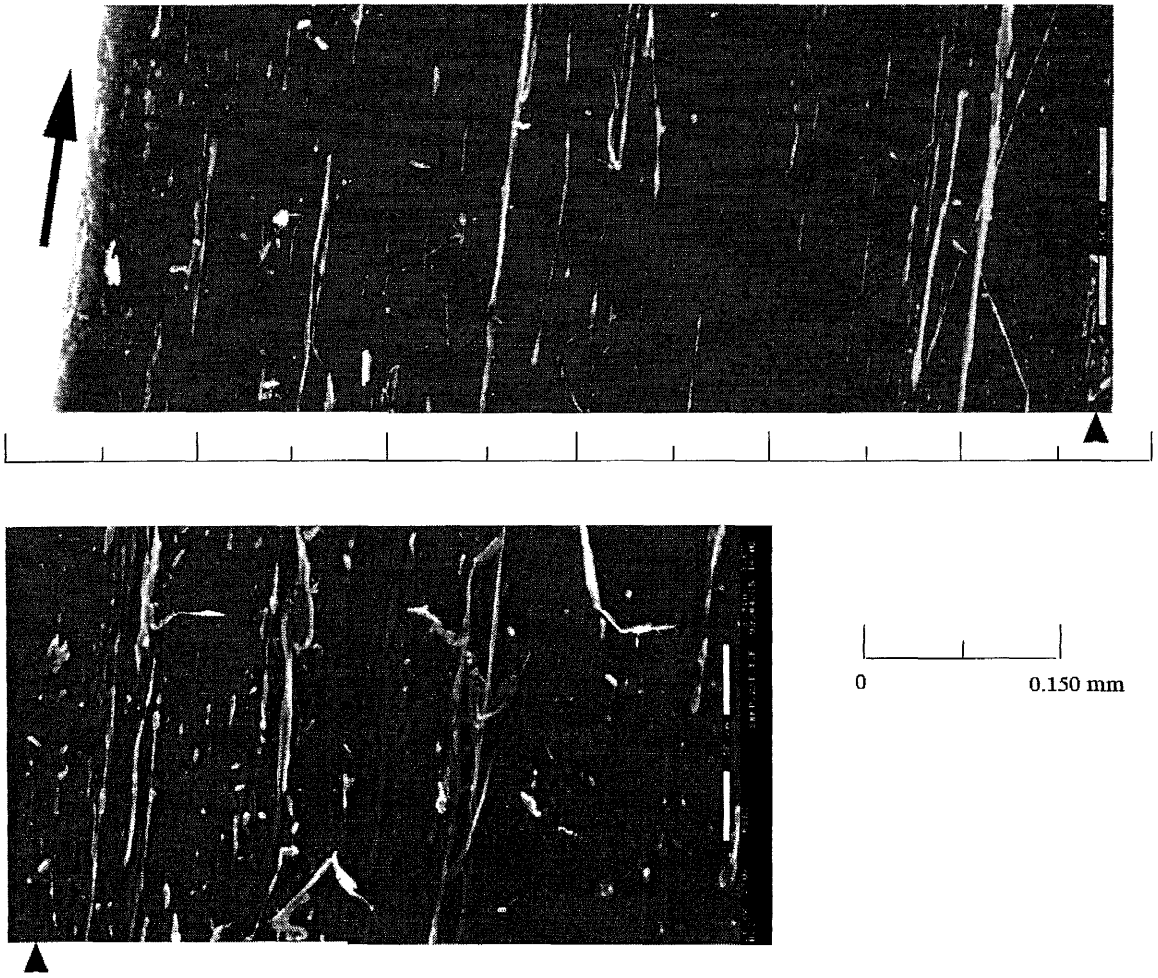

Figure 6.18 A SEM micrograph of injection molded PET/LCP (85/15 wt %) blend at a mold temperature of 50.00 °C, a melt temperature of 304 °C, and an injection speed of 15 mm/s.

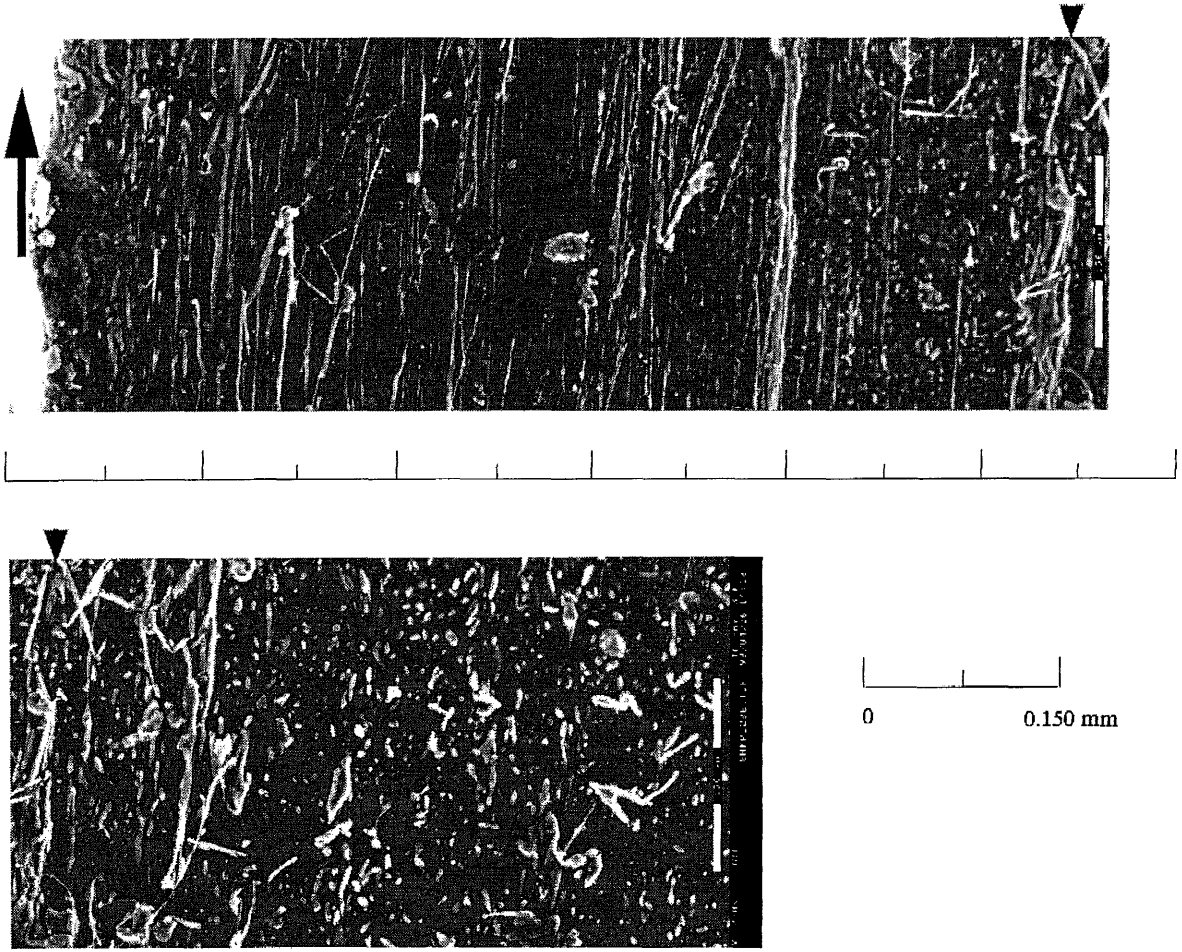

Figure 6.19 A SEM micrograph of injection molded PET/LCP (75/25 wt %) blend at a mold temperature of 35.00 °C, a melt temperature of 304 °C, and an injection speed of 15 mm/s.

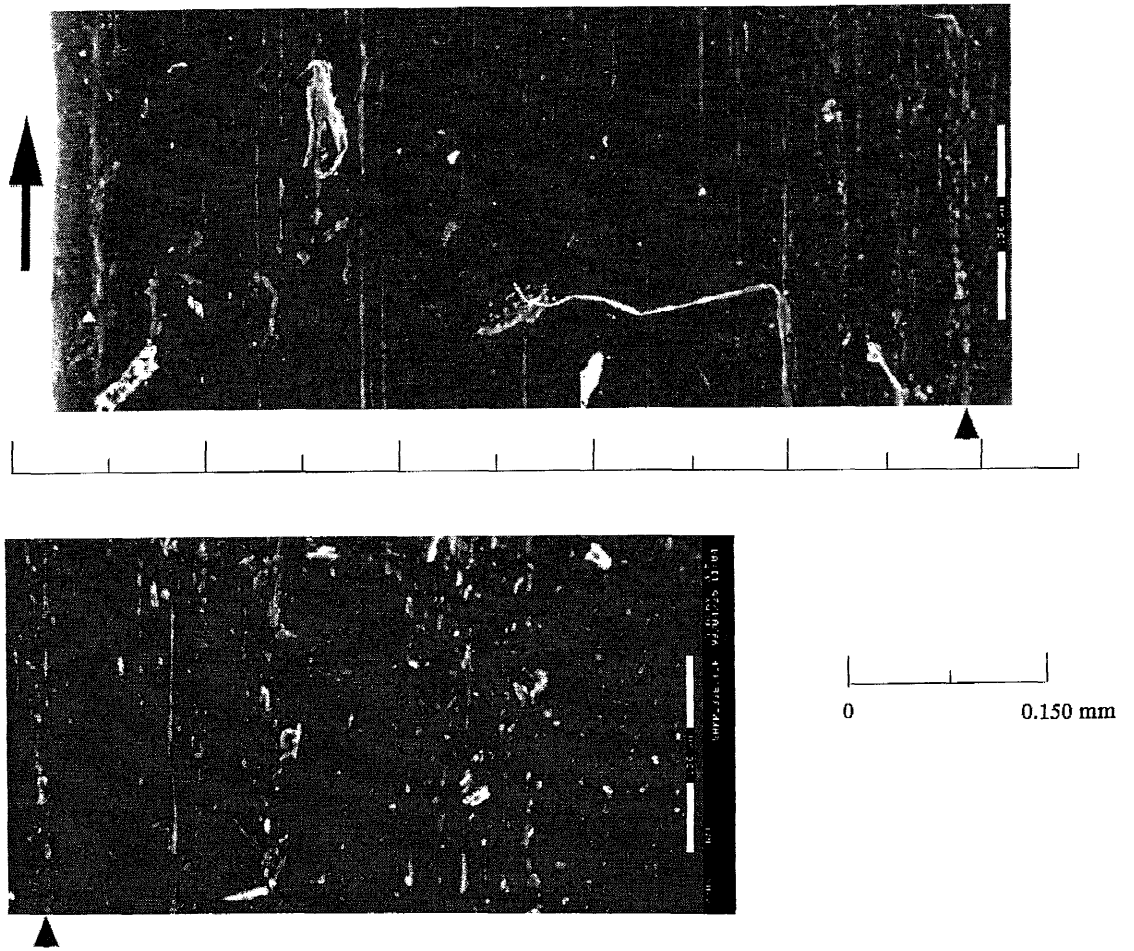

Figure 6.20 A SEM micrograph of injection molded PET/LCP (95/5 wt %) blend at a mold temperature of 35.00 °C, a melt temperature of 304 °C, and an injection speed of 15 mm/s.

CHAPTER 7

MECHANICAL PROPERTIES OF PET/LCP BLENDS

7.1 General

The mechanical properties, among all the properties of plastic materials, are often the most important properties because virtually all service conditions and the majority of end-use applications involve some degree of mechanical loading. In product design, material selection for a variety of applications is quite often based on mechanical properties such as modulus, strength, and elongation.

In this chapter, we discuss the variation of modulus, strength, and elongation at break of injection molded PET/LCP blends as a function of injection speed, melt temperature, and mold temperature. The effect of LCP concentration on modulus, strength, and elongation at break is also discussed. The efficacy of the new method to calculate modulus of the blends developed in this study is demonstrated by comparing the predictions of the new method against the experimental data presented in this Chapter.

7.2 Tensile Modulus of PET/LCP Blends

7.2.1 Effect of Injection Speed on Tensile Modulus

Figure 7.1 shows the effect of injection speed on the tensile modulus of injection molded PET/LCP (85/15 wt %) at a melt temperature of 304 °C. As seen, at a mold temperature of approximately 18 °C , the tensile modulus was found to change from about 4.6±0.06

GPa to 4.3±0.05 GPa when the injection speeds change from approximately 13 to 21 mm/s. At a mold temperature of 35 °C, the tensile modulus drops from approximately 4.5±0.07 GPa to 4.2±0.07 GPa with the injection speeds changing from approximately 13 to 21 mm/s. The tensile modulus decreases by approximately 5 % - 6 % in both cases, while the injection speed changes by about 40 %. Figure 7.2 shows the change of tensile modulus of the blend with the injection speed at a melt temperature of 320 °C. For three different mold temperatures shown, the tensile modulus decreases from approximately 4 % - 5 % with an increase of injection speed from approximately 13 to 21 mm/s.

Of course, the relative variation in tensile modulus of the blend with injection speed could be related to the morphology development of the blend. As discussed in Chapter 6, the thickness of the skin layer drops with an increase of injection speed (Figure 6.6). The trend of variation in the thickness with injection speed is reflected in the change of the tensile modulus. Another reason that the tensile modulus varies with injection speed could be found from the relationship between injection speed and the elongational strain or aspect ratio of the LCP fibers (see Figures 5.16 and 5.19a). LCP fibers with large aspect ratio have high modulus (see Figure 5.20). Clearly, the tensile modulus of the blends is sensitive to injection speed, and large tensile modulus can be obtained at low injection speeds. We used lower injection speeds than those shown in the figures, but this has resulted in short shot during the injection molding. Obviously, we can not decrease the injection speed unlimitedly in order to obtain large tensile modulus.

In Figures 7.1 and 7.2, the straight lines are the predictions of numerical calculations at various processing conditions, based on Eq. 5.31. It can be seen that

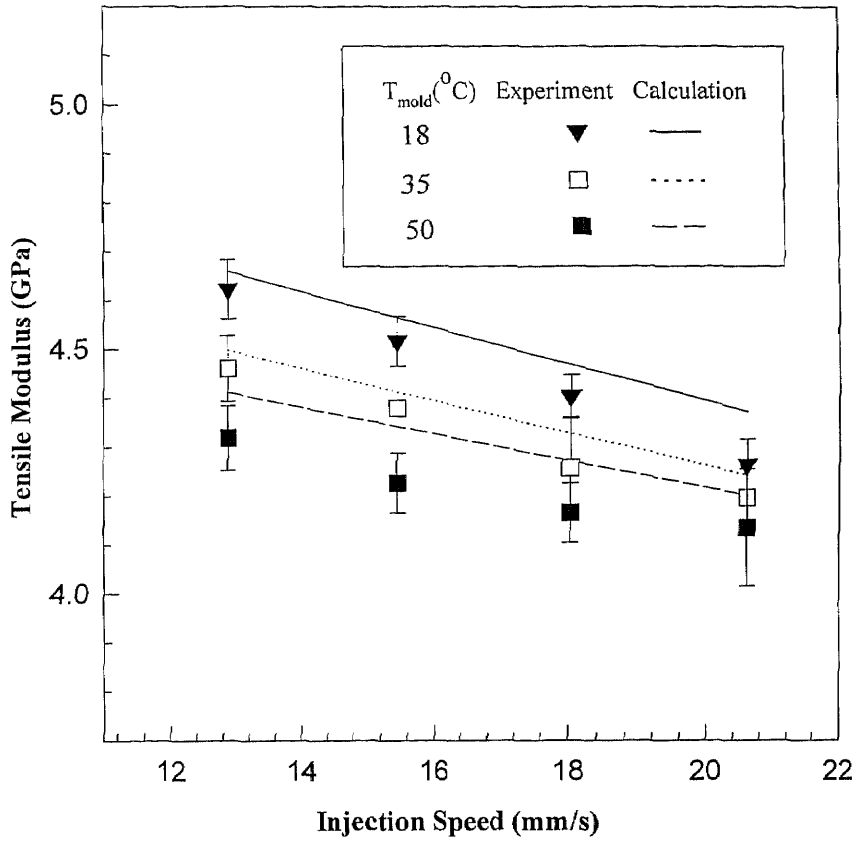

Figure 7.1 Tensile modulus of PET/LCP (85/15 wt %) blend vs. injection speed at a melt temperature of 304 °C. The data are shown with ±1δ.

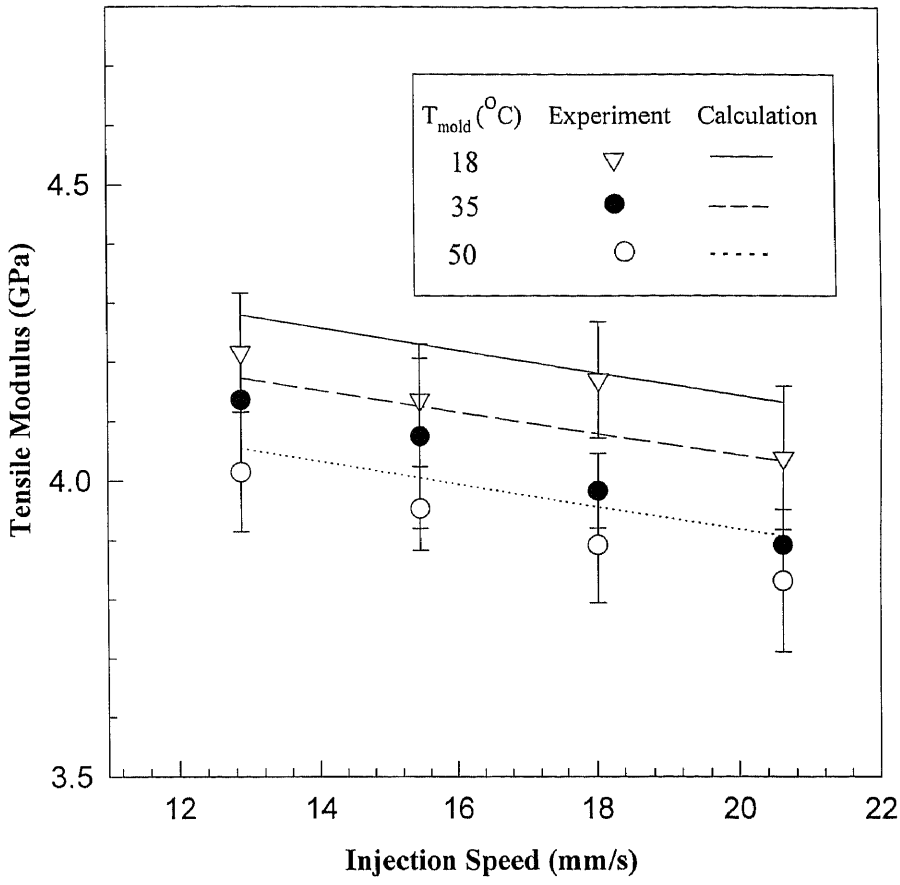

Figure 7.2 Tensile modulus of PET/LCP (85/15 wt %) blend vs. injection speed at a melt temperature of 320 °C. The data are shown with ±1δ.

calculated results show the same trend between injection speed and tensile modulus as the experimental data. At low injection speeds, much stiffer materials are obtained. From the comparison of the calculated results with the experimental data, we found that a agreement between the predictions and experimental results was obtained. It is clear that our numerical calculation is an effective way to analyze the morphology development and to predict the tensile modulus of the injection molded PET/LCP blends.

The predictions and experimental results show that low injection speed is recommended for the blends in order to obtain large tensile modulus of the blends.

7.2.2 Effect of Mold Temperature on Tensile Modulus

Figures 7.1 and 7.2 also show the change of tensile modulus of PET/LCP (85/15 wt %) blend with mold temperature. At a melt temperature of 304 °C (see Figure 7.1), the mold temperature was changed from approximately 18 °C to 50 °C. At low mold temperature, large tensile modulus of the blend was obtained and the maximum tensile modulus is 4.6±0.06 GPa at an injection speed of approximately 13 mm/s. The larger change of the tensile modulus takes place by varying mold temperature at low injection speeds than at high injection speeds. The tensile modulus almost decreases by 6.5 % at lower injection speeds while the mold temperature increases from approximately 18 °C to 50 °C. About 3.5 % change in the tensile modulus exists at high injection speeds while changing the mold temperature from approximately 18 °C to 50 °C.

At a melt temperature of 320 °C (see Figure 7.2), mold temperatures from approximately 18 °C to 50 °C were used during injection molding. The higher mold

temperatures were not used in this study because the samples could not be properly ejected from the mold cavity. As shown in Figure 7.2, a maximum tensile modulus, 4.2±0.07 GPa, occurs at a mold temperature of 18 °C and an injection speed of 13 mm/s; a minimum tensile modulus, 3.8±0.12 GPa, occurs at a mold temperature of 50 °C and an injection speed of 21 mm/s. Almost an 8.5 % drop in tensile modulus from maximum to minimum could be resulted if the injection speed and mold temperature are changed at the same time.

The variation of tensile modulus of the PET/LCP blends as a function of mold temperature corresponds to the difference in the morphology of the blends (see Figures 6.15 and 6.16). At low mold temperature, thick skin layer was obtained and this results in a large tensile modulus of PET/LCP blends. Change of tensile modulus of the blend with the mold temperature could be explained by the relationship between the aspect ratio of LCP fibers and mold temperature (see Figure 5.19c), and by the relationship between the aspect ratio and the modulus of the LCP (see Figure 5.20).

As we can see from Figures 7.1 and 7.2, based on Eq. 5.31, the predictions for the effect of mold temperature on the tensile modulus of the PET/LCP blends agree with the experimental results, which show that the analytical method developed in this study could predict well the variation of the tensile modulus of the blends with mold temperature.

The above analytical and experimental results show that the tensile modulus of the blend is sensitive to mold temperature. We can conclude that it is possible to change mold temperature in order to get large tensile modulus values during injection molding of the blends. Low mold temperatures favor the high tensile modulus of the blends.

7.2.3 Effect of Melt Temperature on Tensile Modulus

Figure 7.3 presents the comparison of the tensile moduli of PET/LCP (85/15 wt %) blend at three different melt temperatures. At an injection speed of 13 mm/s, the tensile modulus drops from approximately 4.6±0.06 GPa to 4.2±0.07 GPa when the melt temperature increases from 304 °C to 320 °C, a decrease of almost 8.5%. At an injection speed of 15 mm/s, the tensile modulus changes from approximately 4.5±0.05 GPa to 4.1±0.005 GPa with melt temperature changing from 304 °C to 320 °C. Obviously, melt temperature affected significantly the tensile modulus of the blends. But as discussed in Chapter 6, the thickness of the skin layer changed only marginally while the melt temperature varied from 304 °C to 320 °C (see Figures 6.11 and 6.12). We also found that the effect of melt temperature on elongational strain and aspect ratio was not apparent (see Figures 5.17 and 5.19b). We measured the tensile modulus of pure PET samples produced at the melt temperatures of 304 °C and 320 °C, and it is shown that the tensile moduli of PET are about 2.9 GPa and 2.75 GPa, respectively, at those two melt temperatures. This means that the variation of tensile modulus of the blends with melt temperature could be possibly attributed to the change of tensile modulus of the PET. Based on Eq. 5.31, we calculated the tensile modulus of PET/LCP blends using different values of PET moduli under different melt temperatures and found that the predictions show a fair agreement with experimental results (see Figure 7.3). We kept the tensile modulus of the pure PET constant in our calculations and found almost no change in the tensile modulus of the blends. Loss of tensile modulus of the pure PET at high melt temperature may have resulted from the degradation of the PET at high melt temperature.

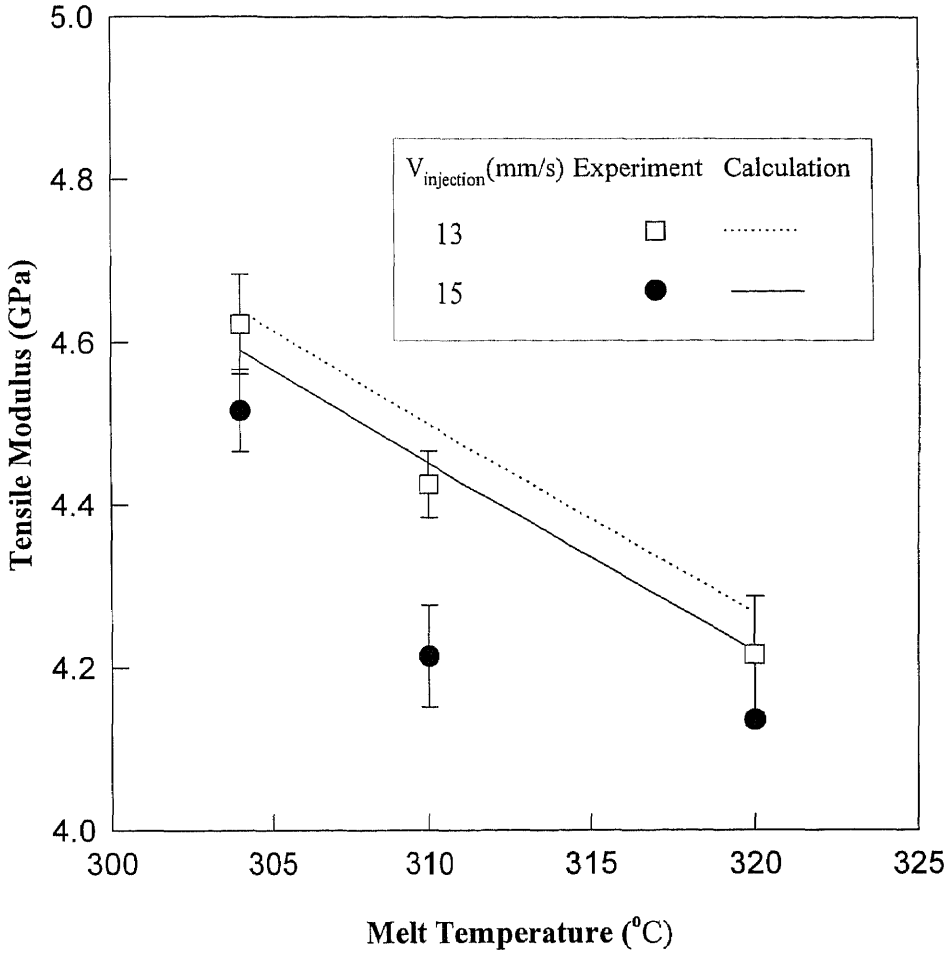

Figure 7.3 Tensile modulus of PET/LCP (85/15 wt %) blend vs. melt temperature at a mold temperature of 18 °C. The data are shown with ±1δ.

We used lower melt temperature than 304 °C and found unmelted LCP on the part surface. It was also difficult to eject molded samples at low melt temperature.

The predictions, based on Eq. 5.31, and experimental data show that the tensile modulus of the injection molded PET/LCP blends is affected only marginally by changing melt temperature. Thus, it is not recommended to change melt temperature in order to improve the tensile modulus of the blends.

7.2.4 Effect of LCP Content on Tensile Modulus

The tensile moduli of PET/LCP blends are shown in Figures 7.4 - 7.7, as a function of the LCP content. The tensile modulus of the blends is slightly influenced by the presence of 5 % LCP; it is almost equal to the tensile modulus of pure PET. Many other studies (Heino et al. 1992, Siegmann et al. 1985, Roetting et al. 1994) also reported similar results. This is because the amount of LCP is too small and cannot dominate the formation of the fibrous structure and increase of the tensile modulus of PET/LCP blends during the injection molding. By increasing the LCP content up to 15 %, the tensile modulus of the blends shows a big jump to 4 GPa from 3 GPa. The tensile modulus was found to undergo a 1.8-fold increase by addition of 25 % of LCP, as reported by La Mantia (1993), and Siegamn et al. (1985).

As we can see from these Figures, the effect of injection speed on tensile modulus for different LCP contents is different. While injection speed varied from maximum to minimum, the tensile modulus of PET/5% LCP blends was changed by 4 % but the tensile modulus of PET/25% LCP blends increased by 10 %. This is due to the wide range of the morphologies obtained at high LCP concentrations.

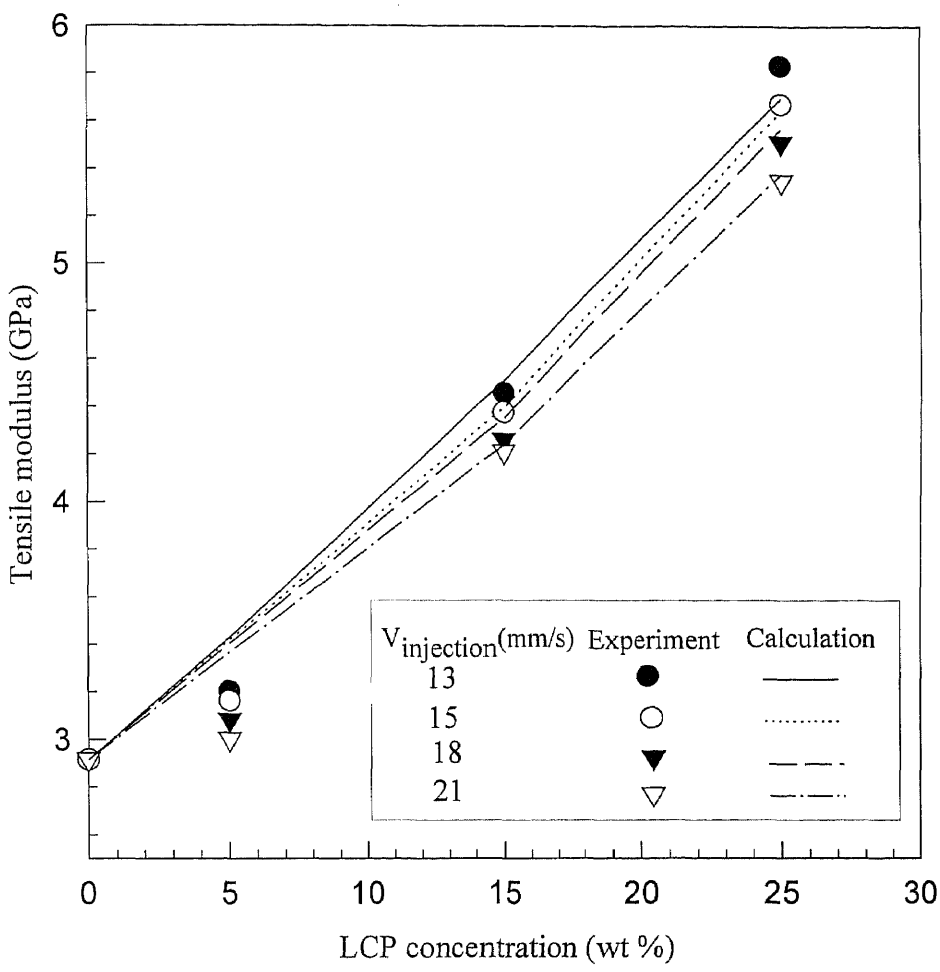

Figure 7.4 Tensile modulus of PET/LCP blends vs. LCP concentration at a melt temperature of 304 °C and a mold temperature of 35 °C. The standard deviations for all four points for the 5% LCP content range from 0.03 to 0.12 GPa; for the 15% from 0.0 to 0.10 GPa; for the 25% from 0.0 to 0.16 GPa.

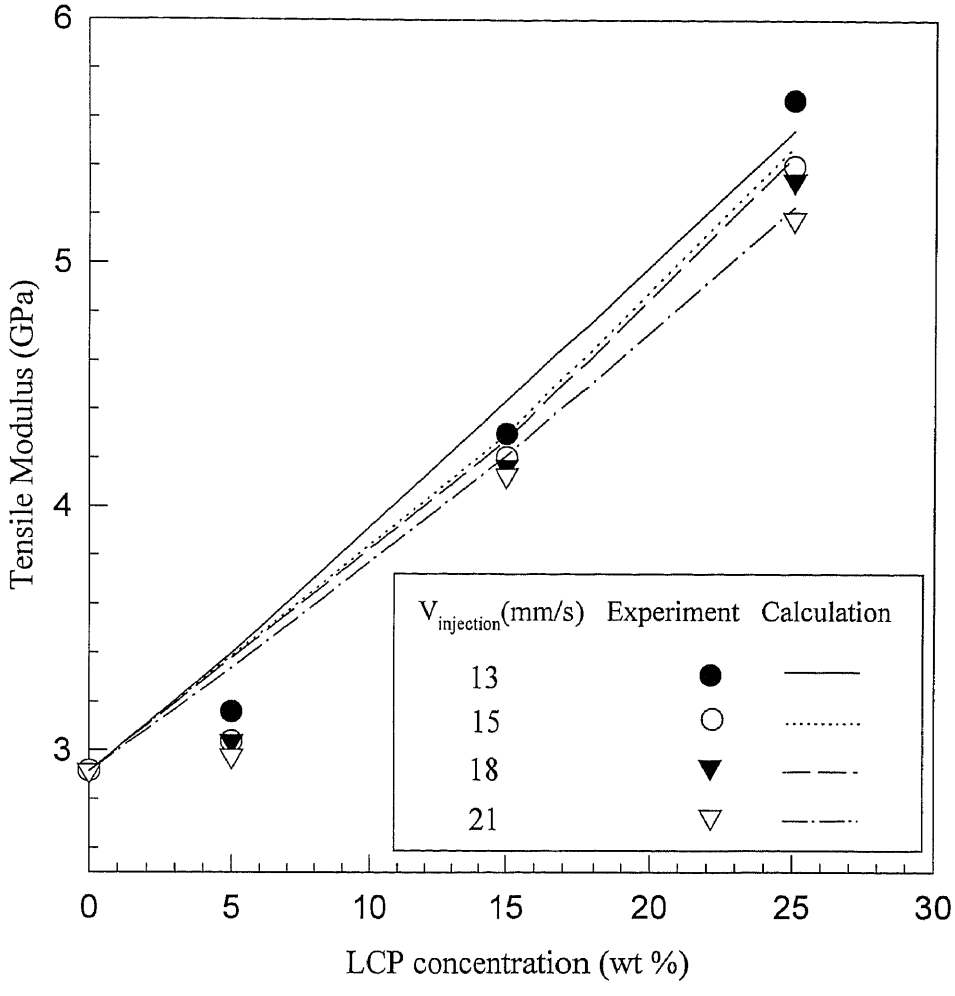

Figure 7.5 Tensile modulus of PET/LCP blend vs. LCP content at a melt temperature of 304 °C and a mold temperature of 50 °C. The standard deviations for all four points for the 5% LCP content range from 0.0 to 0.07 GPa; for the 15% from 0.06 to 0.12 GPa; for the 25% from 0.09 to 0.16 GPa.

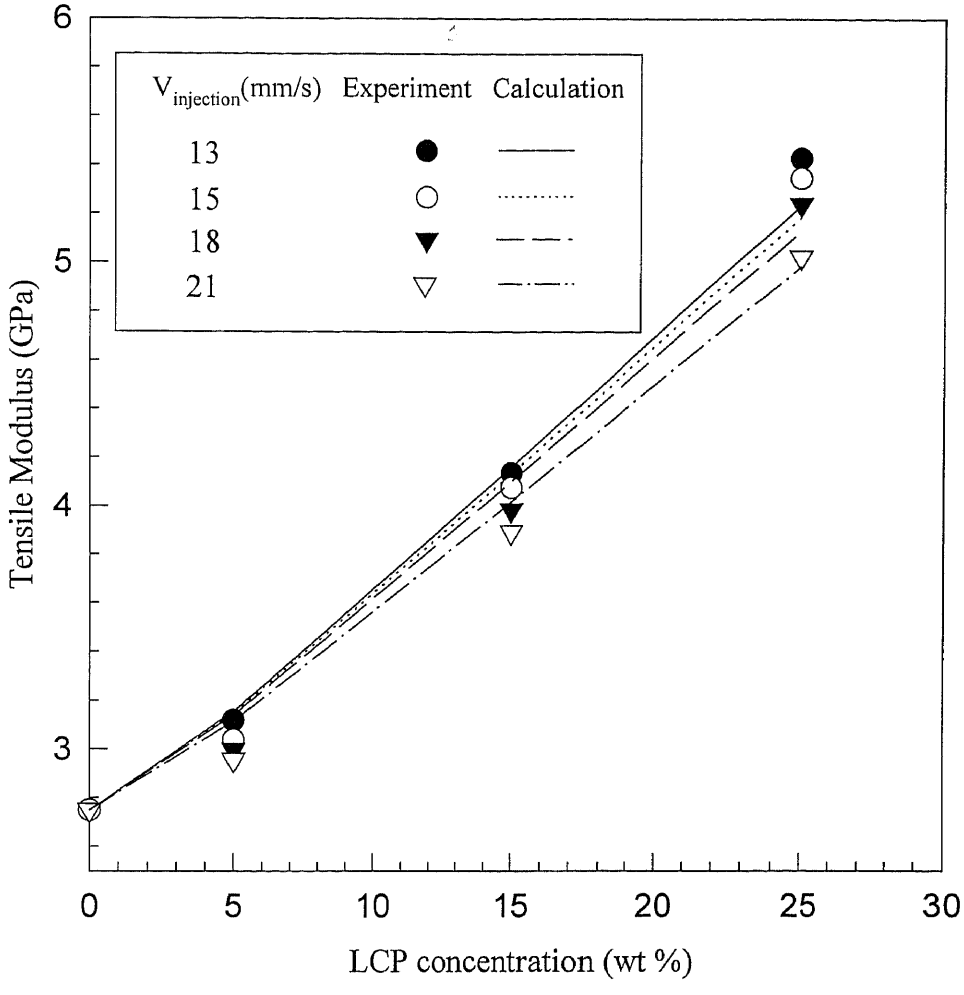

Figure 7.6 Tensile modulus of PET/LCP blends vs. LCP concentration at a mold temperature of 35 °C and a melt temperature of 320 °C. The standard deviations for all four points for the 5% LCP content range from 0.0 to 0.07 GPa; for the 15% from 0.0 to 0.15 GPa; for the 25% from 0.0 to 0.06 GPa.

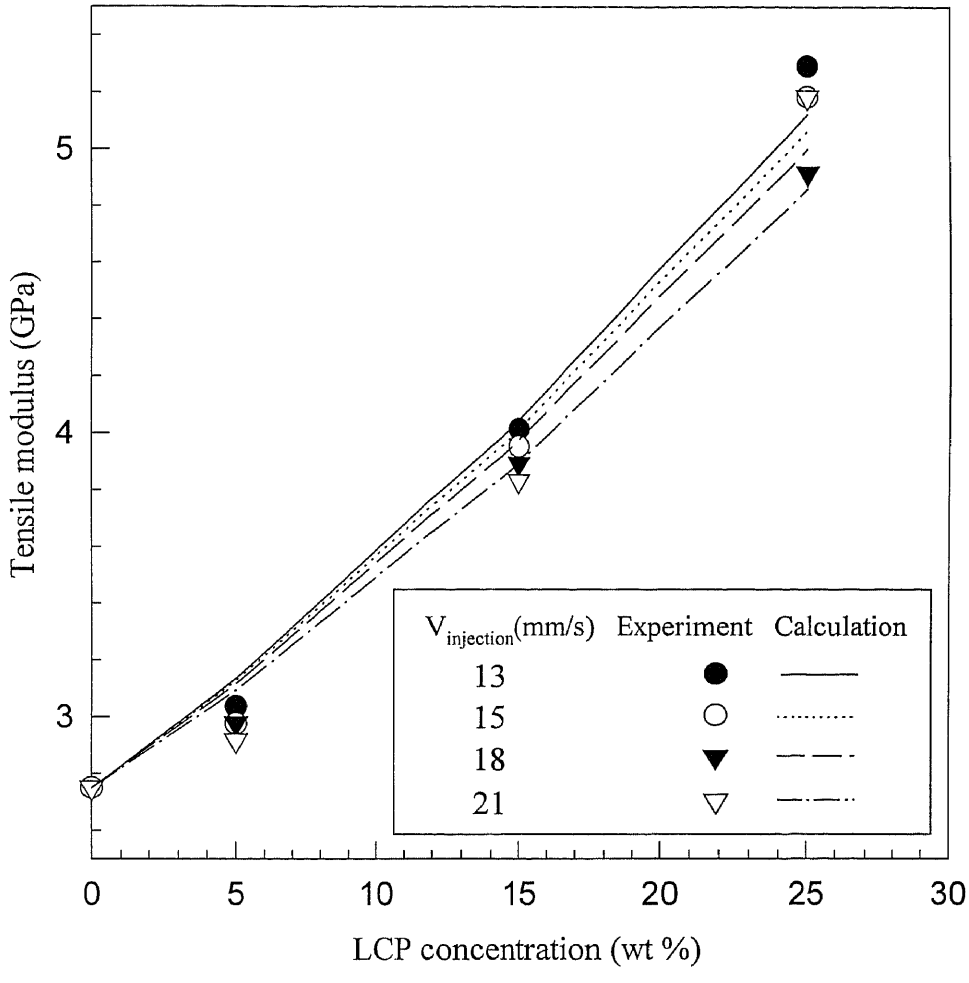

Figure 7.7 Tensile modulus of PET/LCP blends Vs LCP concentration at a melt temperature of 320 °C and a mold temperature of 50 °C. The standard deviations for all four points for the 5% LCP content range from 0.0 to 0.08 GPa; for the 15% from 0.07 to 0.12 GPa; for the 25% from 0.0 to 0.18 GPa.

Comparing the predictions (lines), based on Eq. 5.31, and experimental data (symbols), a good agreement between them was obtained. It is shown that our predictions of the distribution in the LCP fiber size and LCP modulus are reasonable. In earlier studies (Li et al. 1992, Shin et al. 1992, Kyolani et al. 1992), the correct estimations of the aspect ratio of the LCP fibers and their tensile modulus were made with difficulties when calculating the tensile modulus of the LCP blends using traditional composite model. A reasonably accurate approach to estimate the aspect ratio and the modulus has been developed in this study.

7.3 Strength of PET/LCP Blends

Figures 7.8 and 7.9 present the effect of injection speed on the stress at break of PET/LCP (85/15 wt %) blends. As can be seen, there is no consistent relationship between the stress at break and the injection speed. But higher stress at break of the blends tend to occur at lower injection speeds at high melt temperature. From Figures 7.8 and 7.9, it is found that the stress at break of the blends is not sensitive to mold temperature.

Figure 7.10 shows the influence of melt temperature on the stress at break of PET/LCP (85/15 wt %) blends. There is a big jump in the breaking stress of the blends as the melt temperature changed from 320 °C to 304 °C. At the melt temperature of 304 °C, the stress at break of the blends ranges from 155±5 MPa to 175±2 MPa; at the melt temperature of 320 °C, it varies from 138±4 MPa to 141±3 MPa. The change of 18 % in the breaking stress is obtained when the melt temperature drops from 320 °C to 304 °C.

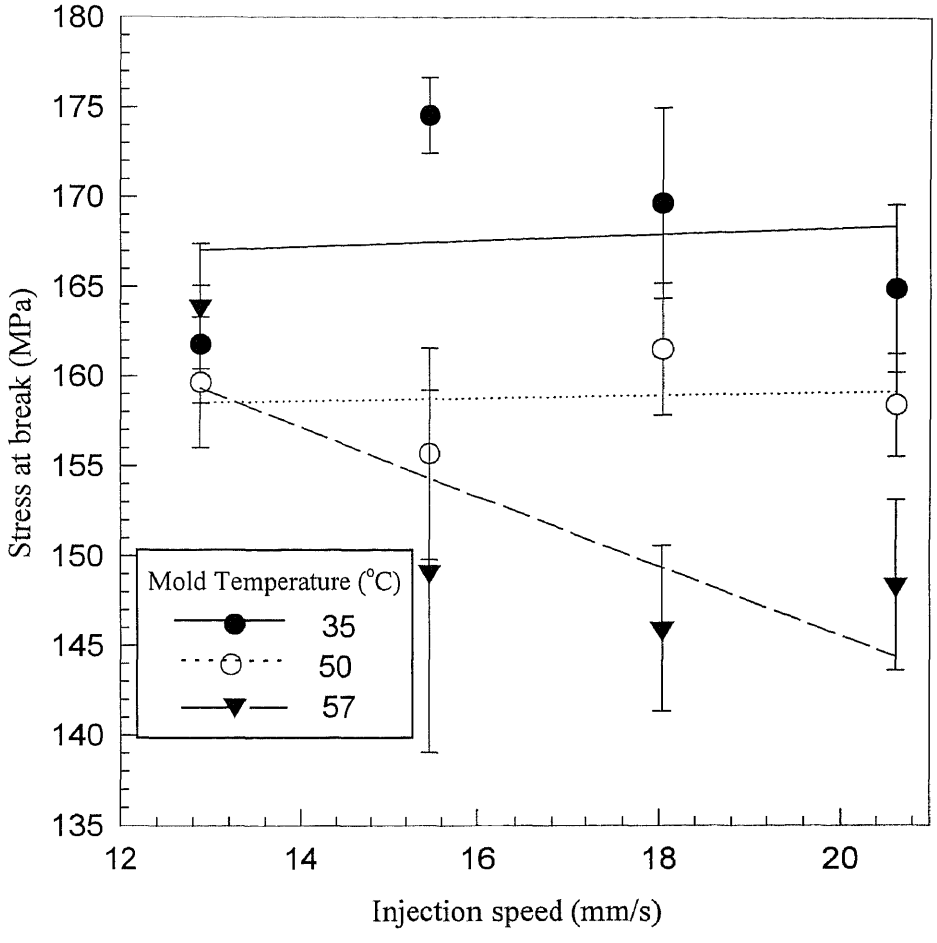

Figure 7.8 Tensile stress at break of PET/LCP (85/15 wt %) blend vs. injection speed at different mold temperatures and a melt temperature of 304 °C. The data are shown with ±1δ.

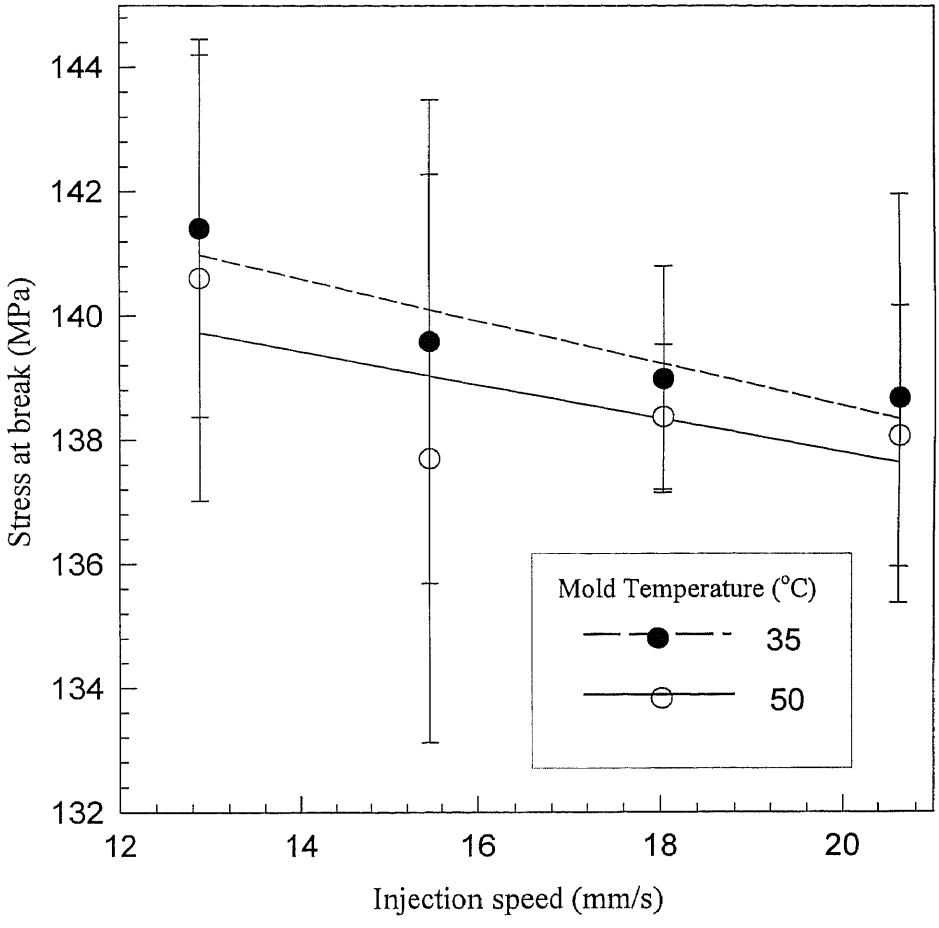

Figure 7.9 Tensile stress at break of PET/LCP (85/15 wt %) blend vs. injection speed at different mold temperatures and a melt temperature of 320 °C. The data are shown with ±1δ.

Comparing the effects of injection speed, melt temperature and mold temperature on the strength of PET/LCP blend, it is shown that changing the melt temperature is a more effective way to change the breaking stress than varying injection speed or mold temperature. Obviously, the variation of the breaking stress of the blends as a function of injection speed, melt temperature, and mold temperature is due to the formation of LCP fibers in the blends. But the strength is very sensitive to the adhesion between the components of PET/LCP blends, and thus its behavior may change with the interfacial adhesion as many studies pointed out (Beery et al. 1991, Siebman et al. 1985). The big increase of strength of the blends with melt temperature could be explained by the fact that interfacial adhesion is more sensitive to melt temperature than to mold temperature and injection speed. This is because a poor adhesion between the matrix and the fibers of the blends could result in a decrease of strength of the blends. But further studies are required to confirm this hypothesis. Any crystallization in pure PET under present experimental conditions was not found because all PET simples produced in this study are transparent. Thus, the effect of the crystallization on the strength of the blends could be ignored.

Figures 7.11 and 7.12 show the stress at break of PET/LCP blends as a function of the LCP content. In both cases, the breaking stress increases by 100% with the addition of 25% LCP and the maximum stress at break reaches above 200 MPa compared with the strength of 100 MPa of pure PET. Therefore, it is a very effective method to use LCP to enhance the strength of flexible thermoplastics. From Figures 7.11 and 7.12, it is also found a big change of the stress at break of PET/25% LCP blend with melt temperature.

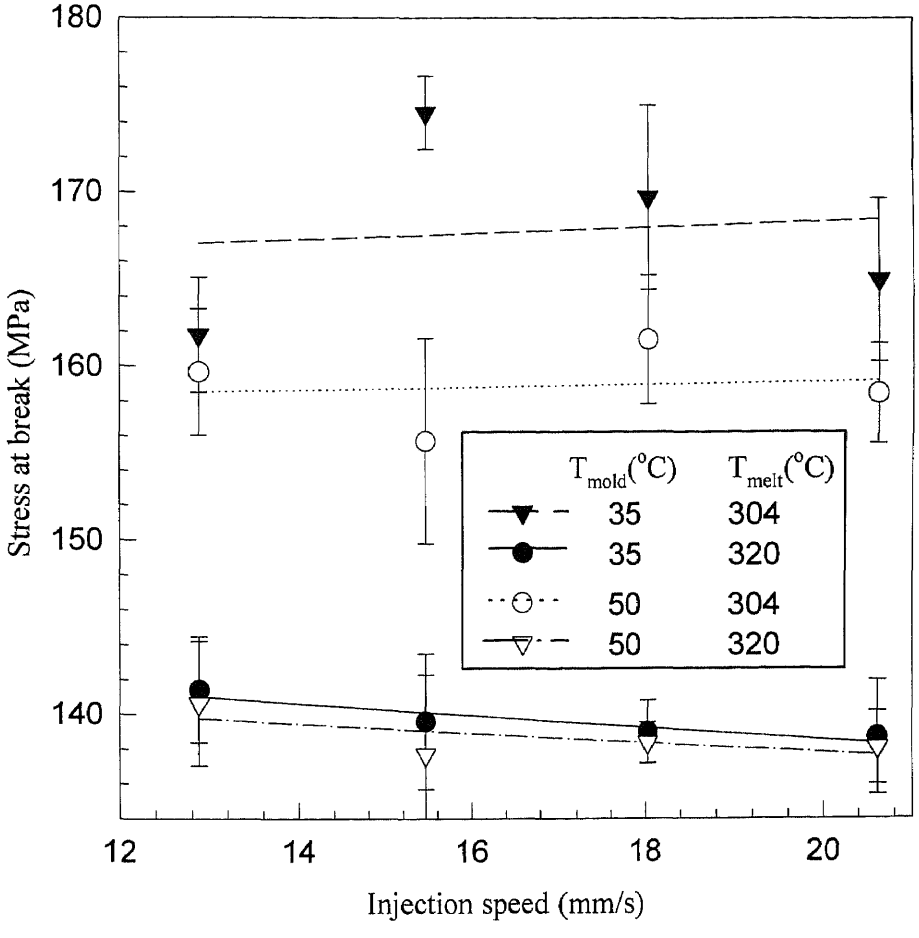

Figure 7.10 Effect of melt temperature on tensile stress at break of PET/LCP (85/15 wt %) blend. The data are shown with ±1δ.

There is almost no variation in the stress at break for PET/5% LCP blend as a function of injection speed, mold temperature, and melt temperature. We can conclude that changing the injection conditions does not result in improvement of mechanical properties of PET/LCP blends at low weight fraction of the LCP .

7.4 Elongation at Break of PET/LCP Blends

Figures 7.13 and 7.14 depict the elongation at break of PET/15 percent LCP blends with respect to injection speed. We cannot see any relationship between the elongation at break and injection speed. The elongation at break of the blends changes from 5.5%±0.2% to 6.6%±0.1%. We also examined the variation of elongation at break as a function of mold temperature but did not see any relationship between them. Comparing Figures 7.13 and 7.14, we also did not obtain a simple relationship between elongation at break and melt temperature. At a melt temperature of 304 °C (Figure 7.13), the elongation at break of the blends varies in a range from 5.5%±0.2% to 6.6%±0.1%; at a melt temperature of 320 °C (Figure 7.14), the maximum and the minimum elongation at break are 6.1%±0.2% and 5.6%±0.3%, respectively. The non-consistent relationship between elongation at break and injection molding conditions can not be explained using our experimental results.

The effect of LCP content on the elongation at break of PET/LCP blends is shown in Figures 7.15 and 7.16. During the measurement of the elongation of pure PET, we cannot see the breaking point of the PET even though the elongation of the PET sample reached 1/3 of original length of the sample. For PET/LCP blends, clear breaking point

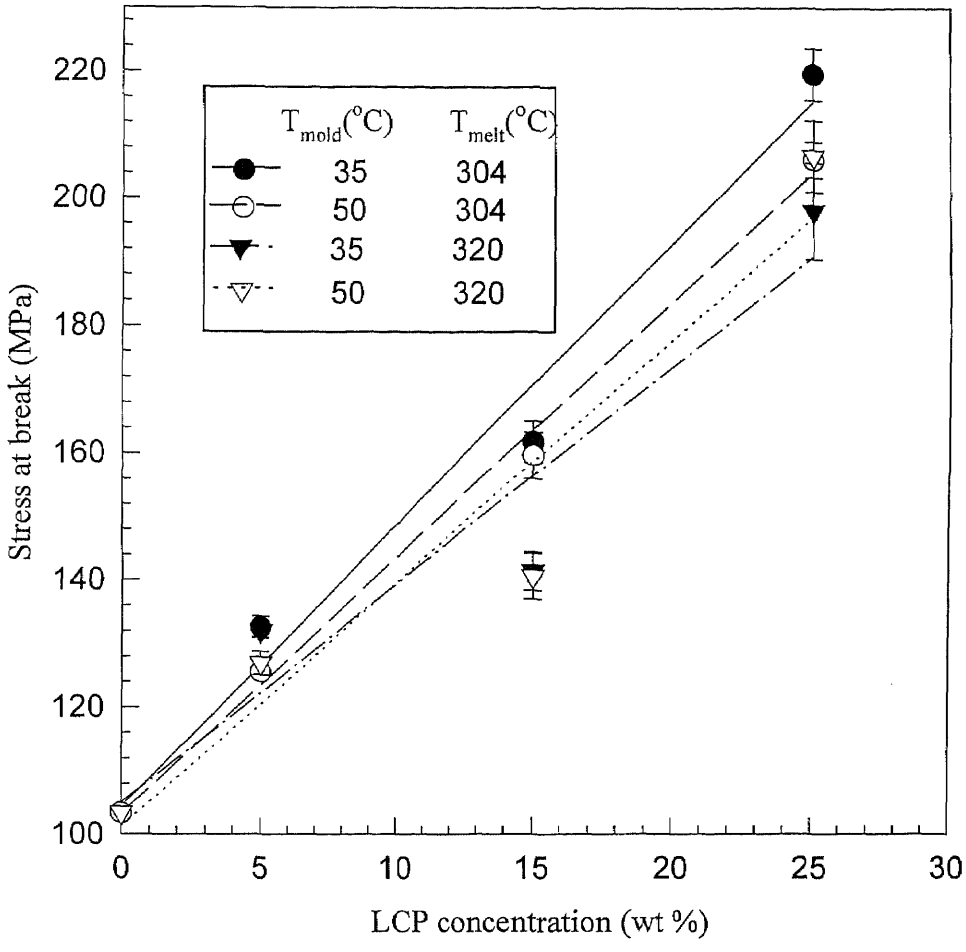

Figure 7.11 Effects of LCP content, melt, and mold temperatures on tensile stress at break of PET/LCP blends at an injection speed of 13 mm/s. The data are shown with ±1δ.

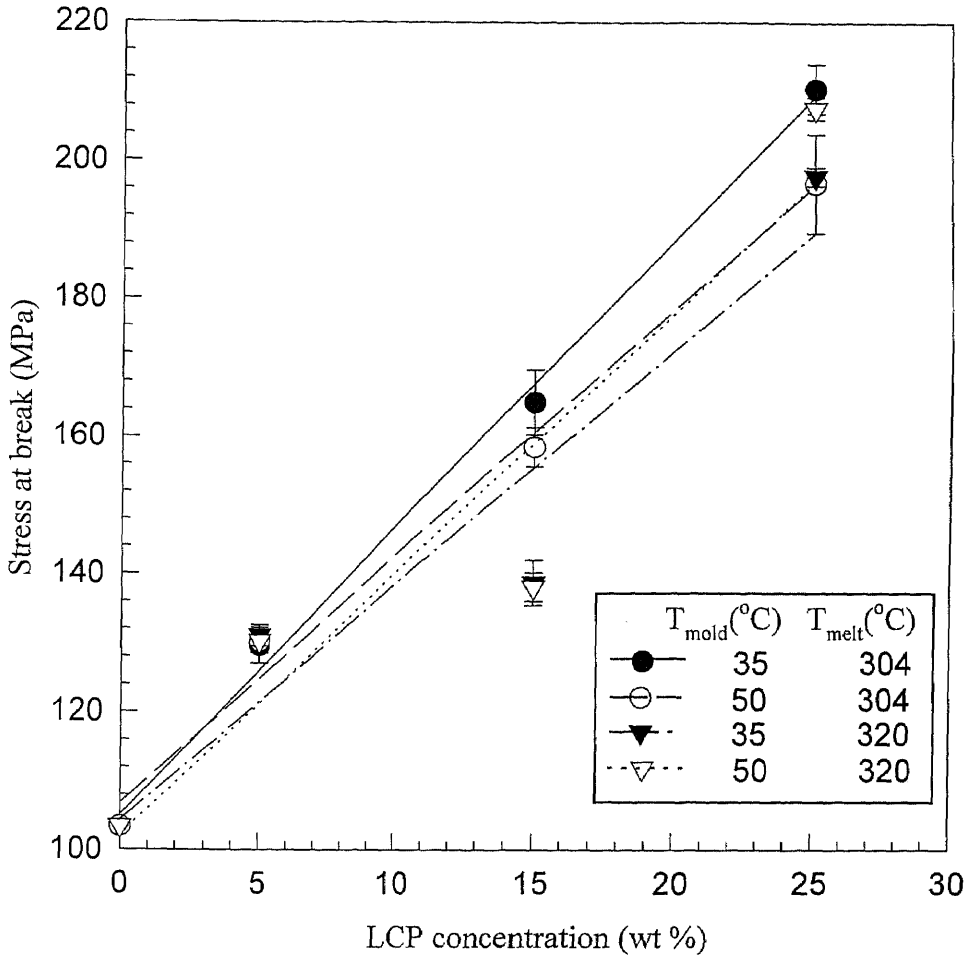

Figure 7.12 Effects of LCP content, melt, and mold temperatures on tensile stress at break of PET/LCP blends at an injection speed 21 mm/s. The data are shown with ±1δ.

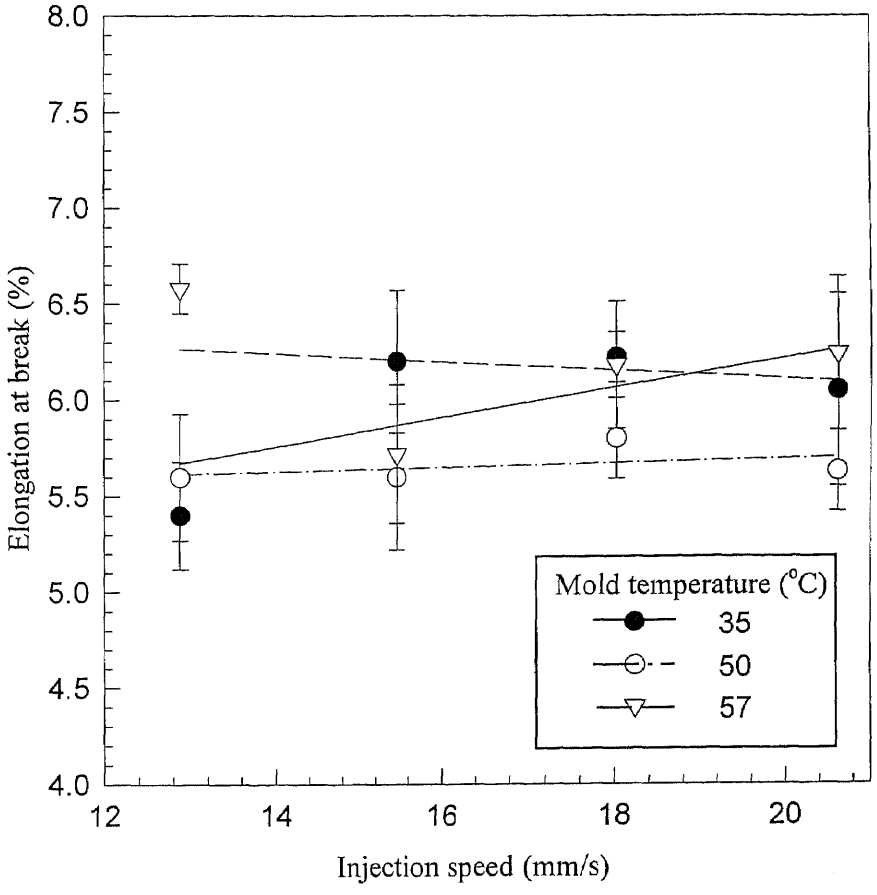

Figure 7.13 Elongation at break of PET/LCP (85/15 wt %) blend vs. injection speed at different mold temperatures and a melt temperature of 304 °C. The data are shown with ±1δ.

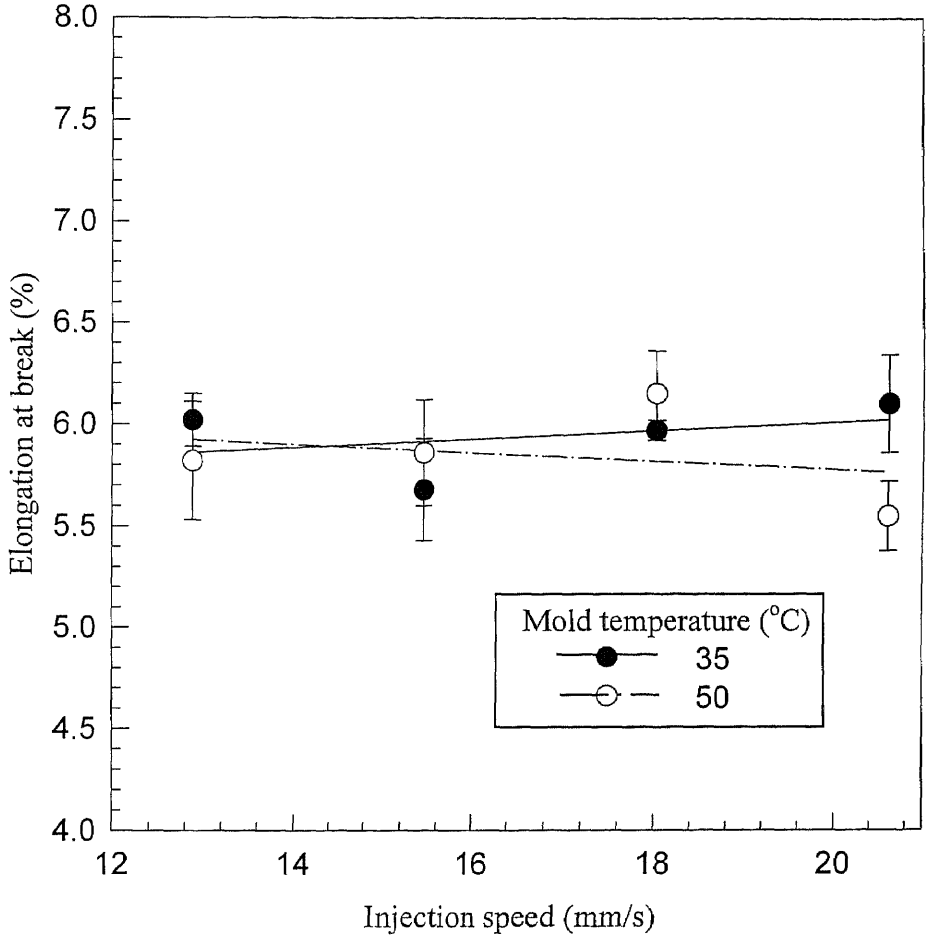

Figure 7.14 Elongation at break of PET/LCP (85/15 wt %) blend vs. injection speed at different mold temperatures and a melt temperature of 320 °C. The data are shown with ±1δ.

can be observed. Therefore, we only present the elongation at break of PET/LCP blends at three different LCP concentrations in this study in order to see the effect of the LCP content on the elongation at break. As seen, there is no significant change of the elongation at break while the LCP content increases from 15 % to 25 %, similar to the results of Kulichikin et al. (1991), and the value of the elongation at break for the two LCP contents varies around 5.9%; the elongation at break of the blends sharply drops while the LCP content increases from 5 % to 15 %. It is shown that high elongation from PET matrix is totally destroyed by the addition of large weight fraction of LCP. The LCP becomes gradually the main factor influencing the elongation of the blends as the LCP content increases to 15 %. An increase in LCP content ensures that there are more LCP fibers to form at large LCP weight fraction.

From Figures 7.15 and 7.16, it is also found that it is difficult to relate the elongation at break of PET/LCP blends to injection molding parameters for all the LCP concentrations used.

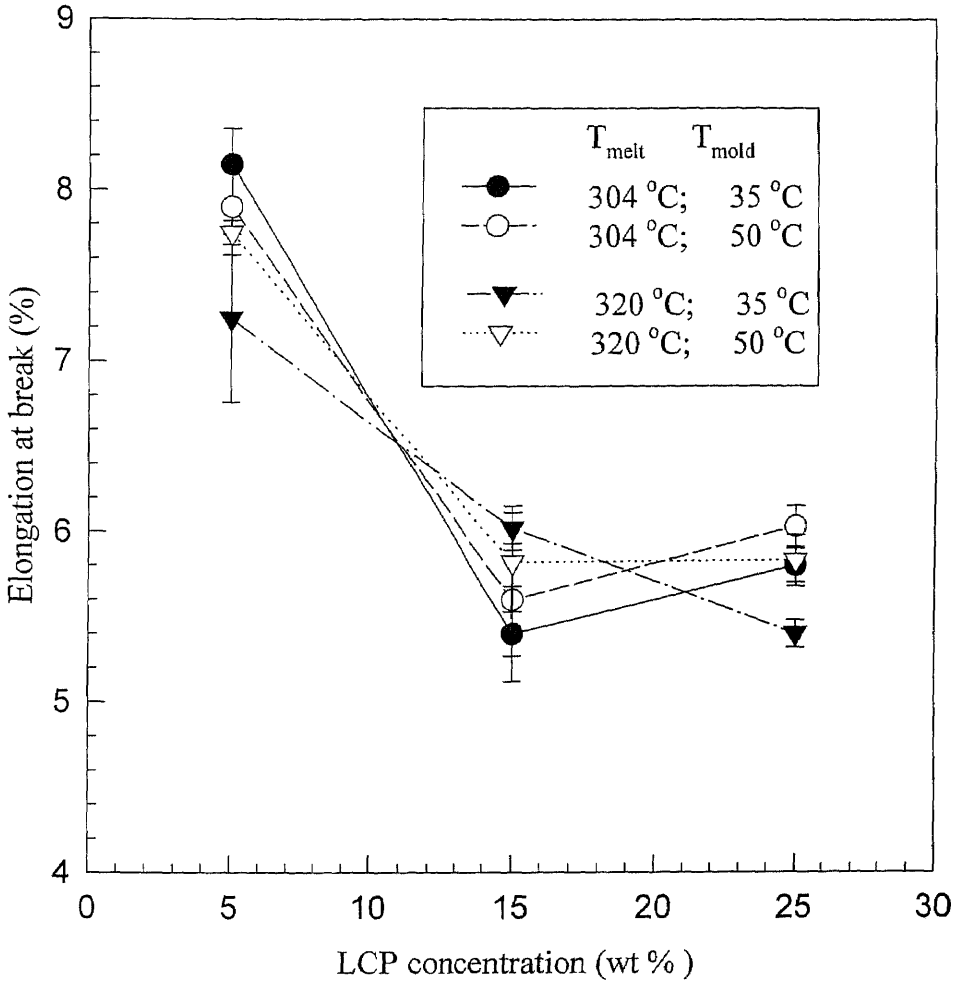

Figure 7.15 Elongation at break vs. LCP content at different melt and mold temperatures and at an injection speed of 13 mm/s. The data are shown with ±1δ.

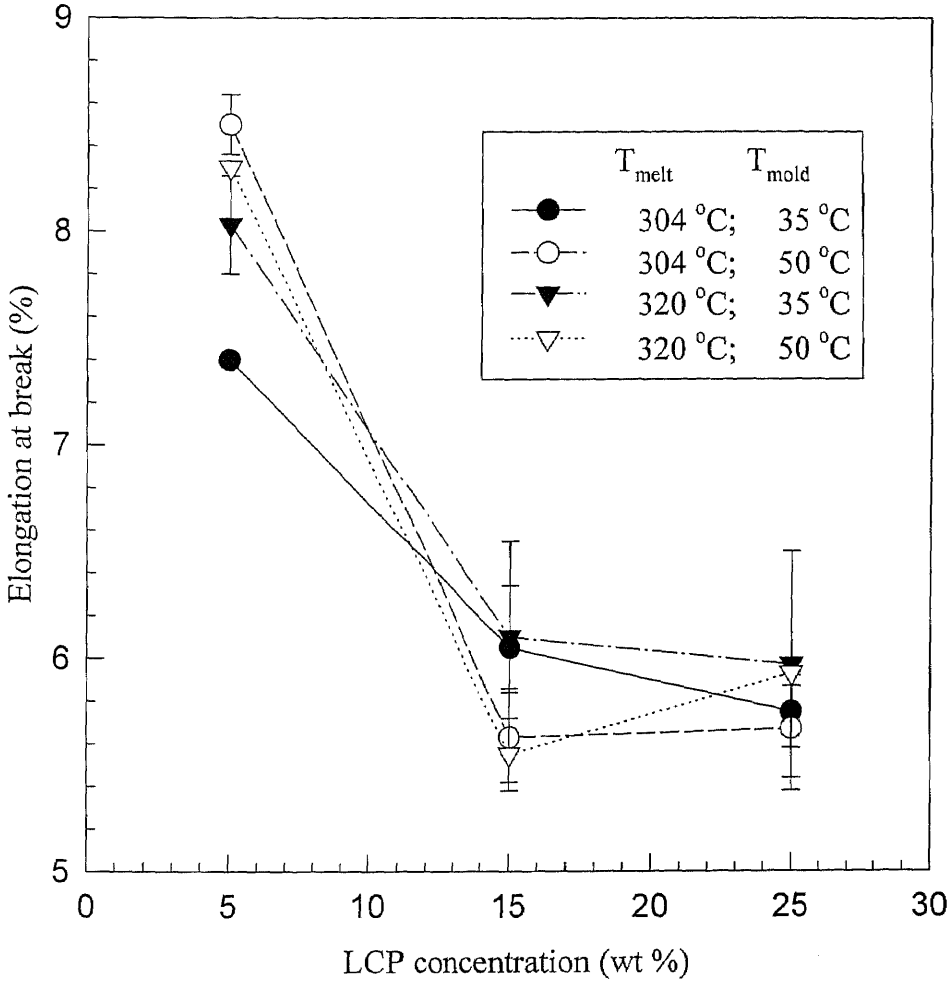

Figure 7.16 Elongation at break vs. LCP content at different melt and mold temperatures and at an injection speed of 21 mm/s. The data are shown with ±1δ.

CHAPTER 8

CONCLUSIONS AND FUTURE WORK

In this study, a series of experiments was set up in order to analyze the morphology and mechanical properties of injection molded PET/LCP blends, including the manufacture of the samples for measurement of mechanical properties, the preparation of the samples for morphology analysis, measurement of rheological and mechanical properties, and morphological observation and analysis using scanning electronic microscope (SEM) and optical microscope (OM). Simulations of the injection molded parts at various processing conditions were performed using CMOLD. Velocity profiles across the thickness of the mold cavity were obtained. A simple analytical method to calculate the melt flow in the advancing melt front (AMF) region was developed. By combining the simulations of injection molding and analysis of the flow in the AMF region, velocity vectors and elongation strain in the AMF region at various processing conditions were obtained.

8.1 Conclusions

Based on these experimental results and analytical methods mentioned above, the relationships between the structure and mechanical properties of the injection molded PET/LCP blends, between the processing parameters, properties, and structure, have been investigated. The studies have led to the following conclusions:

1. According to the simulations of the injection molded parts at various processing condition, it was found that the effect of the processing conditions on the velocity

profiles is very significant: the effect of melt temperature on the velocity focuses on the center area of the mold cavity and the effect of mold temperature on the area away from the center of the mold cavity.

2. Based on the velocity vectors in the AMF region, the deformation of the LCP domains and the distribution of elongational strain across the thickness of the mold cavity were calculated. The theoretical predictions show that the elongational strain increases with decreasing injection speed and mold temperature, and the effect of melt temperature on the elongational strain is not distinct.
3. In the numerical analysis, the aspect ratio of the reinforcing LCP phase is correlated with the elongational strain by assuming an affine deformation scheme and a original spherical shape of the LCP domains. The calculations of the aspect ratio show that low mold temperatures and low injection speeds favor the formation of large aspect ratio LCP fibers. Melt temperature appears to have a little effect on the aspect ratio.
4. A new method to calculate the distribution of tensile modulus of injection molded PET/LCP blends across the thickness of the mold cavity was developed, based on the Halpin-Tsai composite model. Using this method, we were able to make a number of predictions about the effects of melt temperature, mold temperature, injection speed, and LCP volume fraction on the morphologies, and the moduli of the blends. Our predictions show that in order to optimize the reinforcement effect in the blends, low mold temperature and low injection speed are required, and further more, a distinct reinforcement of the blends will not be resulted by changing melt temperature .
5. Scanning electron and optical micrographs covering the half-thickness area of the injection molded samples were made. SEM and OM demonstrate the existence of

distinct morphological layers in the injection molded samples of PET/LCP blends. A skin layer and a core layer can be distinguished according to the shape (fiber or sphere) of the LCP domains. In the core layer, the LCP domains exist mainly in a spherical form. In the skin layer, fibril-like LCP domains are found. The skin layer can be subdivided into the topskin and subskin layers, and the former consists of very long LCP fibers, while the latter contains short LCP fibers. The diameters of the fibers are about 1.5 to 6.0 μm in the 15 % LCP blend. The distribution of the LCP fibers across the thickness of the mold cavity is well described by the prediction of numerical analysis. The thickness of the skin layer, one of the characteristics identified in the morphology of the blends was measured. Its magnitude ranged from approximately 0.40 to 0.62 mm in the 15 % LCP blends, dependent on the processing conditions.

6. We investigated the effect of injection molding parameters including melt temperature, mold temperature, and injection speed on the morphology of the PET/LCP blends. The morphology is very sensitive to mold temperature and injection speed, but not to melt temperature. The relationships between the morphology and processing parameters are in line with the predictions of theoretical analysis. The effect of the LCP content on the morphology of the blends was also investigated. At high LCP concentrations, the LCP fibers exist in the skin area and the skin layer is thicker.
7. The moduli of the injection molded PET/LCP blends at different processing parameters including melt temperature, mold temperature, and injection speed were

measured. It has been shown that the tensile modulus of the injection molded PET/LCP blends is very sensitive to the mold temperature and injection speed. The tensile modulus of the blends increases as the mold temperature and injection speed decrease. The effect of melt temperature on the modulus of the blends is not clear. The experimental results are in agreement with the theoretical predictions of the tensile modulus. A good agreement between them suggests that the tensile modulus of the PET/LCP blends can be improved by adjusting the injection speed and mold temperature. The theoretical predictions and experimental results also show that the variation of the tensile modulus as a function of injection molding parameters is related to the morphological development: high modulus exist at large aspect ratio of LCP fibers and thick skin layer. The LCP content can significantly influence the tensile modulus of the PET/LCP blends at above 5 wt % LCP.

8. The efficacy of the new method to calculate the modulus of injection molded PET/LCP blends is demonstrated by comparing the theoretical predictions and experimental results. The theoretical method incorporated the effect of processing parameters on the morphology and the modulus of the blends, and provides one with a reasonable approach to study the relationships between processing and properties for LCP blends.

9. No simple relationship between the strength of the injection molded PET/LCP blends and injection speed was observed. Melt temperature appears to have a distinct effect on the breaking stress. High stress at break can be obtained at low melt temperature. The stress at break is, approximately, linearly proportional to LCP concentration.

10. No consistent relationships between the elongation at break of the injection molded PET/LCP blends and injection speed, mold temperature, and melt temperature were obtained. As the LCP content increases, the elongation at break decreases but the variation of elongation at break is not significant at above 15 wt % LCP.

8.2 Future Work

1. The modulus of pure LCP fibers is basic data for studying mechanical properties of LCP blends. It is very important to develop a experiment method to measure the modulus of LCP fibers and then to find the relationships between the aspect ratio and modulus of LCP fibers.
2. A technique to measure the LCP fiber size in the matrix, and to determine the distribution across the thickness of the mold cavity should be developed, in order to confirm the theoretical predictions of morphology of LCP blends.
3. One method of experimentally measuring the effect of LCP fiber aspect ratio on the mechanical properties of LCP blends is to construct a mold with several inserts. Using these inserts one can prepare ASTM D368 standard specimens with several thickness ranging from 3 mm to 100 μm or less under identical processing conditions. We can compare the measured modulus versus thickness, with predictions.

APPENDIX A

FIGURES

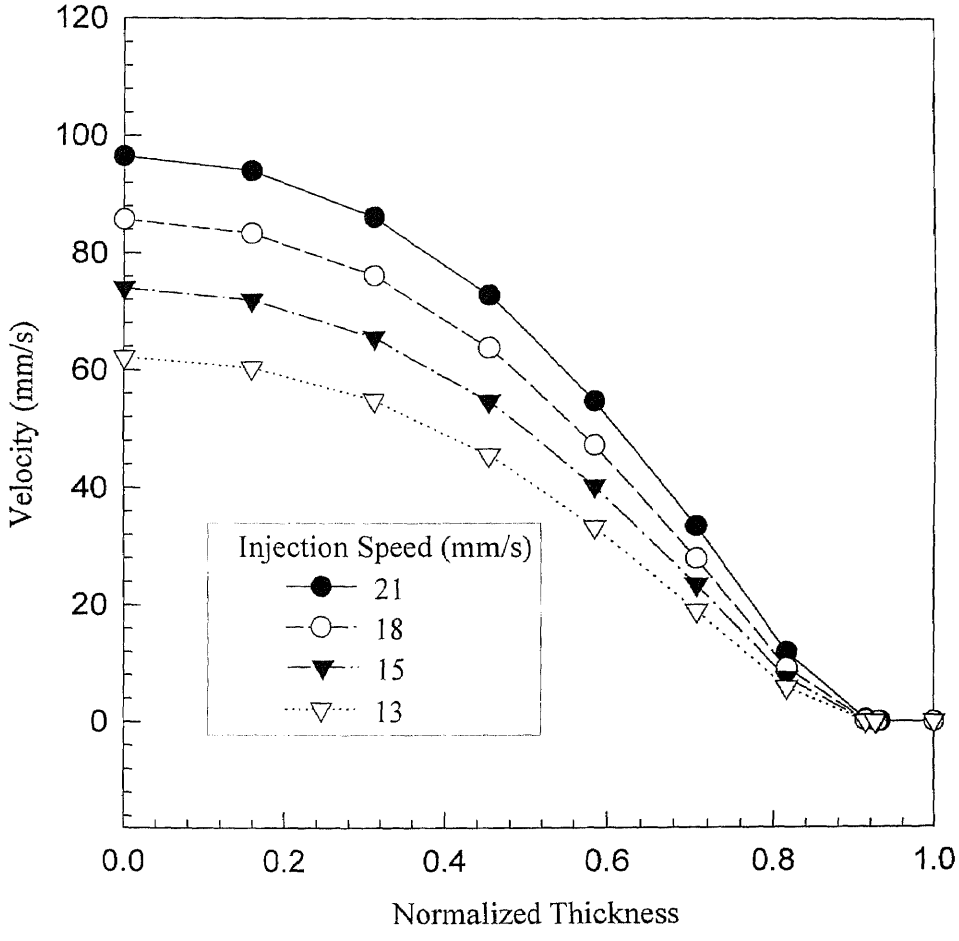

Figure A1 Velocity profiles behind the AMF at a melt temperature of 304 °C and a mold temperature of 18 °C for PET/LCP (85/15 wt %) blend. 0.0 is the center of mold cavity and 1.0 is the mold wall.

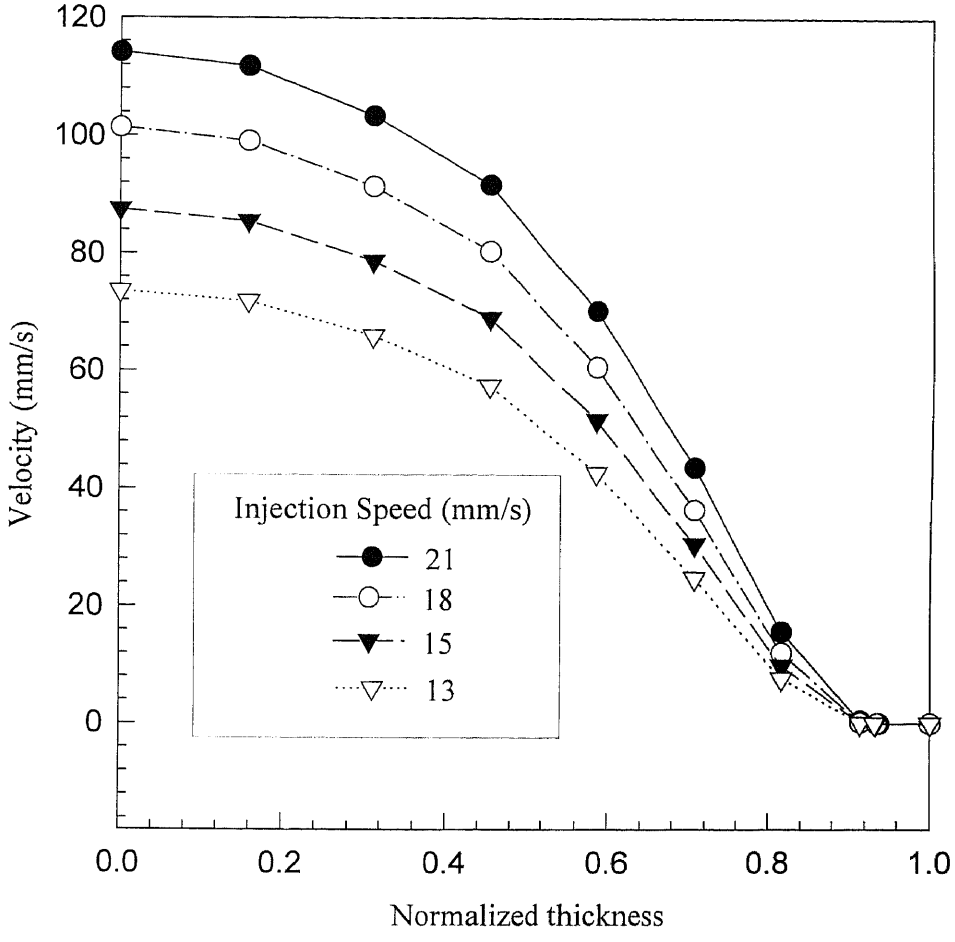

Figure A2 Velocity profiles behind the AMF at a melt temperature of 320 °C and a mold temperature of 35 °C for PET/LCP (85/15 wt %) blend. 0.0 is the center of mold cavity and 1.0 is the mold wall.

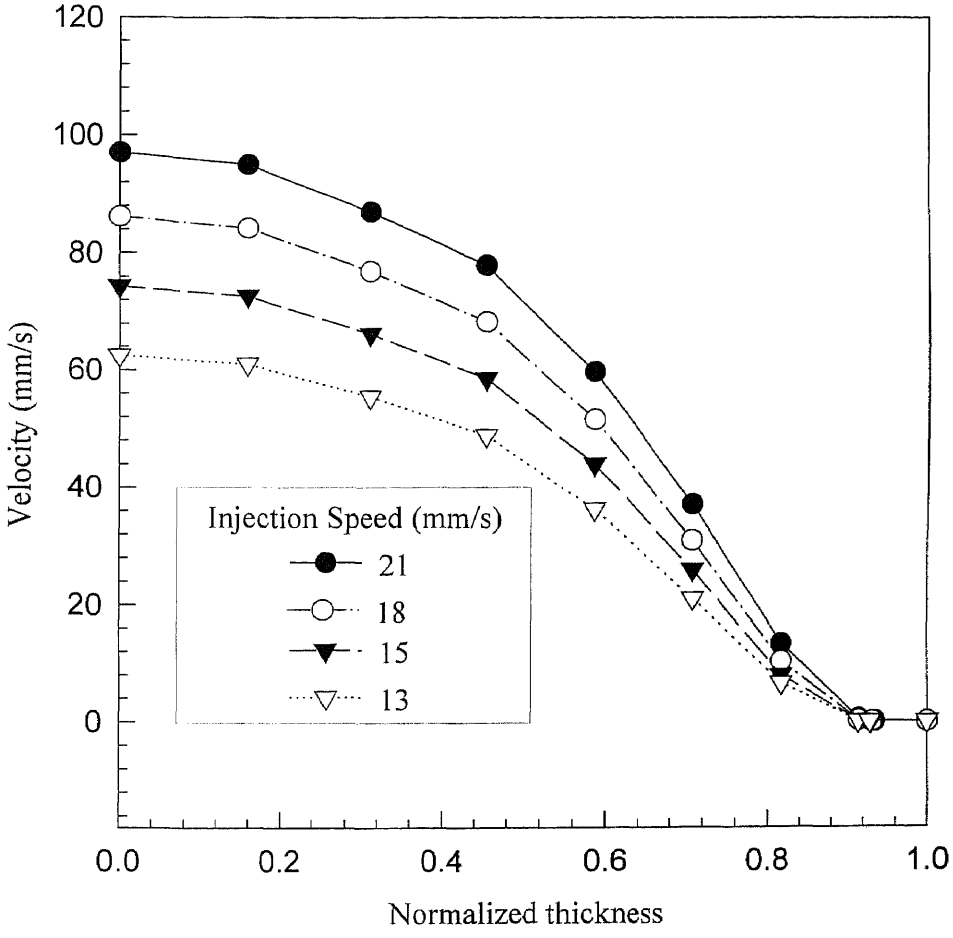

Figure A3 Velocity profiles behind the AMF at a melt temperature of 304 °C and a mold temperature of 35 °C for PET/LCP (85/15 wt %) blend. 0.0 is the center of mold cavity and 1.0 is the mold wall.

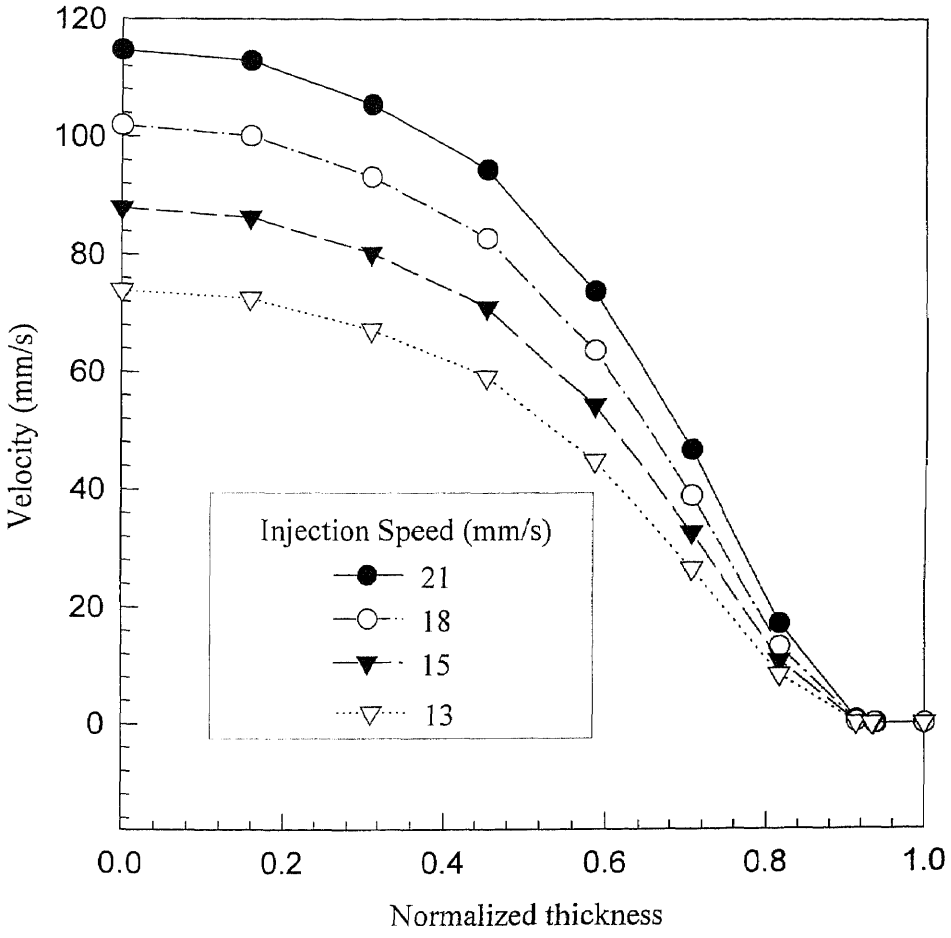

Figure A4 Velocity profiles behind the AMF at a melt temperature of 320 °C and a mold temperature of 50 °C for PET/LCP (85/15 wt %) blend. 0.0 is the center of mold cavity and 1.0 is the mold wall.

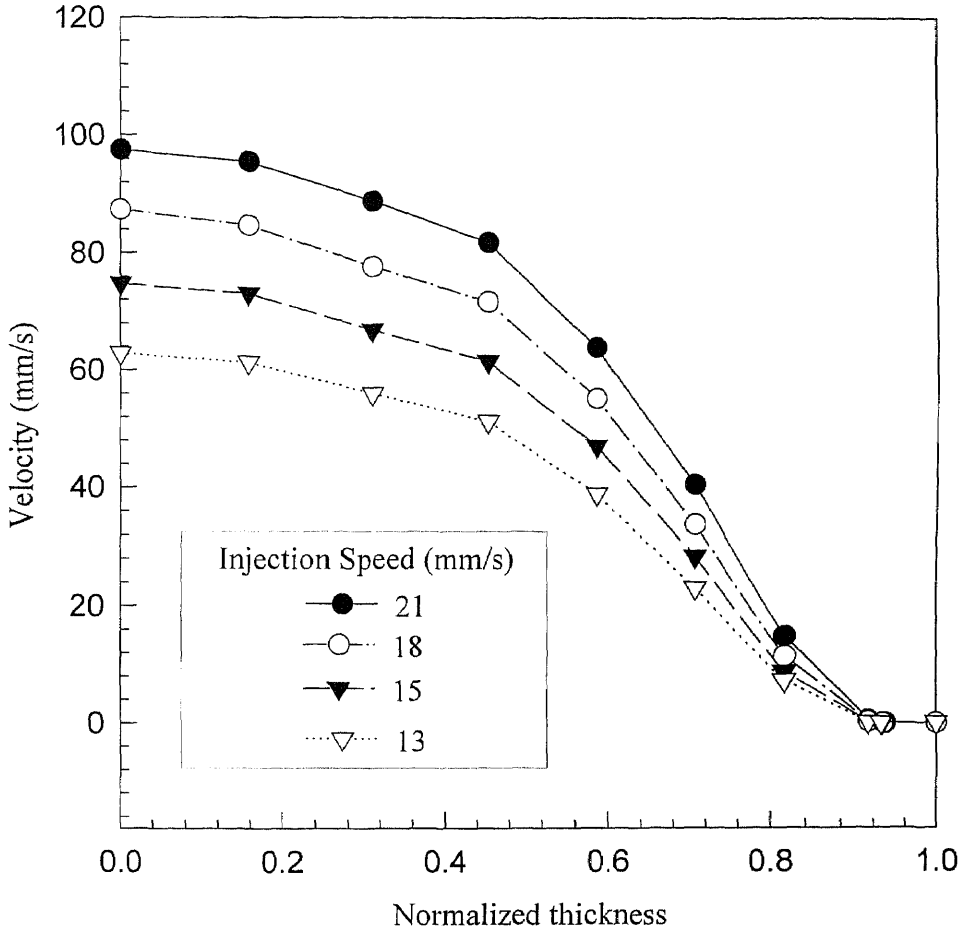

Figure A5 Velocity profiles behind the AMF at a melt temperature of 304 °C and a mold temperature of 50 °C for PET/LCP (85/15 wt %) blend. 0.0 is the center of mold cavity and 1.0 is the mold wall.

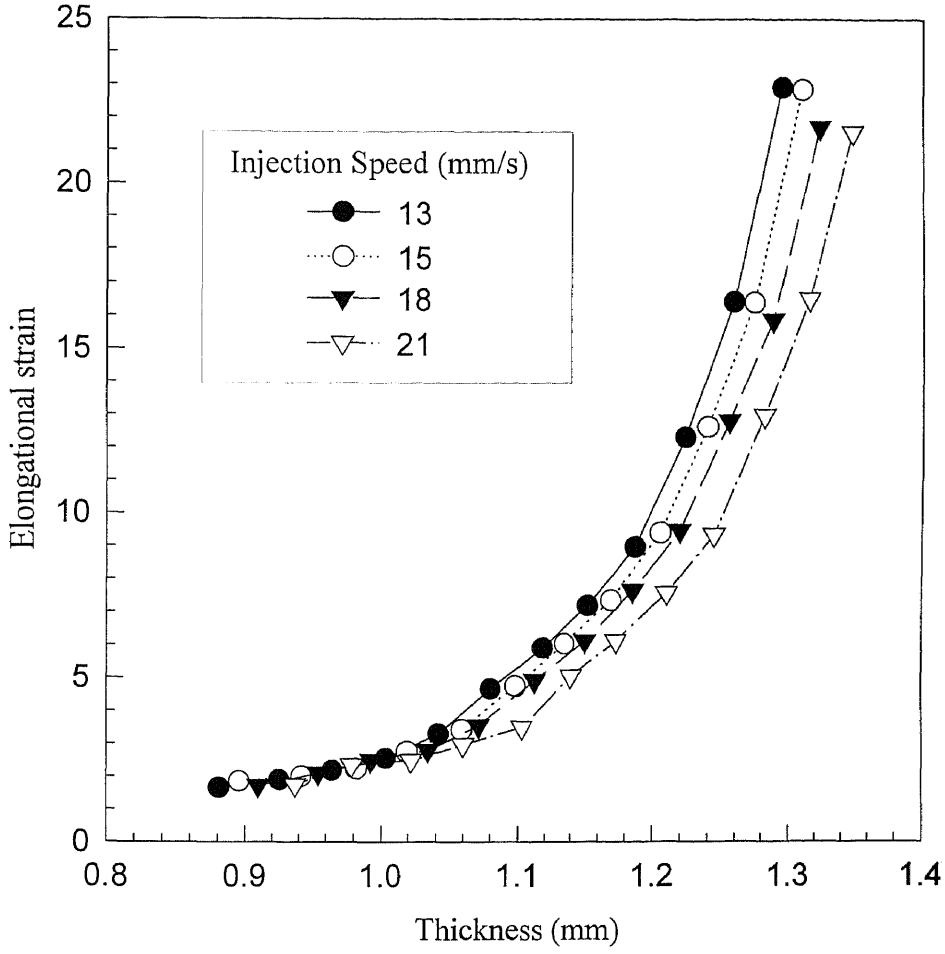

Figure A6 Elongational strain distribution across the thickness of mold cavity at a melt temperature of 304 °C and a mold temperature of 18 °C for PET/LCP (85/15 wt %) blend.

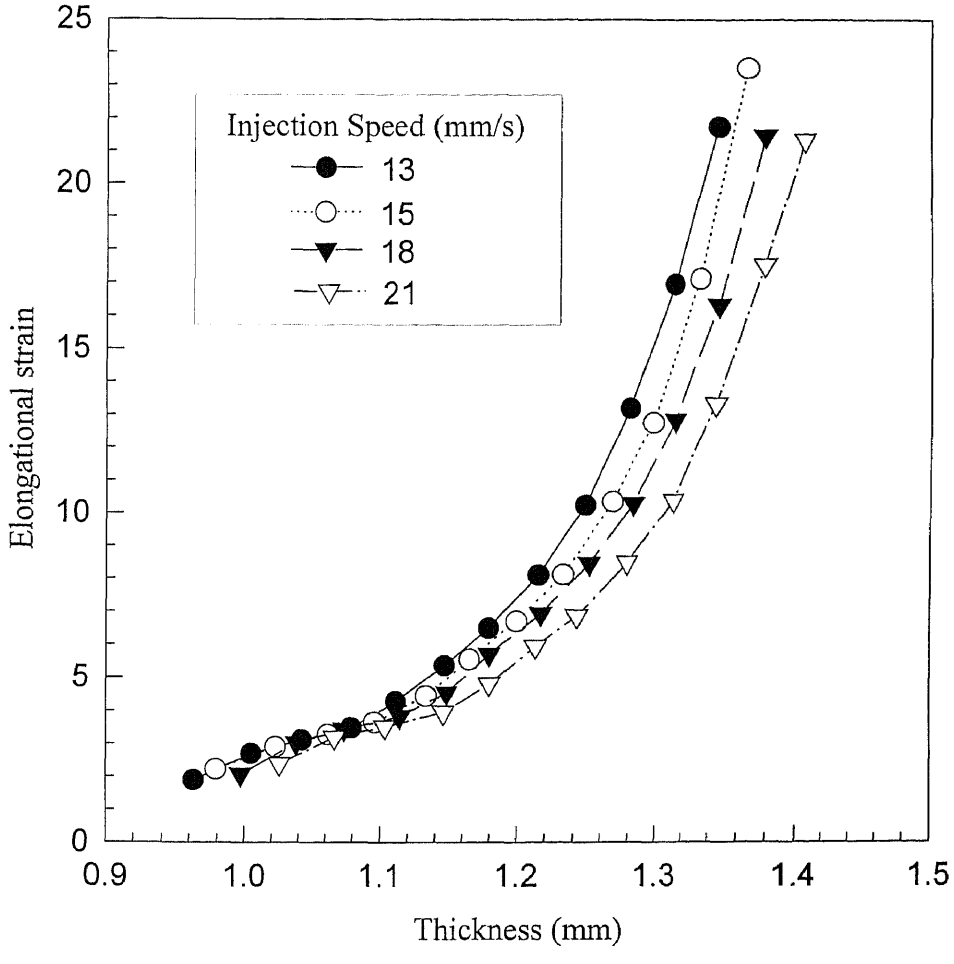

Figure A7 Elongational strain distribution across the thickness of mold cavity at a melt temperature of 320 °C and a mold temperature of 35 °C for PET/LCP (85/15 wt %) blend.

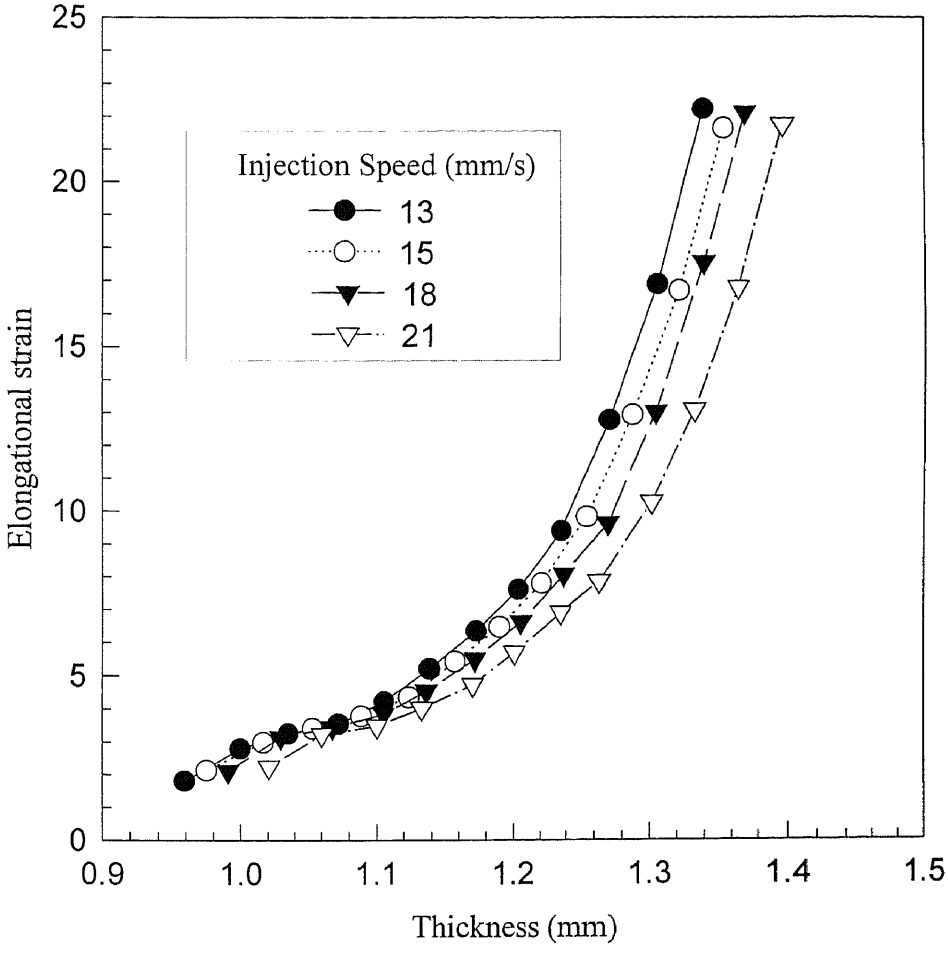

Figure A8 Elongational strain distribution across the thickness of mold cavity at a melt temperature of 304 °C and a mold temperature of 35 °C for PET/LCP (85/15 wt %) blend.

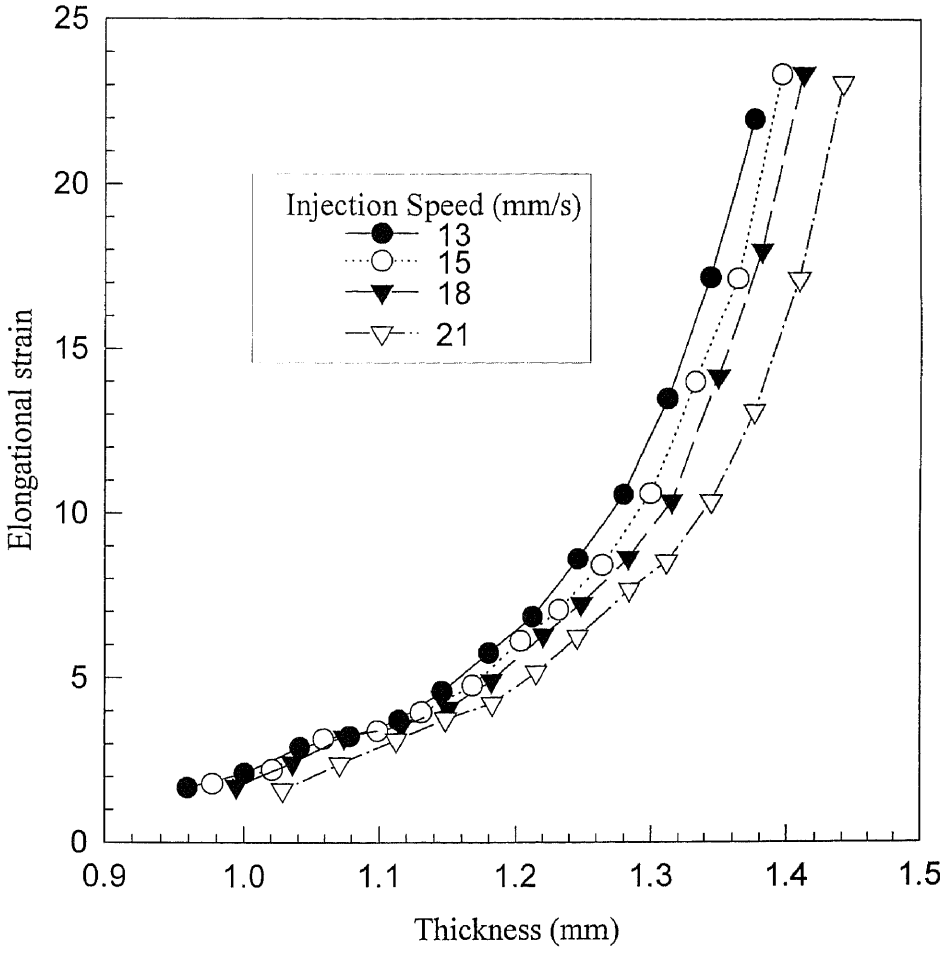

Figure A9 Elongational strain distribution across the thickness of mold cavity at a melt temperature of 320 °C and a mold temperature of 50 °C for PET/LCP (85/15 wt %) blend.

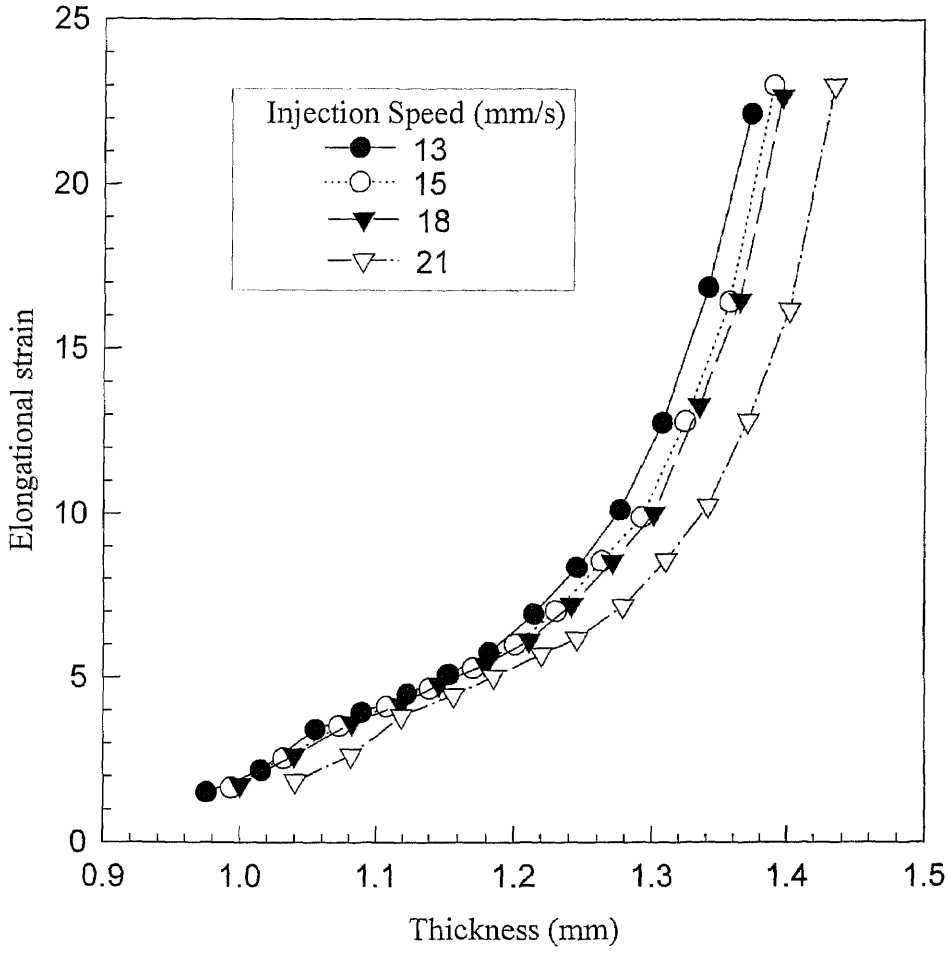

Figure A10 Elongational strain distribution across the thickness of mold cavity at a melt temperature of 304 °C and a mold temperature of 50 °C for PET/LCP (85/15 wt %) blend.

APPENDIX B

EXPERIMENTAL RESULTS FOR VISCOSITY

Table B1 Viscosity of PET/LCP (95/5 wt %) blend

Temperature: 500 °F

Measurements		Calculations	
Piston pressure (psi)	Extrusion time X 4 (s)	Shear Rate (1/s)	Viscosity (Pa.s)
10	59.900	716.169	72.104
15	37.667	1137.893	68.072
20	27.950	1534.832	67.289
25	21.700	1976.893	65.303
30	17.500	2451.347	63.196
40	12.933	3316.985	62.272
50	9.964	4304.492	59.982

Temperature of 536 °F

Measurements		Calculations	
Piston pressure (psi)	Extrusion time X 4 (s)	Shear Rate (1/s)	Viscosity (Pa.s)
5	48.600	882.686	29.25
10	21.867	1961.795	26.32
15	13.500	3177.672	24.376
20	8.333	5148.035	20.061
25	6.800	6308.614	20.463
30	5.350	8018.425	19.320
40	3.833	11191.906	18.455
55	2.700	15888.361	17.875

Temperature of 554 °F

Measurements		Calculations	
Piston pressure (psi)	Extrusion time X 4 (s)	Shear Rate (1/s)	Viscosity (Pa.s)
5	33.250	1290.998	19.999
10	13.733	3123.758	16.531
15	8.350	5137.554	15.076
20	5.800	7996.306	13.963
30	3.650	11753.034	13.181

Table B2 Viscosity of PET/LCP (85/15 wt %) blend

Temperature: 500 °F

Measurements		Calculations	
Piston pressure (psi)	Extrusion time X 4 (s)	Shear Rate (1/s)	Viscosity (Pa.s)
10	68.033	634.561	81.895
15	42.633	1006.229	76.979
20	30.633	1400.404	73.748
25	23.900	1794.919	71.924
30	19.333	2218.930	69.816
40	12.466	3441.246	60.023
50	9.300	4304.493	59.982

Temperature: 536 °F

Measurements		Calculations	
Piston pressure (psi)	Extrusion time X 4 (s)	Shear Rate (1/s)	Viscosity (Pa.s)
5	57.133	750.855	34.386
10	23.867	1797.401	28.729
15	13.933	3078.918	25.157
20	9.650	4468.602	23.232
25	7.467	5745.088	22.471
30	5.433	7895.928	19.619
40	3.766	11391.018	18.133
50	2.800	15320.920	16.853

Temperature: 554 °F

Measurements		Calculations	
Piston pressure (psi)	Extrusion time X 4 (s)	Shear Rate (1/s)	Viscosity (Pa.s)
5	31.067	1389.600	18.698
10	13.400	3221.720	16.130
15	7.825	5517.068	14.129
20	5.367	8006.442	12.921
25	4.233	10151.329	12.738
30	3.333	12892.462	12.036

Table B3 Viscosity of PET/LCP (75/25 wt %) blend

Temperature: 500 °F

Measurements		Calculations	
Piston pressure (psi)	Extrusion time X 4 (s)	Shear Rate (1/s)	Viscosity (Pa.s)
10	75.833	565.698	91.284
15	46.966	913.396	84.792
20	29.966	1431.575	72.143
25	23.233	1846.450	69.916
30	18.133	2365.773	65.482
40	11.133	3853.281	53.605
50	8.667	4949.645	52.163

Temperature: 536 °F

Measurements		Calculations	
Piston pressure (psi)	Extrusion time X 4 (s)	Shear Rate (1/s)	Viscosity (Pa.s)
5	107.233	400.060	64.530
10	34.866	1230.240	41.970
15	17.666	2427.760	31.910
20	9.933	4320.090	23.910
25	6.533	6569.460	19.650
30	4.800	8937.200	17.330
40	3.066	14019.140	14.730

Temperature: 554 °F

Measurements		Calculations	
Piston pressure (psi)	Extrusion time X 4 (s)	Shear Rate (1/s)	Viscosity (Pa.s)
3	41.600	1031.210	15.020
5	22.133	1938.480	13.320
10	9.066	4750.670	10.860
15	5.466	7842.630	9.880
20	3.900	10999.630	9.390
25	3.033	14159.940	9.120

APPENDIX C

PROGRAMS FOR CALCULATIONS OF VELOCITY AND MODULUS

Appendix C1 Program for Calculation of Velocity Profile in the AMF

```
clf
cla
clear all
%*****************************************************************
%                                                                 *
%        THIS IS THE CALCULATION OF VELOCITY RPOFILE AND          *
%     ELONATIONAL RATE FROFILE IN MELT FRONT OF MOLD CAVITY       *
%        (USE FLOW RATE BALANCE WITH EQUAL HEIGHT ELEMENT)        *
%                                                                 *
%*****************************************************************


%*****************************************************************
% H_GAP:     Thickness of mold Cavity                             *
% T_STEP:    Increment of filling time                            *
% Y_STEP:    Increment of Y direction                             *
% POINT_Y:   Y Coordinate of specified position(vertical)         *
% POINT_Z:   Z Coordinate of specified position(horizontal)       *
% H_FLAYER:  Thickness of frozen layer                            *
% YI:        Y increment at entrance of flow channel              *
% V_INLET:   Velocity at entrance of flow channel                 *
% Z_FRONT:   Z coordinate of melt front curve                     *
% AVE_V:     Average velocity of the melt front                   *
% VOY:             Velocity at melt front curve in Y direction    *
% VOZ:             Velocity at melt front curve in Z direction    *
% VY, VZ:    Y and Z velocity at each node                        *
% Y_,Z_:     Y and Z coordinates                                  *
% VYU,VYL:   Velocity of upper and lower boundary of a element at *
             specified point                                      *
% VZU,VZL:   Velocity of upper and lower boundary of a element at *
             specified point                                      *
% Path_Y,Z:  Y and Z path of a point during filling               *
% PATH_Y:    Final Y coordinate of deformed fluid element         *
% N:         Element No. in melt region                           *
% NN:        Element No. in frozen region                         *
% MM:        Number of nodes in each element along Z direction    *
% M:         Control variable for filling time(M>=100)            *
% Y_VZERO:   Y coordinate of V zero at entrance of flow channel   *
% ZF:        Z coordinate at boundary of frozen region            *
% O_LENGTH:  Original length of particle                          *
%*****************************************************************
%*****************************************************************
%                                                                 *
%                          INPUT DATA                             *
%*****************************************************************
```

```
H_GAP=0.125*25.4;

N=200;

NN=20;

MM=20;

M=100;

%(Trial could be 1 2 3 for different melt temperature)

Trial=3;

for OPTION=10:2:16

%(OPTION could be 10, 12, 14, 16 for different Velocity)
OPTION=10;

%*****Calculation of V_INLET***********

[V_INLET,Y_VZERO,H_FLAYER]=FITTING(H_GAP,N,OPTION,Trial);

YI=(H_GAP/2-H_FLAYER)/N;

YI1=H_FLAYER/NN;

T_STEP=0.005;

AVE_V=4*(H_GAP/2-H_FLAYER)*V_INLET(1)/3/H_GAP;

Y_STEP=0.05;

%******Calculation of starting coordinate of fluid elements******

%(if calculating single point, K=1 ~ 1, if more points K > H_GAP/Y_STEP,
about 20)

for K=1:2

      if Y_STEP*K <Y_VZERO

            POINT_Y1=0+Y_STEP*K;

            POINT_Z1=0.1;

            POINT_Y2=0.1+Y_STEP*K;

            POINT_Z2=0.1;

            POINT_Y3=0+Y_STEP*K;

            POINT_Z3=0.2;

            POINT_Y4=0.1+Y_STEP*K;

            POINT_Z4=0.2;

            if K==1
```

```
            O_LENGTH=POINT_Y2-POINT_Y1;

            end

      else
            break;

      end

Y_STEP=0.2;

%********calculation of coordinate of free surface***********

for i=1:N+NN+1

      if i<=N+1

            Z_FRONT(i)=H_GAP/2+((H_GAP/2).^2-(YI*(i-1)).^2).^0.5;
      else

            Z_FRONT(i)=H_GAP/2+((H_GAP/2).^2-(YI*N+YI1*(i-N-
1)).^2).^0.5;
      end
end

%*****************************************************************
%                                                                 *
%           Calculation of Velocity in Y and Z Direction          *
%                 (  Vz=AveV-tg(Q)*Vy  )                          *
%                                                                 *
%*****************************************************************


VOY(1)=0;

for i=1:N

      ZO=Z_FRONT(i)-Z_FRONT(i+1);

      TEMP_A=-YI*(YI*i/((H_GAP/2).^2-
(YI*i).^2).^0.5)/2+ZO/2+Z_FRONT(i+1)/2;

      TEMP_B=Z_FRONT(i)/2+YI*YI*(i-1)/((H_GAP/2).^2-(YI*(i-
1)).^2).^0.5/2-ZO/2;

      VOY(i+1)=(TEMP_B*VOY(i)+YI*(V_INLET(i+1)+V_INLET(i))/2-
YI*AVE_V)/TEMP_A;

end

for i=1:NN+1

ZF(i)=YI1*(i-1)*H_GAP/(2*H_FLAYER);

end

for i=1:NN

      if i==NN

            VOY(i+N+1)=0;
```

```
        else
        ZO=Z_FRONT(N+i)-Z_FRONT(N+i+1);
        TAN1=(YI*N+YI1*i)/((H_GAP/2).^2-(YI*N+YI1*i).^2).^0.5;
        TEMP_A=-YI1*TAN1/2+ZO/2+(Z_FRONT(N+i+1)-ZF(i+1))/2;
        TAN2=(YI*N+YI1*(i-1))/((H_GAP/2).^2-(YI*N+YI1*(i-1)).^2).^0.5;
        TEMP_B=YI1*TAN2/2-ZO/2+(Z_FRONT(N+i)-ZF(i))/2;
        VOY(i+N+1)=(TEMP_B*VOY(N+i)-YI1*AVE_V)/TEMP_A;
        end
end

VOZ(1)=AVE_V;

for i=1:N
        VOZ(i+1)=AVE_V-VOY(i+1)*YI*i/((H_GAP/2).^2-(YI*i).^2).^0.5;
end

for i=1:NN-1
        TEMP=(YI1*i+H_GAP/2-H_FLAYER)/((H_GAP/2).^2-(YI1*i+H_GAP/2-
H_FLAYER).^2).^0.5;
        VOZ(N+i+1)=AVE_V-VOY(N+i+1)*TEMP;
end
VOZ(N+NN+1)=0;
%*****************************************************************
%                                                                 *
%            Calculation of Velocity for Each Node                *
%                                                                 *
%*****************************************************************


for i=1:N+NN+1
        for j=1:MM
                VY(i,j)=VOY(i)*j/MM;
                if i<=N+1
                        VZ(i,j)=V_INLET(i)-AVE_V+(VOZ(i)-AVE_V-(V_INLET(i)-
AVE_V))*j/MM;
                else
                        VZ(i,j)=-AVE_V+(VOZ(i)-AVE_V-(0-AVE_V))*j/MM;
                end
```

```
            if i<=N+1
                  Z_(i,j)=Z_FRONT(i)*j/MM;
                  Y_(i,j)=YI*(i-1);
            else
                  Z_(i,j)=ZF(i-N)+(Z_FRONT(i)-ZF(i-N))*j/MM;
                  Y_(i,j)=YI*N+YI1*(i-N-1);
      end

      end
end

%*****************************************************************
%                                                                 *
%           Calculation of Elongational Rate                      *
%                                                                 *
%*****************************************************************

%----------Calculation of Path for Given Points ----------------

for j =1:M

%--Looking The Element (No) for a given point(POINT_Y2, POINT_Z2)----

  TEMP_Y=0;

  [No]=ELE_No(TEMP_Y,YI,YI1,N,NN,POINT_Y2);

[VYU,VYL,VZU,VZL]=POINT_V(N,AVE_V,V_INLET,Z_FRONT,POINT_Z2,VOY,VOZ,No);

  if POINT_Z2 < 0.09

      Path_Y2(j)=Path_Y2(j-1);

      Path_Z2(j)=Path_Z2(j-1)+Vz*T_STEP;

  else

      if POINT_Y2 >=2*H_FLAYER*POINT_Z2/H_GAP+YI*N

            Path_Y2(j)=Path_Y2(j-1);

            Path_Z2(j)=Path_Z2(j-1)+Vz*T_STEP;

      else

            [Vz]=VELOCITY_No(VZL,VZU,No,YI,YI1,N,POINT_Y2);

            [Vy]=VELOCITY_No(VYL,VYU,No,YI,YI1,N,POINT_Y2);

            Path_Y2(j)=POINT_Y2;

            Path_Z2(j)=POINT_Z2;

            POINT_Y2=POINT_Y2+Vy*T_STEP;

            POINT_Z2=POINT_Z2+Vz*T_STEP;
```

```
            POINT_Z2=POINT_Z2+Vz*T_STEP;
        end
            %plot(Path_Z2, Path_Y2, '*')
    end
    figure(1)
    hold on

%-----------------Point(POINT_Y1, POINT_Z1)-----------------
    [No]=ELE_No(TEMP_Y,YI,YI1,N,NN,POINT_Y1);
   [VYU,VYL,VZU,VZL]=POINT_V(N,AVE_V,V_INLET,Z_FRONT,POINT_Z1,VOY,VOZ,No);
    if POINT_Z1 < 0.09
        Path_Y1(j)=Path_Y1(j-1);
        Path_Z1(j)=Path_Z1(j-1)+Vz*T_STEP;
        break;
    else
        if POINT_Y1 >=2*H_FLAYER*POINT_Z1/H_GAP+YI*N
            Path_Y1(j)=Path_Y1(j-1);
            Path_Z1(j)=Path_Z1(j-1)+Vz*T_STEP;
            %POINT_Y1=POINT_Y1;
            %POINT_Z1=POINT_Z1+Vz*T_STEP;
            break;
        else
            [Vz]=VELOCITY_No(VZL,VZU,No,YI,YI1,N,POINT_Y1);
            [Vy]=VELOCITY_No(VYL,VYU,No,YI,YI1,N,POINT_Y1);
            Path_Y1(j)=POINT_Y1;
            Path_Z1(j)=POINT_Z1;
            POINT_Y1=POINT_Y1+Vy*T_STEP;
            POINT_Z1=POINT_Z1+Vz*T_STEP;
        end
    end
%end of M Loop
end
m13=j;
```

```
for j =1:M

%---Looking The Element (No) for a given point(POINT_Y4, POINT_Z4)---

  TEMP_Y=0;

  [No]=ELE_No(TEMP_Y,YI,YI1,N,NN,POINT_Y4);
 [VYU,VYL,VZU,VZL]=POINT_V(N,AVE_V,V_INLET,Z_FRONT,POINT_Z4,VOY,VOZ,No);

  if POINT_Z4 < 0.09
      Path_Y4(j)=Path_Y4(j-1);

      Path_Z4(j)=Path_Z4(j-1)+Vz*T_STEP;

  else
      if POINT_Y4 >=2*H_FLAYER*POINT_Z4/H_GAP+YI*N

            Path_Y4(j)=Path_Y4(j-1);

            Path_Z4(j)=Path_Z4(j-1)+Vz*T_STEP;

      else

            [Vz]=VELOCITY_No(VZL,VZU,No,YI,YI1,N,POINT_Y4);

            [Vy]=VELOCITY_No(VYL,VYU,No,YI,YI1,N,POINT_Y4);

            Path_Y4(j)=POINT_Y4;

            Path_Z4(j)=POINT_Z4;

            POINT_Y4=POINT_Y4+Vy*T_STEP;

            POINT_Z4=POINT_Z4+Vz*T_STEP;

      end
            %plot(Path_Z4, Path_Y4, '*')

   end

%---Looking The Element (No) for a given point(POINT_Y3, POINT_Z3)---

  [No]=ELE_No(TEMP_Y,YI,YI1,N,NN,POINT_Y3);

[VYU,VYL,VZU,VZL]=POINT_V(N,AVE_V,V_INLET,Z_FRONT,POINT_Z3,VOY,VOZ,No);

  if POINT_Z3 < 0.09

      Path_Y3(j)=Path_Y3(j-1);

      Path_Z3(j)=Path_Z3(j-1)+Vz*T_STEP;

      break;

  else

      if POINT_Y3 >=2*H_FLAYER*POINT_Z3/H_GAP+YI*N

            Path_Y3(j)=Path_Y3(j-1);

            Path_Z3(j)=Path_Z3(j-1)+Vz*T_STEP;
```

```
            break;
      else
            [Vz]=VELOCITY_No(VZL,VZU,No,YI,YI1,N,POINT_Y3);
            [Vy]=VELOCITY_No(VYL,VYU,No,YI,YI1,N,POINT_Y3);
            Path_Y3(j)=POINT_Y3;
            Path_Z3(j)=POINT_Z3;
            POINT_Y3=POINT_Y3+Vy*T_STEP;
            POINT_Z3=POINT_Z3+Vz*T_STEP;
      end
      %plot(Path_Z3, Path_Y3, '*')
  end
%end of M Loop
end
m24=j;
%*****************************************************************
%                                                                *
%           Sketch a Flow Region                                 *
%                                                                *
%*****************************************************************
      B_1=[0 H_GAP/2];
      B_2=[H_GAP/2-H_FLAYER,H_GAP/2];
      plot(H_GAP/2,H_GAP/2,'.')
      hold on
      plot(0,H_GAP/2-H_FLAYER,'.')
      hold on
      plot(H_GAP,0,'.')
      hold on
      for i=1:2
      plot(B_1,B_2,'-.')
      end
for i=1:N+NN+1
      CurveZ(i)=Z_FRONT(i);
      if i<=N+1
            CurveY(i)=YI*(i-1);
```

```
      else

            CurveY(i)=YI*N+YI1*(i-N-1);
      end
end

plot(CurveZ,CurveY,'-')

%*****************************************************************
%                                                                 *
%           Sketch the deformation of a particle                  *
%                                                                 *
%*****************************************************************

a=4

axis([-0.5 3.5 0 3.5])

for j=1:14:m13-1

      X1=[Path_Y1(j) Path_Y2(j)];

      Y1=[Path_Z1(j) Path_Z2(j)];

      hndl=plot(Y1,X1,'-');


      set(hndl,'LineWidth',a);

      hold on

      X3=[Path_Y4(j) Path_Y3(j)];

      Y3=[Path_Z4(j) Path_Z3(j)];

      hndl1=plot(Y3,X3,'-');

      set(hndl1,'LineWidth',a);

      if a<=0.5
      a=0.5;

      else

      a=a-0.5;
      end

      hold on
end

      X1=[Path_Y1(m13-1) Path_Y2(m13-1)];

      Y1=[Path_Z1(m13-1) Path_Z2(m13-1)];

      %plot(Y1,X1,'-')

      hold on

      X3=[Path_Y4(m13-1) Path_Y3(m13-1)];
```

```
      Y3=[Path_Z4(m13-1) Path_Z3(m13-1)];
      %plot(Y3,X3,'-')
      hold on

for j=1:14:m13-1
      X2=[Path_Y2(j) Path_Y4(j)];
      Y2=[Path_Z2(j) Path_Z4(j)];
      %plot(Y2,X2,'-')
      hold on
      X4=[Path_Y3(j) Path_Y1(j)];
      Y4=[Path_Z3(j) Path_Z1(j)];
      %plot(Y4,X4,'-')
      hold on
end
      X2=[Path_Y2(m13-1) Path_Y4(m13-1)];
      Y2=[Path_Z2(m13-1) Path_Z4(m13-1)];
      %plot(Y2,X2,'-')
      hold on
      X4=[Path_Y3(m13-1) Path_Y1(m13-1)];
      Y4=[Path_Z3(m13-1) Path_Z1(m13-1)];
      %plot(Y4,X4,'-')
      hold on
hold off
%*****************************************************************
%                                                                 *
%          Sketch the Velocity Vector and Calculation of Strain   *
%                                                                 *
%*****************************************************************
figure(2)
plot(0,2*1.5875,'.')
hold on
quiver(Z_,Y_,VZ+AVE_V,VY)
hold off
```

```
Length(K)=((Path_Y1(m24-1)-Path_Y2(m24-1)).^2+(Path_Z1(m24-1)-
Path_Z2(m24-1)).^2).^0.5;

ELONGA(K)=(Length(K)-O_LENGTH)/O_LENGTH;

PATH_Y(K)=Path_Y2(m24-1);


%End of K loop

end


%*****************************************************************
%                                                                 *
%     Out put the Elongation and Coordinate                       *
%                                                                 *
%*****************************************************************

fid=fopen('PathY.txt','a+');

count=fprintf(fid, '%7.4f\t',PATH_Y);

fid1=fopen('Elonga.txt','a+');

count1=fprintf(fid1,'%8.4f\t',ELONGA);

fid2=fopen('DEFORM.txt','a+');

count=fprintf(fid2, '%7.4f\t',X11);

count=fprintf(fid2, '%7.4f\t',X12);

count=fprintf(fid2, '%7.4f\t',Y11);

count=fprintf(fid2, '%7.4f\t',Y12);

%end of OPTION Loop

end
```

Appendix C2 Program for Calculation of Modulus of PET/LCP Blend

```
%*****************************************************************
%                                                                 %
%     Calculation of Tensile Modulus of PET/LCP Blend             %
%                                                                 %
%*****************************************************************%


%*****************************************************************
%                                                                 %
% H_GAP:     Thickness of mold Cavity                             %
% VOL:             Volume fraction of LCP                         %
% Em:        Modulus of matrix                                    %
% T:         Melt temperature                                     %
% Elong_T:   Elongation strain and corresponding to Y coordinates %
```

```
% Asp_Ra:   Aspect ratio of LCP fibers                          %
% PATH_Y1:  Y coordinate                                        %
% Y_STEP:   Y increment                                         %
% Y_LIMIT:                                                      %
% L_D:            Aspect ratio of LCP fibers                    %
% Ef:       Modulus og LCP fiber                                %
% L_DCORE:  Aspect ratio of LCP fibers in core region           %
% EfCORE:   Modulus of LCP fibers in core region                %
% ESKIN:    Modulus of skin layer                               %
% ECORE:    Modulus of core layer                               %
% ETATOL:   Modulus of part                                     %
% In-Spd:   Injection speed                                     %
% N:        Index of Elong_T#.dat                               %
% M:        Loop number for numerical integratation             %
%*****************************************************************


clf
cla
clear all

%****************Input Data and Load File************************

N=13;

M=50;

T=304;

load 'Elong_T8.dat'

Elong_T=Elong_T8;

E10=Elong_T(1,:);

E12=Elong_T(3,:);

E14=Elong_T(5,:);

E16=Elong_T(7,:);


Y10=Elong_T(2,:);

Y12=Elong_T(4,:);

Y14=Elong_T(6,:);

Y16=Elong_T(8,:);

VOL=0.131;

H_GAP=25.4*0.125;

Em=2.9;

%***Calculation of Aspect Ratio at Different Injection Speed*****

for j=1:4

      K=0;
```

```
for i=1:N
      if j==1
        Asp_Ra(i)=(E10(i)+1).^1.5;
        PATH_Y1(i)=Y10(i);
      end
      if j==2
        Asp_Ra(i)=(E12(i)+1).^1.5;
        PATH_Y1(i)=Y12(i);
      end
      if j==3
        Asp_Ra(i)=(E14(i)+1).^1.5;
        PATH_Y1(i)=Y14(i);
      end
      if j==4
        Asp_Ra(i)=(E16(i)+1).^1.5;
        PATH_Y1(i)=Y16(i);
      end
end
fid=fopen('Asp_Ra.txt','a+');
count=fprintf(fid, '%7.4f\t',Asp_Ra);
if j==1,Y_LIMIT=PATH_Y1(1),end
Y_STEP=(Y_LIMIT-PATH_Y1(N))/M;
Yt=PATH_Y1(N);

%***************Calculation of Ef at Each Point***************
for i=N-1:-1:1
        while Yt<=PATH_Y1(i) & Yt>=PATH_Y1(i+1)
            if Yt>=Y_LIMIT, break, end
            K=K+1;
            temp=(PATH_Y1(i)-Yt)*(Asp_Ra(i)-Asp_Ra(i+1));
              L_D(K)=Asp_Ra(i)-temp/(PATH_Y1(i)-PATH_Y1(i+1));
```

```
                temp1=0.0069*(log(L_D(K).^(-2))).^2;
                temp2=-2.2721+0.1952*log(L_D(K).^(-2));
                temp=temp1+temp2;
                Ef(K)=(exp(temp)).^(-1);
                B1(K)=(Ef(K)/Em-1)/(Ef(K)/Em+2*L_D(K));
                Yt=Yt+Y_STEP;
                Yy(K)=Yt;
            end
        end
        E(j)=0;
        if T==304, M1=0, end
        if T==320, M1=5,end

%*************Numerical Integration***************
        for i=1:M-M1
            TEMP1=Em*(1+2*L_D(i)*VOL*B1(i))/(1-B1(i)*VOL);

            if i==1
                E(j)=E(j)+TEMP1*Y_STEP;
            else
                TEMP2=Em*(1+2*L_D(i-1)*VOL*B1(i-1))/(1-B1(i-1)*VOL);
                E(j)=E(j)+(TEMP1+TEMP2)*Y_STEP/2;
        end
        if j==1
            Yy10=Yy;
            L_D10=L_D;
        end
        if j==2
            Yy12=Yy;
            L_D12=L_D;
        end
        if j==3
```

```
            Yy14=Yy;
            L_D14=L_D;
        end
        if j==4
            Yy16=Yy;
            L_D16=L_D;
        end
end
%************Calculation of Modulus of PET/LCP Blend************
L_DCORE=1;
temp=-2.2721+0.1952*log(L_DCORE.^(-2))+0.0069*(log(L_DCORE.^(-2))).^2;
EfCORE=(exp(temp)).^(-1);
ESKIN=E(j)/Y_LIMIT;
BCORE=(EfCORE/Em-1)/(EfCORE/Em+2*L_DCORE);
ECORE=Em*(1+2*L_DCORE*BCORE*VOL)/(1-BCORE*VOL);
ECORE=PATH_Y1(N)*ECORE/Y_LIMIT;
ETATOL(j)=((ECORE+ESKIN)*Y_LIMIT+((1-VOL)*Em+VOL*Ef(K))*(H_GAP/2-
Y_LIMIT))*2/H_GAP
end
axis([0.8 1.8 0 200])
figure(8)
%plot(Yy10(6:64),L_D10(6:64),'-')
hold on
plot(Yy12(6:64),L_D12(6:64),'y-')
hold on
plot(Yy14(6:64),L_D14(6:64),'r-')
hold on
plot(Yy16(6:64),L_D16(6:64),'g-')
hold off
In_Spd(1)=10;
for i=2:4
```

```
In_Spd(i)=In_Spd(i-1)+2;
end
figure(9)
plot(In_Spd, ETATOL,'-')
```

APPENDIX D

NUMERICAL INTEGRATION OF EQUATION 5.31

According to Simpson Equation, for any function,

$$z = f(y) \tag{C1}$$

we have

$$S = \int_a^b f(y)dy = \frac{b-a}{3n}\left(\frac{f(a)-f(b)}{2} + \sum_{k=1}^{n}(2f(y_{k-\frac{1}{2}}) + f(y_k))\right) \tag{C2}$$

By applying Eq. C2 to Eq. 5.31 and by letting

$$f(y) = \frac{1-2B(\varepsilon+1)^{3/2}V_f}{1-BV_f} \tag{C3}$$

and $a = 0$; $b = H/2$; $y_{k-0.5} = (k-0.5)*H/(2n)$; and $y_k = k*H/(2n)$. Then we can solve Eq. 5.31.

REFERENCES

Acierno, D., and M. R. Nobile. 1993."Processing and Properties of Thermotropic Liquid Crystalline Polymers." *Thermoplastic Liquid Crystal Polymer Blends*. F. P. La Mantia (Eds). Technomic Publishing Company, Inc., New York, p.76.

Baird, D. G and R. Ramanathan.1990. "The In-situ Generation of Liquid Crystalline Reinforcements in Engineering Thermoplastics." in *Contemporary Topics in Polymer Science*, Vol. 6, B. M. Culbertson (Eds). Plenum Press, New York, pp. 73-93.

Beery, D., S. Kenig, and A. Siegmann. 1991a. "Structure Development During Flow of Polyblends Containing Liquid Crystalline Polymers." *Polym. Eng. Sci.* 31(6): 451.

Beery, D., S. Kenig, and A. Siegmann. 1991b. "Structure and Properties of Molded Polyblends Containing Liquid Crystalline Polymers." *Polym. Eng. Sci.* 31(6): 459.

Behrens, B. A., M. J.Crochet, C. D. Denson, and A. B. Metznen. 1987. "Transient Free-Surface Flows: Motion of a fluid Advancing in a Tube." *AIChE J.* 33(7):1178-1186.

Blizard, K. G. and D. G. Baird. 1987. "The Morphology and Rheology of Polymer Blends Containing a Liquid Crystalline Copolyester." *Polym. Eng. Sci.* 27(9): 653.

Blizard, K. G., C. Federici, O. Federico, and L. L. Chapoy. 1990. "The Morphology of Extruded Blends Containing a Thermotropic Liquid Crystalline Polymer." *Polym. Eng. Sci.* 30(22): 1442.

Brinkmann, T., P. Hoeck, and W. Michaeli 1991. *Proceedings of Compalloy Europe `91,* Luxembourg, 24 – 25 October: 307.

Carfagna, C., E. Amendola, L. Nicolais, D. Acierno, O. Francescangeli, B. Yang, and F. Rustichelli. 1991. "Blends of a Polyetherimide and a Liquid Crystalline Polymer: Fiber Orientation and Mechanical Properties." *J. of Appl. Polym. Sci.* 43: 839.

Chan, T. W. and A. I. Isayev, 1992, *SPE ANTEC Technical Papers*, 38:1148.

Chung, T. 1987. "How Well Do Various Blends of LCP and Nylon 12 work?" *Plastics Engineering*, 43 (10): 39.

Cogswell, F. N., B. P. Griffin, and J. B. Rose. May 31, 1983, U. S. patent 4,386,174.

REFERENCES
(Continued)

CMOLD. 1997. *User's Manual*. AC Technology, Ithaca, New York.

Crevecoeur, G. and G. Croeninckc. 1990. "Morphology and Mechanical Properties of Thermoplastic Composites Containing a Thermotropic Liquid Crystalline Polymer." *Polym. Eng. Sci.* 30(9): 532.

Dietz, W, J. L. White, and E. S. Clark. 1978. "Orientation Develpoment and Relaxation in Injection Molding of Amorphous Polymers." *Polym. Eng. Sci.* 18(4): 273-281.

Dutta, D., H. Fruitwala, A. Kohli, and R. A. Weiss. 1990. "Polymer Blends Containing Liquid Crystals: A Review." *Polym. Eng. Sci.* 30(17): 1005.

Froix, M. F. July 3, 1980, U. S. patent 4,460,735.

Halpin, J. C., 1969. *J. Compos. Mater.* 3: 732.

Heino, M. T. and J. V. Seppala. 1992. "Extruded Blends of a Thermotropic Liquid Crystalline Polymer with Polyethylene Terephthalate, Polypropylene and Polyphenylene Sulfide." *J. of Appl. Polym. Sci.* 44:2185.

Instron. 1979. *User's Manual*. Inston Corporation, Canton, Massachusetts.

Isayev A. I. and M. J. Modic. 1987. "Self-Reinforced Melt Processable Polymer Composites: Extrusion, Compression, and Injection Molding." *Polym. Compos.* 8(3): 158.

James, S. G., A. M. Donald, and W. A. MacDonald. 1987. "Blends of a Liquid Crystalline Copolyester with Polyethersulphone." *Molec. Cryst. Liq. Cryst.* 153: 491.

Kiss, G. 1987. "*In situ* Composites Blends of Isotropic Polymer and Thermotropic Liquid Crystalline Polymers." *Polym. Eng. Sci.* 27(6): 410.

Kolhi, A., N. Chung, and R. A. Weiss.1989. "The Effect of Deformation History on the Morphology and Properties of Polycarbonate and a Thermotropic Liquid Crystalline Polymer." *Polym. Eng. Sci.* 29(9): 573.

REFERENCES
(Continued)

Kulichikin, V. G., O. V. Vasil'eva, I. A. Litvinov, E. M. Antipov, I. L. Parsamyan, and N. A. Plate. 1991. "Rheology and Morphology of Polymer Blend Containing Liquid-Crystalline Component in Melt and Solid State." *J. of Appl. Polym. Sci.* 42(2):363.

Kyolani, M., A. Kaito, and K. Nakagawa. 1992. "Applications of Fourier Transform Infrared Microspectroscopy to the Analysis of Microscopic Orientation in Liquid Crystalline Polymer Sheets." *Polymer,* 33: 2672 - 2678.

La Mantia, F. P., A. Valenza, M. Paci, and P. L. Magagnini. 1990. "Rheology-Morphology relationships in Nylon 6/Liquid Crystalline Polymer Blends." *Polym. Eng. Sci.* 30(1): 7.

La Mantia, F. P., M. Saiu, A. Valenza, M. Paci, and P. L. Magagnini. 1990. "Relationships Between Mechanical Properties and Structure for Blends of Nylon 6 with a Liquid Crystal Polymer." *Europ. Polym. J.* 26(3): 323.

Lee, H. S. 1997. "Finite Element Analysis for the Flow Characteristics Along the Thickness Direction in Injection Molding." *Polym. Eng. Sci.* 37(3): 559-567.

Lee, W., A. T. Dibenedetto, and J. M. Gromek. 1993. "Processing of Thermotropic Liquid Crystalline Polymers and Their Blends - Analysis of Melt-Spinning TLCP Fibers." *Polym. Eng. Sci.* 33(3): 156.

Li, J. X., M. S. Silverstein, A. Hiltner, and E. Bare. 1992. "Morphology and Mechanical Properties of Fibers From Blends of a Liquid Crystalline Polymer and Poly(ethylene Terephthalate)." *J. of Appl. Polm. Sci.* 44: 1531 - 1542.

Lin, Q., J. Jho, and A. F. Yee. 1993. "Effect of Drawing on Structure and Properties of a Liquid Crystalline Polymer and Polycarbonate *In-Situ* Composite." *Polym. Eng. Sci.* 33(13): 789.

Lin, Q. and A. F. Yee. 1994. "Elastic Modulus of *In-situ* Composite of a Liquid Crystalline Polymer and Polycarbonate." *Polym. Compos.* 15(2): 156.

Mavridis, H., A. N. Hrymark, and J. Vlachopoulos. 1986. "Finite Element Simulation of Fountain Flow in Injection Molding." *Polym. Eng. Sci.* 26(7): 449 - 454.

McCrum, N. G., C. P. Buckley, and C. B. Bucknall. 1992. *Principles of Polymer Engineering*. Oxford University Press, New York, p. 209, p. 218.

REFERENCES
(Continued)

Mehta, S. and B. L. Deopura. 1993. "Fibers From Blends of PET and Thermotropic Liquid Crystalline Polymer." *Polym. Eng. Sci.* 33(14): 931.

Nobile, M. R., E. Amendola, and L. Nicolais. 1989. "Physical Properties of Blends of Polycarbonate and a Liquid Crystalline Copolyester." *Polym. Eng. Sci.* 29(4): 244.

Naitove, M. H. 1985, April. "A Processing Guide to Liquid Crystal Polymers." *Plastics Technology*, p. 85 - 89.

O`Donnell, H. J. and D. G. Baird. 1996. "The Effect of Injection Molding Conditions on the Mechanical Properties of an *In-situ* Composite. I: Polypropylene and a Liquid Crystalline Copolyester Based on Hydroxynaphthoic Acid." *Polym. Eng. Sci.* 36(7): 963.

Qin, Y., D. L. Brydon, R. R. Mather, and R. H. Wardman. 1993. " Fibers From Polypropylene and Liquid Crystal Polymer (LCP) Blends: 2. Effect of Extrusion and Drawing Conditions." *Polymer* 34(6): 1202.

Roetting O., and G. Hinrichsen. 1994. "Blends of Thermotropic Liquid Crystalline and Thermoplastic Polymers: A Short Review." *Advances in Polymer Technology* 13(1): 57 - 64.

Sawyer, L. C. and M. Jaffe. 1991. "Structure-Property Relationships in Liquid Crystalline Polymers." *High Performance Polymers.* E. Baer et al. (Eds). Hanser Publishers, New York, p. 63.

Seo, Y., S. S. Hwang, S. M. Hong, T. S. Park, and K. U. Kim .1995. "Effect of Die Geometry on the Structural Development of a Thermotropic Liquid Crystalline Polymer in a Thermoplastic Elastomer Matrix." *Polym. Eng. Sci.* 35(20): 1621.

Shin, B. Y., S. H. Jang, I. J. Chung, and B. S. Kim. 1992. "Mechanical Properties and Morphology of Polymer Blend of Poly (ethylene Terephthalate) and Semiflexible Thermotropic Liquid Crystalline Polyesters." *Polym. Eng. Sci.* 32: 73.

Siegmann, A., S. Dagan, and S. Kenig. 1985. "Polyblends Containing a Liquid Crystalline Polymer." *Polymer,* 28(9):1325.

Silverstein, M. S., A. Hiltner, and E. Baer. 1991. "Hierarchical Structure in LCP/PET Blends." *J. of Applied Polymer Sci.*, 43:157.

REFERENCES
(Continued)

Song, M., G. Hu, and Q. Zhu. 1993. "Study on the Relationship Between the Mechanical Properties and Processing for Self-Reinforced Polymer: 2-A Quantitative Characterization of Tensile Modulus for Self-Reinforced Polymers." *Polymer Testing* 12:311.

Suokas, E. 1989. "The Microstructure of Injection-Molded Thermotropic Copolyester: 1. Optical and Scanning Electron Microscope Studies." *Polymer*, 30(6): 1105.

Tadmor, Z. 1974. "Molecular Orientation in Injection Molding." *J. of Appl. Polym. Sci.* 18:1753 - 1772.

Taylor, G. I. 1934. *Proc. R. Soc.* A146: 501.

Tsai, S. W. 1968. U. S. Govt. Rept. AD 834851.

Utracki, L. A. 1990. *Polymer Alloys and Blends*. Hanser Publishers, New York, p.1.

Weiss, R. A., W. Huh, and L. Nicolais. 1987. "Novel Reinforced Polymers Based on Blends of Polystyrene and a Thermotropic Liquid Crystalline Polymer." *Polym. Eng. Sci.* 27(9): 684.

Wood, A. S. April 1985. "Liquid-Crystal Polymers: Now They Are Melt Processable." *Modern Plastics*, p. 78.

Yi, X. S., F. Shi, and W. Michaeli. 1996. "The Modulus of Shear-Induced Fibers From a Thermotropic Liquid Crystalline Polymer in a Thermoplastic Matrix." *Polym. Composite* 17(3): 423.

Zhuang, P., T. Kyu, and J. L. White. 1988. "Characteristics of Hydroxybenzonic Acid-Ethylene Terephthalate Copolymers and Their Blends with Polystyrene, Polycarbonate, and Polyethylene Terephthalate." *SPE ANTEC Tech. Papers*, 34:1237.

Zachariades, A. E. and T. Kanamoto. 1979. "Morphological Model." *Ultra High Modulus Polymers*, A. Ciferri and I. M. Ward (Eds), Applied Science, London, p. 309.